TECHNISCHE UNIVERSITÄT WIEN
Vienna University of Technology

DIPLOMARBEIT

DIFFERENTIAL PHASE CONTRAST IN SWEPT SOURCE OPTICAL COHERENCE TOMOGRAPHY

Ausgeführt am

Institut für Angewandte Physik

der Technischen Universität Wien

unter der Anleitung von

Ao.Univ.Prof. Dipl.-Ing. Dr.techn. Martin Gröschl

in Zusammenarbeit mit

Assoc. Prof. DI Dr. Michael Pircher

Zentrum für Medizinische Physik und Biomedizinische Technik

der Medizinischen Universität Wien

durch

Paul Fuchs BSc

Mommsengasse 17/12

1040 Wien

August 2021

MEDIZINISCHE UNIVERSITÄT WIEN

Master Thesis

Differential phase contrast in swept source optical coherence tomography

Paul Fuchs

Supervised by

Assoc. Prof. DI Dr. Michael Pircher[1]

Ao.Univ.Prof. Dipl.-Ing. Dr.techn. Martin Gröschl[2]

[1]Center for Medical Physics and Biomedical Engineering, Medical University of Vienna,

Währinger Gürtel 18-20, AKH 4L, A-1090 Vienna, Austria

[2]Institute of Applied Physics, Vienna University of Technology, Wiedner Hauptstraße

8-10/134, A-1040 Vienna, Austria

Vienna, 11.8.2021

Abstract:

Optical coherence tomography (OCT) is an imaging technique that is capable of providing cross sectional images of biological tissues with micrometer resolution. As the method is based on interferometry, the phase component of the backscattered light is accessible and theoretically opens the possibility of measuring length differences in the pico-meter range. Practically, interferometric jitter and sample motion greatly influence the corresponding phase measurements limiting corresponding applications. To overcome this limitation, a differential phase-contrast technique can be used. The basic idea is that two light beams of different focus diameters incident collinearly onto the sample. The beam with small focus diameter is used as probing beam, while the beam with broad focus diameter serves as phase reference and enables to subtract for phase changes introduced by motion or interferometric jitter.

This work focuses on the practical realization of a differential phase-contrast system operating at high imaging speeds, including development of corresponding signal acquisition and data evaluation software. The system is based on a polarization sensitive swept-source OCT setup that has been modified in this work for differential phase contrast imaging.

An alignment procedure is presented and the phase stability that can be achieved with the system is determined.

Finally, the characteristic parameters of the system in terms of resolution, sensitivity and imaging depth are assessed. Several technical samples have been measured and the measurement performance of the instrument is quantified.

Kurzfassung:

Die optische Kohärenz Tomografie (OCT) ist ein bildgebendes Verfahren, das Querschnittsbilder von biologischen Geweben mit einer Auflösung im Mikrometerbereich generiert. Da die Methode auf Interferometrie beruht, ist die Phase des rückgestreuten Lichts zugänglich und erlaubt theoretisch die Messung von Längenunterschieden im Pikometerbereich.

In der Praxis beeinflussen Schwankungen im Interferometer und die Bewegung der Probe die Phasenmessung und limitieren damit den Anwendungsbereich. Um diese Hürde zu überwinden, kann die Phasenkontrast-Methode verwendet werden. Die Grundidee ist, dass zwei Lichtstrahlen verschiedener Fokusdurchmesser kollinear auf die Probe treffen. Der Strahl mit kleinem Fokusdurchmesser wird zur Beprobung verwendet, der Strahl mit breitem Durchmesser dient als Phasenreferenz und ermöglicht damit die Phasenänderungen, die von der Probenbewegung und den Schwankungen im Interferometer herrühren, abzuziehen.

Diese Arbeit widmet sich der praktischen Realisierung eines differentiellen Phasenkontrast-Systems, bei dem die Bildgebung mit sehr hoher Geschwindigkeit erfolgt, einschließlich der Entwicklung zugehöriger Software im Bereich der Signalerfassung und Datenauswertung.

Die Methode basiert auf einem polarisationssensitiven OCT System, das in dieser Arbeit modifiziert wurde, um differentielle Phasenkontrast-Bilder aufnehmen zu können. Für das Funktionieren der Methode ist eine perfekte Justierung des Systems essentiell. Im Rahmen dieser Arbeit wird deshalb ein genaues Prozedere vorgestellt, um eine hohe Genauigkeit der Justierung zu erzielen. Des Weiteren wird die mit diesem System erreichbare Phasenstabilität wird bestimmt.

Schließlich werden die charakteristischen Parameter des Messsystems, in Bezug auf Auflösung, Sensitivität und Abbildungstiefe, bestimmt. Verschiedene technische Proben wurden gemessen, um die Leistungsfähigkeit des Geräts zu quantifizieren.

Acknowledgements:

I am deeply grateful for the supervision of Assoc. Prof. DI Dr. Michael Pircher of the Center for Medical Physics and Biomedical Engineering, Medical University of Vienna, who introduced me to the field of OCT, and his expertise and support on a daily basis as well as an open ear for my concerns allowed me to build a good foundation in the topic of OCT and to develop the differential phase contrast OCT system.

I would also like to thank my supervisor Ao.Univ.Prof. Dipl.-Ing. Dr.techn. Martin Gröschl of the Institute of Applied Physics, Vienna University of Technology, who evoked my interest for medical physics and also introduced me to Michael Pircher.

I am thankful to Prof. Christoph Hitzenberger of the Center for Medical Physics and Biomedical Engineering, Medical University of Vienna, who contributed a lot of ideas to solve issues occurring in the development of the system, as well as in terms of interpretation of the results.

I also want to thank Dr. Muhammad Faizan Shirazi for his advice and his support, Dr. Elisabeth Brunner for her kind support and motivation, Sylvia Desissaire for her practical advice with the build-up and for everyone I worked with for the heartful working environment.

Special thanks go to Ao.Univ.Prof. Dipl.-Ing. Dr.techn. Christoph Eisenmenger-Sittner from the Institute of Solid State Physics, Vienna University of Technology, for the production of the test samples.

Finally, I must express my very profound gratitude to my brother and my parents that continuously encourage me, support me and believe in me.

TABLE OF CONTENTS

A. Introduction and motivation

Optical coherence tomography (OCT) is an interferometric technique and uses low time-coherent light sources. OCT provides high-resolution cross-sectional images at short acquisition times and is a powerful tool to non-invasively image various tissues [1].

Classical OCT images the distribution of the backscattering potential of the object, i.e., it yields an image of the light intensity that is backscattered or reflected at the different structures of an object [2]. OCT images are B-scan images synthesized from laterally adjacent low (time-) coherence interferometry (LCI) depth scans or "A-scans" [2]. The use of low-coherence light sources enables the isolation of the region of interest within a depth range and avoids influences from nearby reflections [3-6].

In a typical OCT interferometer, the light from the light source is first split into a sample and reference beam. The sample beam illuminates the object and light that is backscattered from it is then brought to interference (at the interferometer exit) with the light returning from the reference beam path. The optical amplification of the signal through the interference between a strong reference light and a weak sample light results in a high sensitivity of the technique.

Two different variants or techniques exist for LCI and OCT [6]:

In time-domain OCT (TD-OCT) the reference arm´s length is changed with time and the light intensity (returning from the reference and sample arms, respectively) at the interferometer exit is detected by a point detector at different reference mirror positions.

Only light that travelled a similar optical distance (within the range of the double pass coherence length of the light source) in the reference and sample arms, respectively, contributes to the detected interference signal and allows therefore a separation between axially displaced structures. A Hilbert-transformation can then be used on the recorded interference signal to extract amplitude and phase of the measured depth profile.

In Fourier-domain OCT (FDOCT), the reference mirror is kept at a fixed position and the interference signal is recorded in dependence of the wavelength. Two variants of FDOCT exist: Swept source OCT (SSOCT), where a tunable light source that sweeps through the different wavelengths (or wavenumbers k) is used to illuminate the interferometer [7] and spectral domain OCT (SDOCT) where the light in the interferometer exit is spectrally dispersed and detected [8]. In SSOCT, at a single time point, the light source sends out light at a certain wavelength (with narrow bandwidth). Over time the wavelength is changed which results in a broad spectrum of the light emission within one wavelength tuning (sweep). Ideally, this spectrum is evenly spaced in k-space [9] when the sweep is sampled evenly in time. The detection unit has to be operated at a sample rate that equals twice the sample rate

of the sweep in order to fulfil the Nyquist criteria. As the signal is already recorded in k-space, the depth profile (as recorded in TDOCT) can be retrieved by an inverse Fourier transformation of the recorded spectral interferogram.

In SDOCT, a spectrometer in the detection unit is used for the wavelength dependent detection of the interferometric signal [8]. The recorded spectrum needs to be mapped into k-space $k = \frac{2\pi}{\lambda}$ (k…wavenumber, λ…wavelength) before performing Fourier transformation into spatial domain for retrieving a depth profile because the data is recorded evenly spaced in wavelength which results otherwise in a broadening of the axial point spread function (or coherence function) [10].

The major advantage of SSOCT in relation to SDOCT is that the signal to noise (SNR) drop with depth location resulting from the finite wavelength resolution during signal acquisition is negligible [9].

One extension for OCT is differential phase contrast that has been introduced to quantify sub imaging wavelength axial displacements of small sample structures [11]. For achieving differential phase contrast, typically two independent light beams are used to illuminate the sample. One light beam serves as a phase reference while the other is used to probe subtle phase changes introduced by the sample. The differential phase between both beams eliminates phase jitter caused by vibration within the interferometer as well as phase changes introduced by sample motion. The two beams can be realized for example by using polarized light, which can be split into two orthogonal and thus independent polarization states.

In order to offer a brief insight into differential phase contrasting methods in OCT, several developments are mentioned in the following.

In 1999, Hitzenberger and Fercher [12] developed a polarization sensitive TD-OCT setup, where a circular polarization state in the sample arm is split into two parallel beams of orthogonal linear polarization states using a Wollaston prism. Two adjacent positions of the object are scanned simultaneously and an axial displacement at the sample between those two positions resulted in a change of the phase difference between both beams. This change was measured and the resulting signals were converted to OCT images with increased contrast [12].

In 2002, Sticker et al. [11] introduced a differential phase contrast TDOCT system that is able to image single cell layers. The method is based on two polarization encoded beams impinging collinearly onto the sample. The probing beam has a narrow focal spot diameter

while the broader beam represents the phase reference. Small phase changes of the phase are thereby detected and additional depth contrast compared to intensity images is gained.

In 2008, Huang et al. [13] built a differential-phase optical coherence reflectometer (DP-OCR). An analog differential phase decoding method is integrated and high-resolution measurements of axial displacement of a localized surface profile is presented.

Also published in 2009, Pircher et al. [14] created a phase contrast coherence microscopy setup for en-face OCT. The concept is based on the assumption that the use of a high transverse imaging speed (of the order of several kilohertz) makes phase changes owing to jitter within the interferometer (or sample motion) separable from phase changes introduced by the sample structure as these occur on different time scales [14]. An elimination algorithm is introduced to remove a residual phase jitter of the interferometer and phase contrast images of red blood cells are presented.

In 2009, Heisse and Stifter [15] extended a previous method [12] specifically for technical samples. The instrument is based on a polarization sensitive TDOCT setup and a Wollaston prism for introducing a transversal displacement between the two orthogonal polarized sample beams. By using the rotatability of the Wollaston-prism two phase contrast images can be obtained for two different (orthogonal) rotation angles of the prism. A shape from shading (SfS) - algorithm [16] is used for retrieving cumulative phase contrast images of a microlens array and particles on an oil film.

In 2013, Heldermann et al. [17] introduced a method similar to [11] for optical coherence phase microscopy (OCPM). Usually, in OCPM the phase difference is measured between two interfaces of a glass plate (where the sample is located). For high numerical aperture imaging insufficient back reflection of the reference glass interfaces is observed. In order to overcome this limitation that is associated with a reduced phase stability, a common path setup is implemented that uses two beams of different focus diameter. The beam with a larger focal spot diameter and depth of field yields high reflection at both glass plate interfaces and is used as a phase reference while the narrower beam is used as probing beam. The measured phase stability values depend on the signal to noise ratio of the signals and are close to the theoretical expected values.

This underlying work builds upon previous two beam methods for enabling phase contrast imaging in OCT [11]. An existing polarization sensitive SSOCT-setup [18] based on single-mode fibers is modified for enabling phase contrast imaging. The required beam separation is realized by insertion of a polarization sensitive Mach-Zehnder interferometer into the sample

arm of the main interferometer. Both beams are focused on the sample. The beam with larger spot size and lower transverse resolution serves as reference beam, the narrow beam with higher resolution is used as probing beam. Thereby, phase stability between the beams is provided and small phase changes that are associated with depth variations in the nanometer range are detectable.

In this thesis, the experimental realization, the procedures that are needed for the development of the system are outlined together with test measurements and a characterization of the system.

B. Theory

1) Light waves in interferometry

1.1 Light as a planar wave

Light is an electro-magnetic transverse wave. A transverse wave describes an oscillation of the electric or magentic field vector that propagates orthogonally to its axis (axes) of oscillation. For simplification, only the electric field vector is considered and the coordinate system is placed in a way, that the direction of propagation is the z-axis. At the source position z=0, an oscillation of the electric field vector $\mathbf{E}$ in time (t) is described with a prefactor $\mathbf{A_0}$ reflecting direction and amplitude of the wave, ω reflecting the frequency of the oscillation:

$$\mathbf{E}(t) = \mathbf{A_0} \cdot \cos(\omega t) \tag{1}$$

When the wave propagates in space, the oscillation is phase shifted (retarded) to the initial oscillation. This phase shift $\Delta\varphi$ depends on the position z, the oscillation frequency ω and the velocity of propagation c. The negative sign denotes that the wave oscillates retarded compared to the initial position, at the location z:

$$\Delta\varphi = -\frac{\omega}{c}z = -\frac{2\pi}{\lambda}z = -kz \tag{2}$$

The linear factor k is called wavenumber and goes reciprocal with the wavelength λ. It determines how dense the wave oscillates in space.

$$\mathbf{E}(z,t) = \mathbf{A_0} \cdot \cos(\omega t - kz) \tag{3}$$

The z-propagation of waves of different wavenumbers k are shown in Fig. 1.

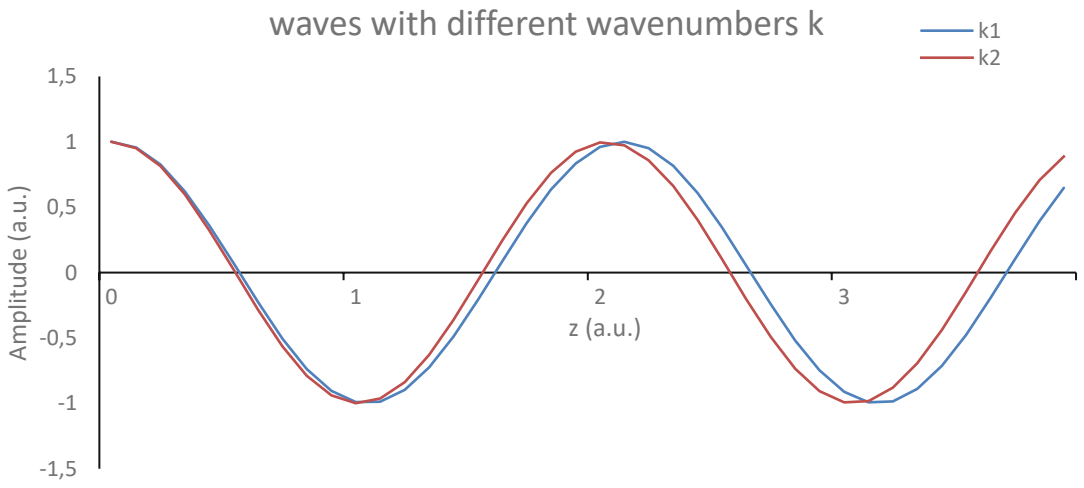

Figure 1: Propagation of waves with different wavenumbers k1 and k2

As Fig. 1 shows, for a given z depth position z≠0, the phase of each wave is different.

1.2 Wave propagation in an interferometer

In a Michelson interferometer (Fig. 2), the generated wave is split into two waves at a beam splitting unit, for instance a 50:50 beam splitter. One beam enters the reference arm to be backreflected at a mirror, the other beam impinges on the sample and is backscattered. After backreflection, both beams are recombined at the beam splitting component and interfere.

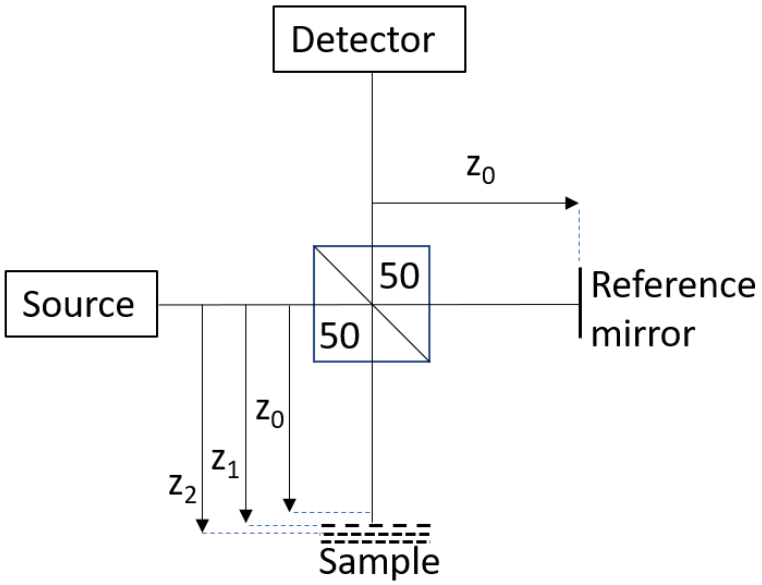

Figure 2: Scheme of a Michelson interferometer. The light from the light source is split into two components, the sample and reference beam by the 50:50 beam splitter. The sample beam is reflected at different depth positions z_i while the reference beam is always reflected at the same depth position z_0. After being reflected or backscattered, the two beams are combined again at the beam splitter and the interfering light is detected by the detector.

In Fourier domain interferometry, the reference arm remains unchanged, which means the wave always returns at a reference phase $2kz_0$, with k as the wavenumber and z_0 as the path length between reference mirror and beam splitter. In the sample arm, the wave is backscatterd at different sample depths corresponding to different path lengths z_i and consequently returns at different phases $2kz_i$. When sample wave and reference wave are reunified, the phase difference (determined by the path length difference between reference and sample light) of the waves determines if constructive or destructive interference occurs.

In order to create a mathematical understanding of Fourier domain interferometry, the calculation of the interferometric signal is shown in the following.

The wave field obtained by overlap of sample and reference wave is calculated by vector addition and the total intensity detected by the detector is given by the square of the electric field:

$$\mathbf{E_{tot}}(z_i, t) = \mathbf{E_r}(z_0, t) + \mathbf{E_s}(z_i, t) = \mathbf{A_r} \cdot \cos(\omega t - 2kz_0) + \mathbf{A_s} \cdot \cos(\omega t - 2kz_i) \quad (4)$$

$$I_{tot}(z_i, t) = |\mathbf{E_{tot}}(z_i, t)|^2 \quad (5)$$

$\mathbf{A_r}$ and $\mathbf{A_s}$ are the electric field amplitudes returning from reference and sample arm. The detector's response time is much slower than the electric field oscillation. Consequently, many periods $\frac{2\pi}{\omega}$ of the light wave are detected during one detector exposure. The detected intensity is thereby averaged over the detector exposure time T.

$$I_{det} = \bar{I}_{tot}(z_i) = \frac{1}{T}\int_0^T [|\mathbf{A_r}| \cdot \cos(\omega t - 2kz_0) + |\mathbf{A_s}| \cdot \cos(\omega t - 2kz_i)]^2 dt =$$

$$= \frac{1}{T}\int_0^T \left\{ \begin{matrix} |\mathbf{A_r}| \cdot [\cos(\omega t)\ \cos(2kz_0) + \sin(\omega t) \sin(2kz_0)] + \\ +|\mathbf{A_s}| \cdot [\cos(\omega t)\ \cos(2kz_i) + \sin(\omega t) \sin(2kz_i)] \end{matrix} \right\}^2 dt \qquad (6)$$

As the detector period T is of the order of 10^{-8} s and the light frequency ω of the order of 10^{15} Hz, the integrals can be approximated by:

$$\frac{1}{T}\int_0^T \cos^2(\omega t)\, dt = \frac{1}{T}\int_0^T \sin^2(\omega t) dt = \frac{1}{2} \qquad (7a)$$

$$\frac{1}{T}\int_0^T \sin(\omega t)\cos(\omega t)\, dt = 0 \qquad (7b)$$

Consequently, the detected intensity consists of two constant terms and the interference term, that depends on the relative phase of reference arm and sample arm $\Delta\varphi$:

$$\bar{I}_{tot}(z_i) = |\mathbf{A_r}|^2 + |\mathbf{A_S}|^2 + 2|\mathbf{A_r}||\mathbf{A_S}| cos \underbrace{(2k(z_i - z_0))}_{\Delta\varphi} \qquad (8)$$

Note that the relative phase $\Delta\varphi$ is a function of the path length difference $\Delta s = 2(z_i - z_0) = 2\Delta z_i$ and the wavenumber k. Δz_i describes the depth positions in the sample arm with respect to the reference position z_0.

1.3. Swept source optical coherence tomography (SSOCT)

In swept source OCT, the light source sends out a discrete spectrum of waves of different wavenumbers k that form a specific amplitude distribution (depending on the gain medium of the laser) equally spaced in k-space. The waves are sent out and detected separated in time, which enables the assignment of the detected intensity and the corresponding wavenumber k. The amplitude spectrum of the source contains the amplitudes of each emitted wavelength region and is shown in Fig. 3.

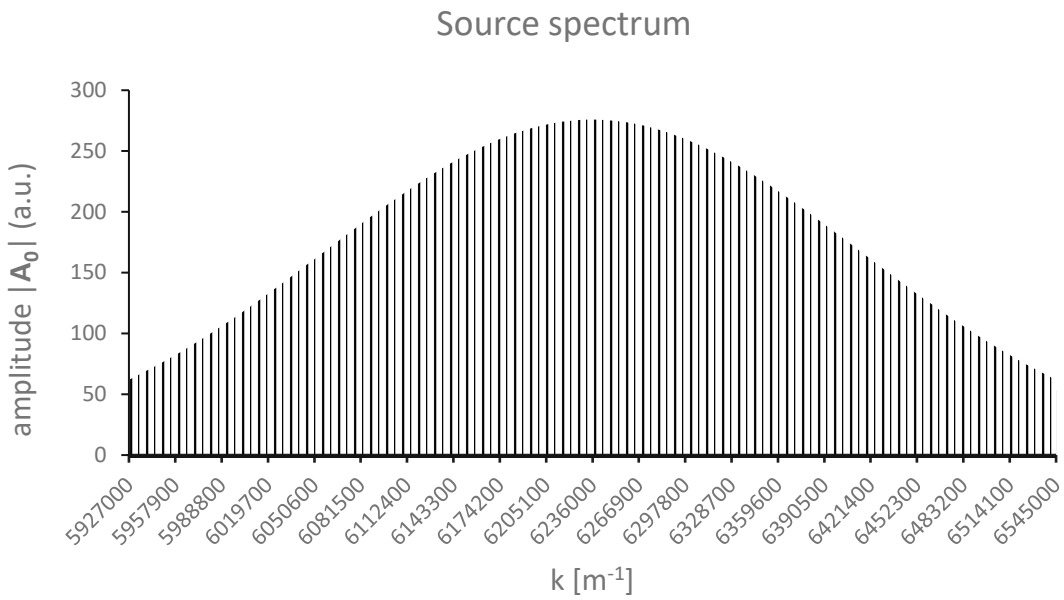

Figure 3: Example of a discrete source spectrum of a swept laser source that is obtained during one full wavelength sweep. Each wavelength (or k) is emitted at a different time point. The amplitudes of the different waves k emitted by this ideal swept laser source describe a Gaussian curve in k-space.

Illuminating the interferometer with waves of different wavenumbers k_j and placing a mirror in the sample arm at position Δz_i results in a modulated intensity spectrum at the detector, as the inteference term $\cos(2k_j\Delta z_i)$ depends on the wavenumber k_j. The recorded interference spectrum can be calculated by:

$$A_{\mathrm{det}}(\Delta z_i, k_j) = \sqrt{\bar{I}_{tot}(\Delta z_i, k_j)} =$$

$$= \sqrt{|\mathbf{A_r}(k_j)|^2 + |\mathbf{A_S}(k_j)|^2 + 2|\mathbf{A_r}(k_j)||\mathbf{A_S}(k_j)|\cos(2k_j(\Delta z_i))} \qquad (9)$$

The dependencies $\mathbf{A_r}(k_j), \mathbf{A_S}(k_j)$ indicate that every wave k_j is originally sent out with the corresponding source amplitude $\mathbf{A_0}(k_j)$ and reflect the losses in the interferometer arms (Fig. 3).

An interference signal $A_{\mathrm{det}}(\Delta z_i, k_j)$ created by interference between sample and reference arm light with a path length difference between the arms of Δz_i is shown in Fig. 4.

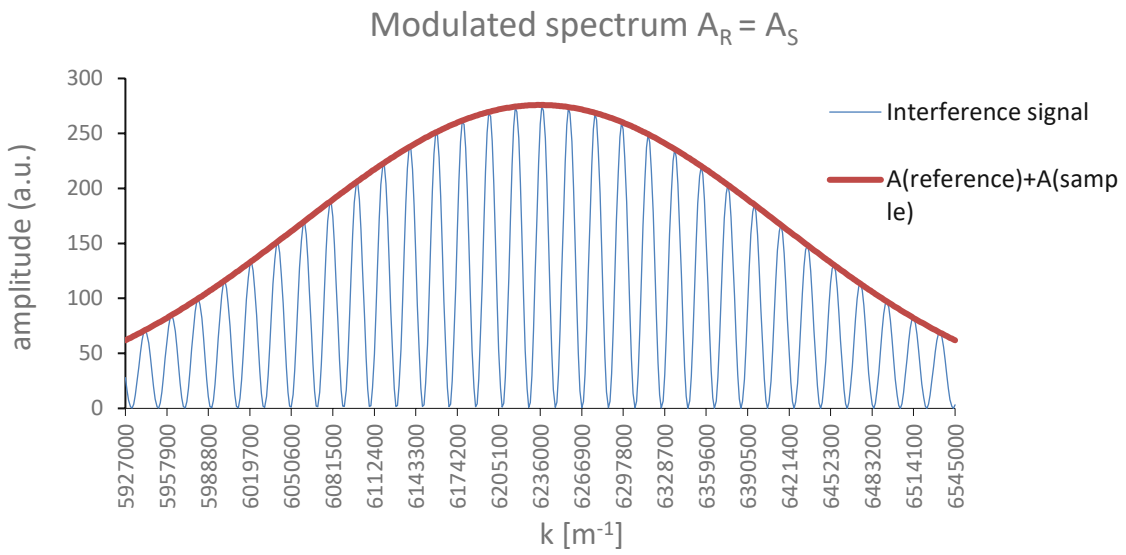

Figure 4: Simulated interferometric signal in k-space arising from a single reflector in the sample arm and reference arm, respectively, that show a path length difference 2Δz. In case of equal strength of the beams, the envelope (red line) corresponds to the amplitude sum, while destructive interference results in complete annihilation of the signal.

The interference signal oscillates with a frequency of $2\Delta z_i$ in k-space (cf. Formula (9)).

As the sample in general is not a perfect reflector, the light amplitude returning from the sample is attenuated by scattering. Thus, a non-perfect destructive interference is observed that results in a lower envelope of the interference signal as shown in Fig. 5.

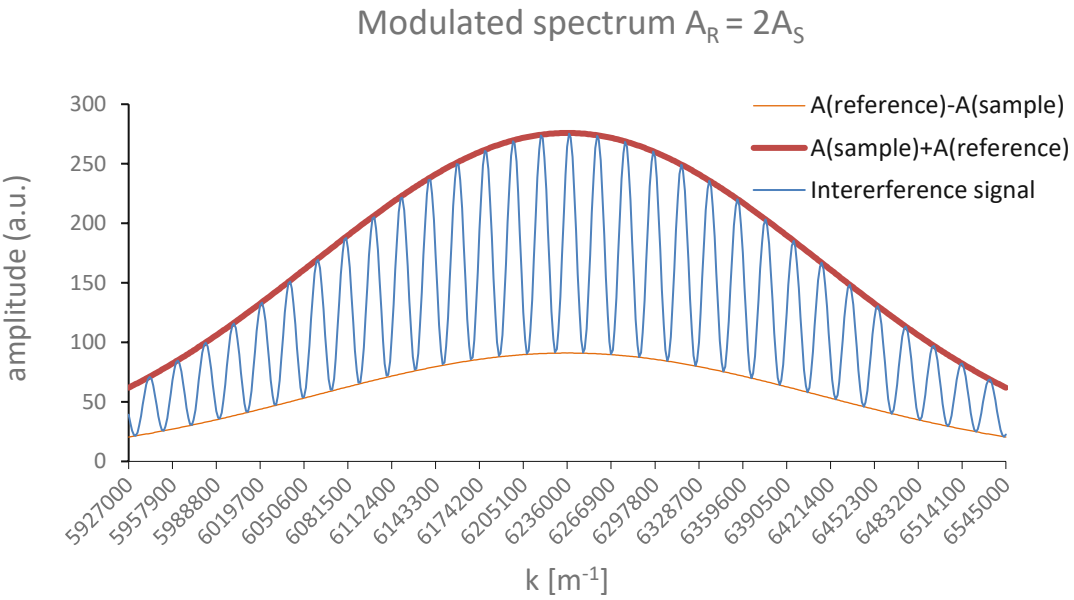

Figure 5: Simulated interferometric signal in k-space evoked by a single reflector in the sample arm that shows a path length difference 2Δz to the reference arm: The light returning from the sample arm is weaker than that returning from the reference arm, residual light from the reference arm will be detected even if destructive interference with the sample arm light occurs.

Fourier transformation of the modulated k-spectrum delivers a peak corresponding to the dominating frequency associated with the path length difference between sample and reference arm Δz_i. The absolute valued part of the complex Fourier transformed k-spectrum

can be considered as a depth profile of the sample. The depth profile of a single reflector (Fig. 4) is shown in Fig. 6.

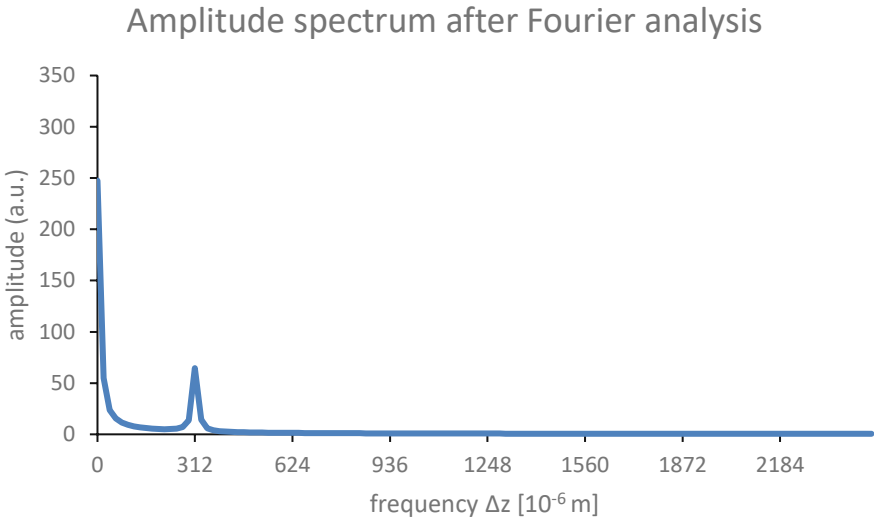

Figure 6: Depth profile of a single reflector: the peak at the zero frequency corresponds to the envelope of the spectrum, the second peak represents the frequency corresponding to the depth position of Δz of the reflector.

The peak around the zero frequency results from the DC component of the spectrum in Fig. 4 and can be filtered out either by AC detection (a high pass filter) or by subtraction of the DC component (=reference spectrum without modulation) prior to Fourier transformation.

Remarks:

- Multiple reflexes at different depths Δz_i inside the sample result in various modulations with different frequencies that overlap in the k-spectrum. Fourier analysis separates these frequencies and thereby generates the axial profile (or A-scan) of the depth positions Δz_i of these reflexes. The amplitude detected for each frequency is a direct measure of the light intensity returning from these depth positions.
- Positive and negative frequencies: as the Fourier transformation does not differentiate between negative and positive path length difference between reference arm and sample arm, but only contains the absolute path length difference Δz_i, a mirrored axial depth profile could overlap the original depth profile. This can be prevented by placing the reference mirror in such a way that only positive (or only negative) path length differences in the sample arm are possible.
- The finite spacing between wavenumbers in the spectrum $\delta k = k_{j+1} - k_j$ limits the resolvable frequency, which means that the resolvable depth range is limited

by $\Delta z_{max} = \pi/\delta k$. After Fourier transformation, the total length of the generated depth profile equals the depth range of the system.

The finite bandwidth of the source spectrum limits the separation between frequencies Δz_i, which gives a theoretical limit for the minimal difference in depth that is still resolvable, the axial resolution. For a Gaussian spectrum as shown in Fig. 4 the axial resolution can be calculated by [19]:

$$\Delta z = \frac{2ln2}{\pi} \frac{{\lambda_0}^2}{\lambda_{FWHM}} \tag{10}$$

λ_0 is the central wavelength of the light source and λ_{FWHM} corresponds to the full width at half maximum wavelength interval of the emitted Gaussian spectrum.

The scaling inside the depth profile $\delta z = \Delta z_{i+1} - \Delta z_i$ is finally set by the total number of values used in the Fourier transformation. A reasonable selection is the inclusion of k-values where the light source emits light which results in a scaling that is slightly denser than the axial resolution.

Up to now, only the amplitude of the Fourier transformed interference signal has been considered. However, the Fourier transform yields complex values and thus access not only to the amplitude but also to the phase.

The phase of the Fourier transformed k-spectrum contains the phases of the modulations $\phi(\Delta z_i)$. In order to illustrate the meaning of the phase, two similar modulations Δz_i corresponding to interference of light from two very closely located sample depths (below the resolvable range given by the axial resolution of the system) with light from the refence arm are shown in Fig. 7.

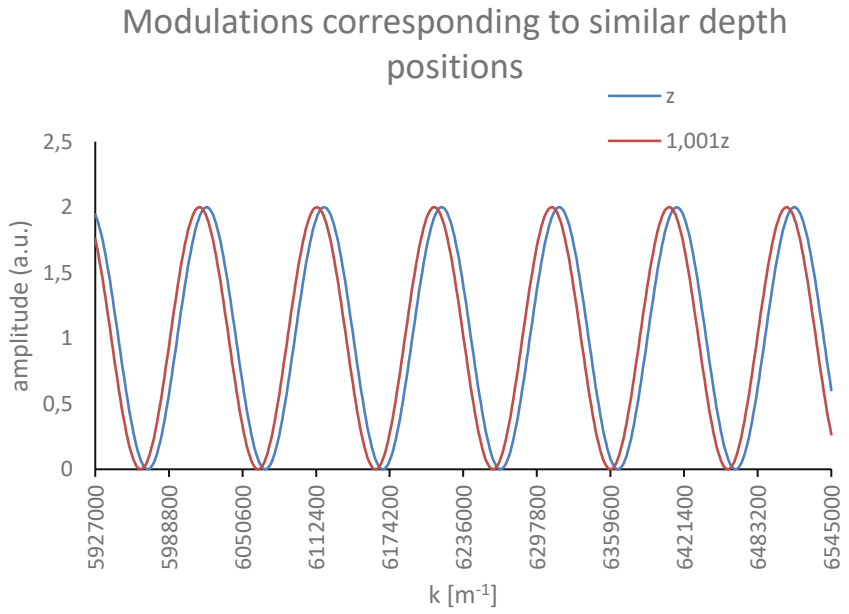

Figure 7: Two modulations representing path length differences of Δz=32.5µm (blue line) and Δz'=1.001z=32.5325 µm (red line) of two interfaces in the sample arm are shown in the k-spectrum. The difference in path lengths is mainly visible in the associated phase change between the modulation and not in the subtle frequency change.

The absolute valued amplitude spectrum z_i of the Fourier transformed k-spectrum is not able to resolve the difference between the frequencies, as the minimal step width between frequencies is limited by the axial resolution, that is typically in the order of micrometers.

However, the corresponding phase difference between the Fourier transformed k-spectrum in Fig. 7 $\phi(\Delta z)$ at the location of the peak of the amplitude is able to resolve that difference:

$$\Delta\phi = \phi(\Delta z) - \phi(\Delta z') = 2k_0(\Delta z - \Delta z') = \frac{4\pi}{\lambda_0}(\Delta z - \Delta z') \qquad (11)$$

In this case the depth difference of $\Delta z - \Delta z' = 32.5$ nm results in a phase difference of 23.4° (at a central wavelength λ_0 = 1000nm).

The amplitude and phase spectrum of the Fourier transformed k-spectrum of Fig. 7 are shown in Fig. 8.

While the amplitude of the Fourier transformed k-spectra show exactly the same peak at the same position $\Delta z = 32.5\ \mu m$ and do not allow a differentiation of the signals, the phase spectrum shows a clear difference at position Δz of $\Delta\phi(\Delta z) = 23.4°$. This phase difference is associated with the small depth variation $\Delta z' - \Delta z = 32.5\ nm$.

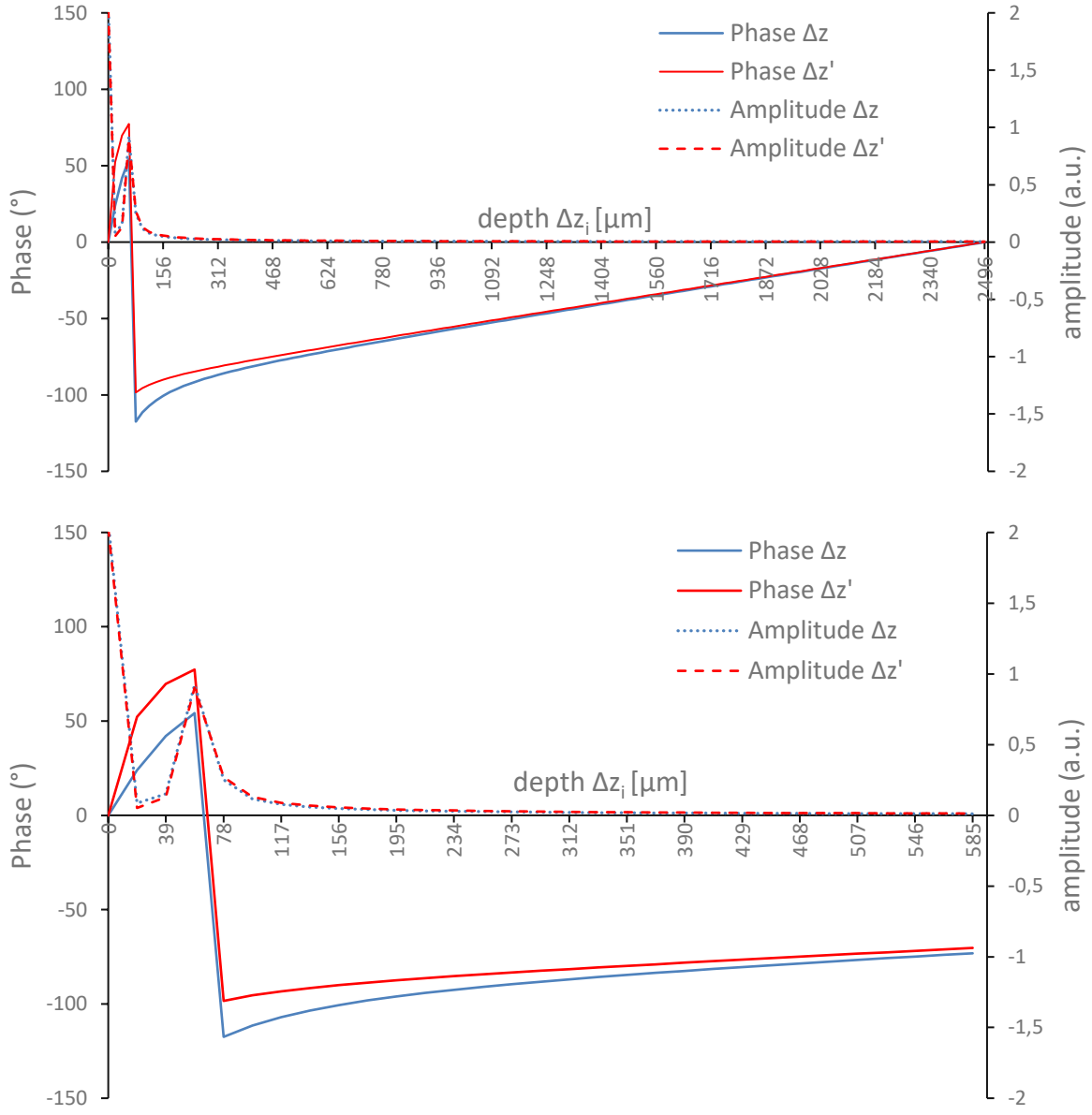

Figure 8: On top: Amplitude and phase of the Fourier transformed k-spectra shown in Fig. 7 over the whole depth range; bottom: Enlarged region around the amplitude peak for a better visualization of the phase difference.

It is important to note that the spacing of the sampling points $\delta z = \Delta z_{i+1} - \Delta z_i$ is not relevant, which means that the phase can be evaluated at all positions. The advantage of the phase lies in the fact that at a certain position a specific phase value can be determined that corresponds to subtle changes of the exact location of a reflex.

When interpreting the phase value, one has to take into account, that the phase of the Fourier transformed k-spectrum can only take values between $\pm\pi$. Consequently, phase values that in reality exceed this interval are mirrored into this interval. Phase unwrapping algorithms compensate for that and allow an explicit assignment of the phase.

The phase itself is highly sensitive to vibrations of the optical components or jitter within the interferometer as path length changes (between sample and reference arm) below the nanometer range will influence the phase measurement. An additional aspect is phase noise of the measurement that depends on the signal to noise ratio of the signal, where the phase is retrieved [20]. The noise can be calculated by:

$$\varrho_{Ph}^{th} = \sqrt{\frac{1}{SNR}} = \sqrt{\frac{\sigma_A}{\overline{I_A}}} \tag{12}$$

σ_A…Standard deviation of the detected intensity, $\overline{I_A}$…mean detected intensity

Phase differencing methods are therefore favorable to remove the influence of interferometric jitter or sample motion and to allow for measurement of phase changes introduced only by the sample structure.

2) Differential phase contrast

2.1. Differential phase contrast with two co-linear beams

One way to realize removal of the influence of interferometric jitter is a system with two co-linear sample beams of different beam diameter, illustrated in Fig. 9. Two collimated beams are focused onto the sample by an achromatic lens and produce focal spots of different size.

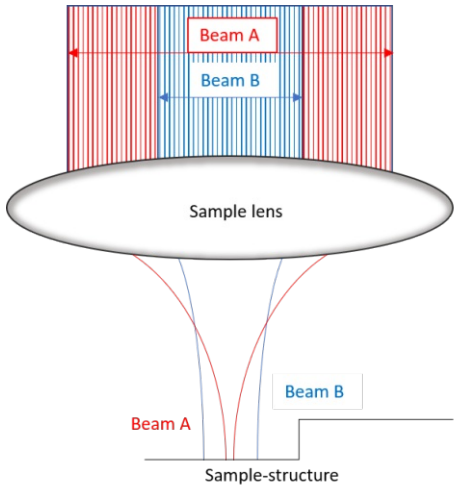

Figure 9: Illustration of two co-linear beams with different beam waist that are incident on a lens and thus produce two different focal spots with varying diameter. The beams illuminate a sample that shows a step in the surface profile.

When the beams scan over an edge in the sample structure, the beam with large focus diameter will show a smooth phase change in the interferometric signal from the sample surface, as it interacts with the step on a lateral path length that corresponds to the focus diameter (cf. Fig. 10). The sharp beam will produce a steep step function, according to its smaller focus diameter.

A simulation program was written in order to simulate that behavior.

The evolution of the absolute phases of both beams when scanning over a rising edge on the sample surface is approximated by hyperbolic tangent functions of different slope:

$$\varphi_i(x) = A \cdot [\tanh(c_i x)] \qquad (13)$$

x…lateral position, $\varphi_i(x)$…Phase of beam i, c_i…slope of beam i, A…half height of the step (half step size)

The phase difference between the beams shows a smaller change in amplitude than the individual phase change of each beam (cf. Fig. 10), which indicates that a recalculation factor is necessary in order to determine the step size of the sample from the phase difference signal.

Note that the lateral distance from the step, where the phase difference function shows a non-constant behavior, is given by the lateral distance where the bigger (blue) beam shows changes.

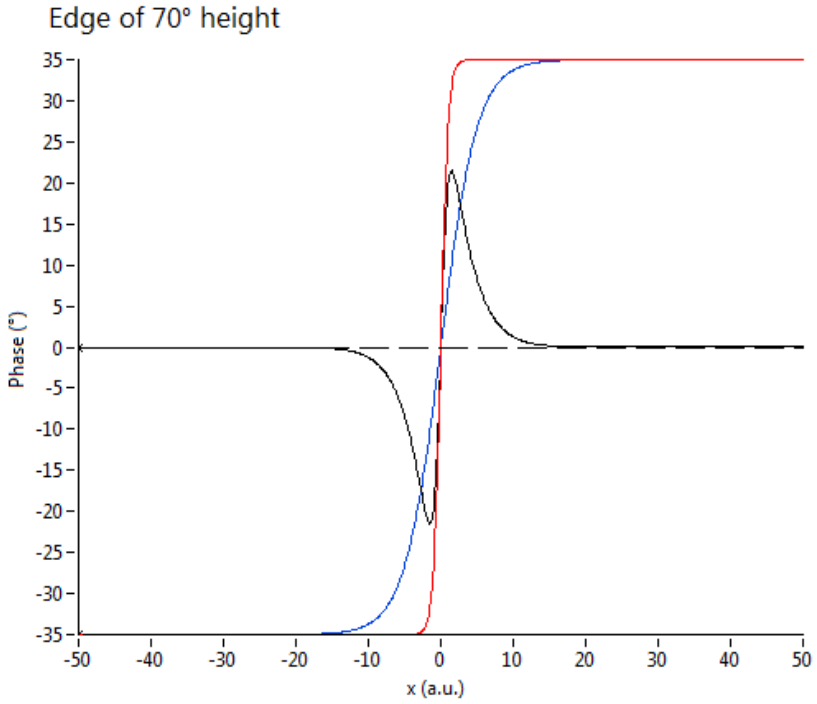

Figure 10: Simulated absolute phase functions for beam A (red) and beam B (blue) illustrated in Fig. 9 during scanning over a sample with a small step size at the surface and resulting phase difference between the two beams (black). The simulation is based on formula (13).

As perfect alignment of the sample beams is challenging, the next chapter will deal with simulated misalignments and their effect on the phase difference curve and the possible countermeasures to minimize the influence of these effects on the quantitative measurements.

2.2 Simulation of misalignments between the sample beams

The aim of this chapter is to determine a quantitative procedure to relate the measured phase differences between beam A and B and to the true height change of a sample structure and to simulate the influence of misalignments on the phase measurement. Furthermore, the influence of the focal spot diameters on the evaluation as well as probable misalignments are simulated.

The measured phase difference of two perfectly aligned beams that scan transversally over a perfectly vertical step is approximated by a differential function of two hyperbolic tangent functions with different coefficients a,b and same amplitude A.

$$\Delta\varphi(x) = \varphi_A(x) - \varphi_B(x) = A \cdot [\tanh(ax) - \tanh(bx)] \qquad (14)$$

A…half step size of the structure (in degrees)

a…slope of the beam A with sharp focus

b…slope of the beam B with wide focus

As the beams interact with the vertical step on a transversal path length that is approximately determined by the focal spot diameters $\Delta\bar{x}_i$ of the beams, the beam diameters can be related to the slopes of the simulated phase signals:

$$\varphi_A\left(\frac{-\Delta\bar{x}_a}{2}\right) = A \cdot \tanh\left(-\frac{a\Delta\bar{x}_a}{2}\right) = -\frac{A}{2} \Rightarrow a = -\frac{2}{\Delta\bar{x}_a}\,\text{artanh}\,(-0.5) \qquad (15a)$$

$$\varphi_B\left(\frac{-\Delta\bar{x}_b}{2}\right) = A \cdot \tanh\left(-\frac{b\Delta\bar{x}_b}{2}\right) = -\frac{A}{2} \Rightarrow b = -\frac{2}{\Delta\bar{x}_b}\,\text{artanh}\,(-0.5) \qquad (15b)$$

As shown in equations 15a and 15b, the slopes a,b are calculated from the transversal resolutions $\Delta\bar{x}_a, \Delta\bar{x}_b$ and the focal spot ratio of the diameters is reflected in the simulation by:

$$FSR = \frac{\Delta\bar{x}_b}{\Delta\bar{x}_a} = \frac{a}{b} \qquad (15c)$$

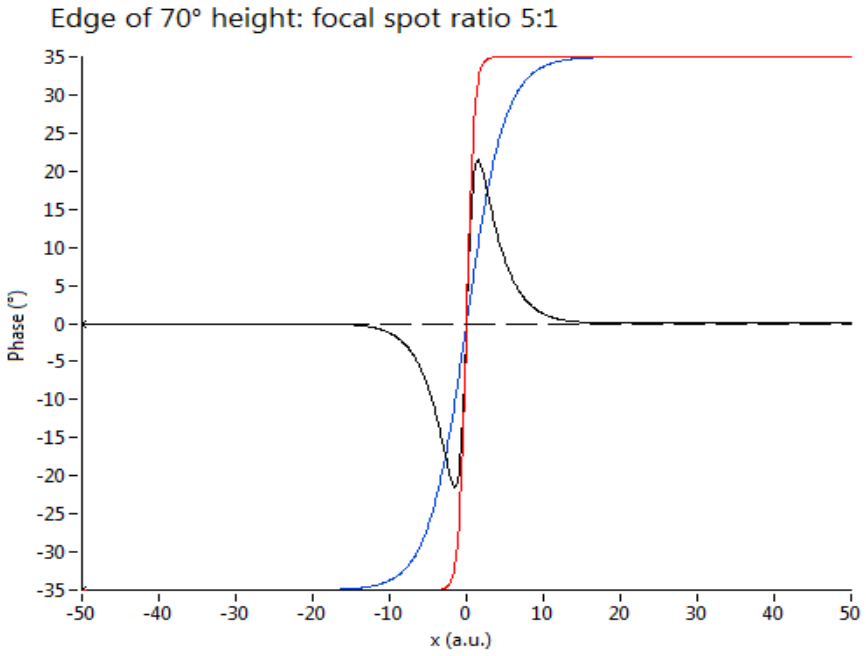

Figure 11: Simulated phase change of beams A (red) and B (blue) when the beams are moved over a step size corresponding to a phase change of 70°. The phase difference between the two beams is displayed in black. A correction factor K=1.63 was found between the absolute phase change (70°) and the phase difference signal (43°).

As can be seen in Fig. 11, the change in the differential phase signal does not reflect the true step size. Thus, a conversion factor K is needed to recalculate the actual step size. The hyperbolic tangent function reflects the windowing property of the phase difference function well, as the interaction of the beam with the step (and associated phase change) is strongly influenced by the focal spot diameter of each beam.

2.2.1 Impact of focal spot ratio (FSR) on the conversion factor

If the FSR is smaller, the amplitude of the change in the phase difference signal becomes smaller. This can be clearly seen by comparing the phase difference signals in Figs. 11 and 12. On one hand, a low resolution of the large beam might be beneficial in terms of SNR, on the other hand, adjacent structures might influence the reference that is subtracted, distorting the phase difference signal observed from the step.

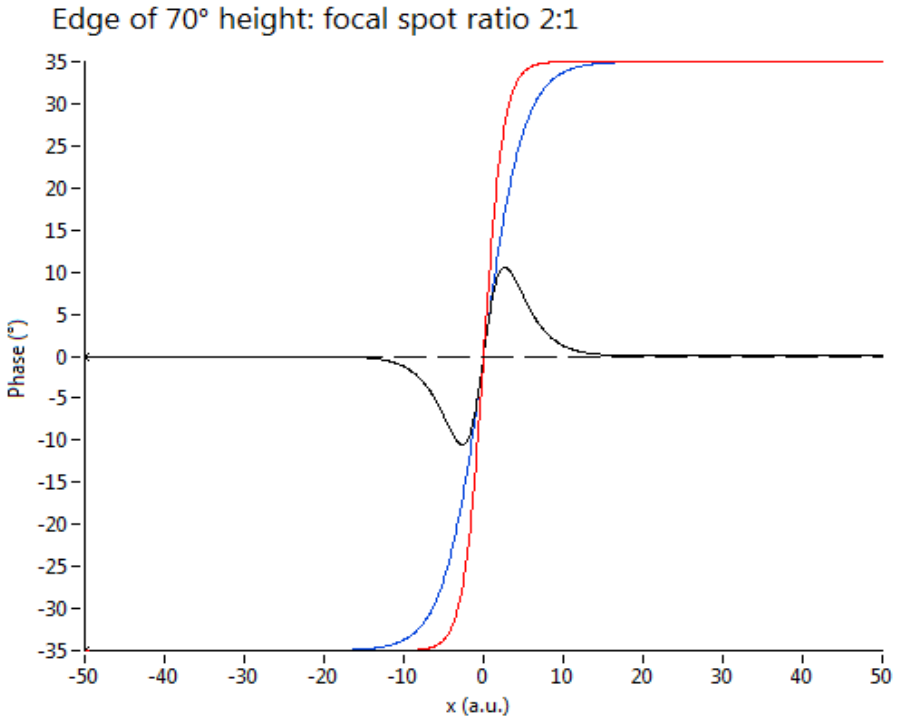

Figure 12: Simulated phase change of beam A (red) and B (blue) when the beams are moved over a step size corresponding to a phase change of 70°. The phase difference between the two beams is displayed in black. The FSR is much smaller than in the case of Fig. 11. Thus, a correction factor of K=3.33 was found between the absolute phase change (70°) and the change of the phase difference signal (21°).

2.2.2 Influence of a beam displacement

In the following, the influence of a potential misalignment between the two beams is investigated. An angular deviation between the collimated beams before the lens results for example in a lateral beam displacement of the focal spots at the sample. If the spots are displaced in direction of the evaluation axis x, a simple lateral offset between the beams can be used for the simulation:

$$\Delta\varphi(x) = \varphi_A(x) - \varphi_B(x) = A \cdot [\tanh(ax) - \tanh(b(x+c))] \qquad (16)$$

A…half step size of the structure (in degrees)

a…slope of the beam A with sharp focus

b…slope of the beam B with wide focus

c…lateral displacement of the beam

The phase difference signal now shows an asymmetry, as can be seen in Fig. 13.

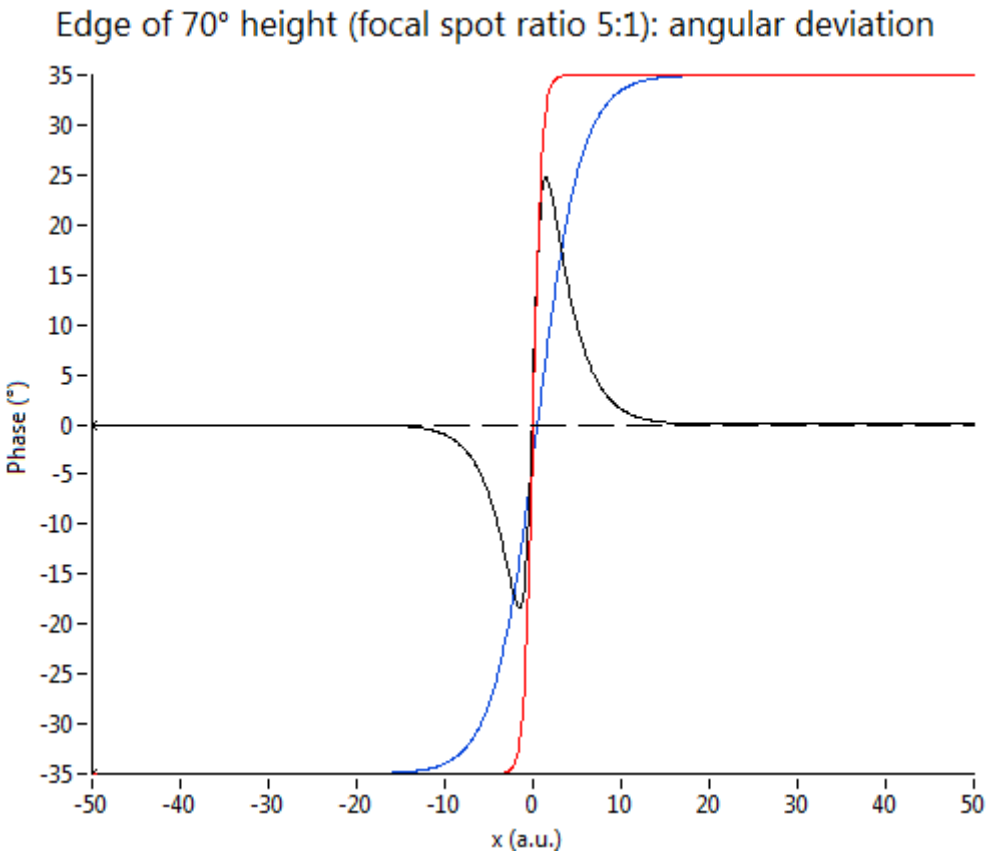

Figure 13: Simulated phase change of beam A (red) and B (blue) when the beams are moved over a step size corresponding to a phase change of 70°. The blue beam is laterally displaced in x-direction by 0.5 units with respect to the red beam. The FSR is 5:1. A correction factor of K=1.62 as in Fig. 11 was found between the absolute phase change (70°) and the change of the phase difference signal (43°).

A beam displacement orthogonally to the scanning axis (displacement along y-direction) reduces the cross-section area of the larger spot size with the edge resulting in a steeper step function in comparison to the non-displaced beam. This results in a similar behavior as a smaller focal spot ratio (cf. Fig. 12).

2.2.3 Parallel displacement of the beams and scanner (pivot point mismatch)

If the collimated beams are displaced parallel to each other before they hit the x-scanner, one beam mishits the rotation axis of the scanner (pivot point) and will therefore undergo an additional phase change evoked by the scanner. This pivot point mismatch will be discussed later in chapter C1.3.

For the simulation, a linear phase term is introduced for one beam (with the pivot point mismatch) that increases linearly with the scanning angle and therefore with the lateral position x (Eq. 17). As illustrated in Fig. 14, this linear phase term also affects the phase difference and tilts the differential phase function.

$$\Delta\varphi(x) = \varphi_A(x) - \varphi_B(x) = A \cdot [\tanh(ax) - \tanh(bx)] + d \cdot x \qquad (17)$$

A…half step size of the structure (in degrees)

a…slope of the beam A with small focal spot

b…slope of the beam B with large focal spot

d…linear phase factor because of a pivot point mismatch of beam A

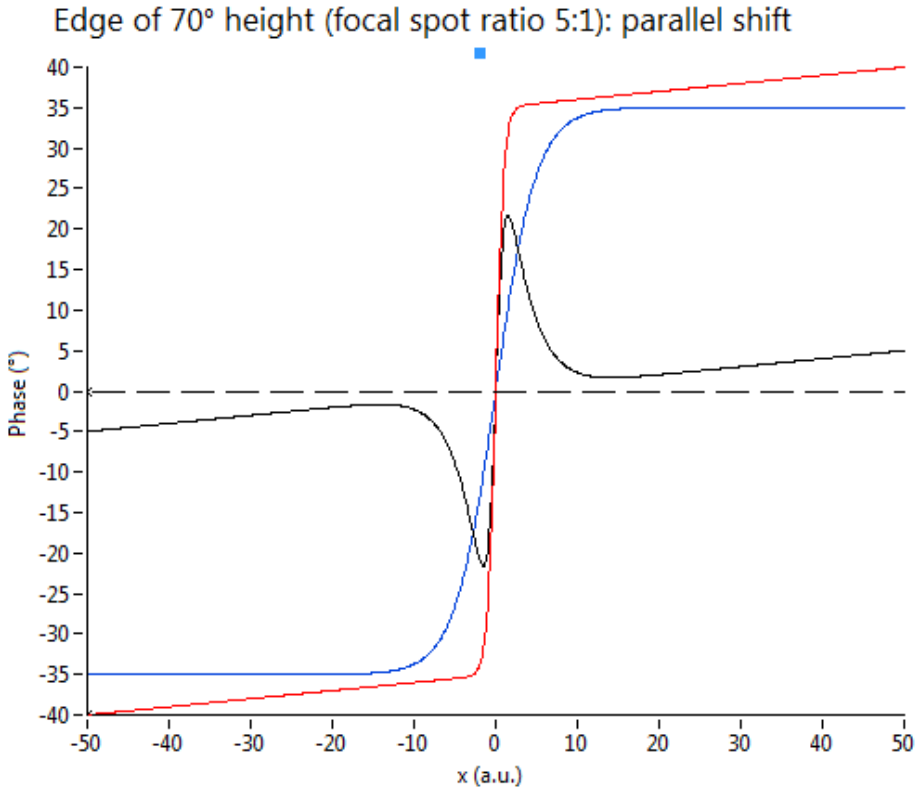

Figure 14: Simulated phase change of beam A (red) and B (blue) when the beams are moved over a step size corresponding to a phase change of 70°. The FSR is 5:1. The phase difference between the two beams is displayed in black. Beam A is incident with an offset to the pivot point of the scanner which results in an additional linear phase term along the x-direction. A conversion factor of K= 1.61 was retrieved from this simulation.

Consequently, a general formula for simulation has to reflect both, a parallel displacement and an angular deviation, and is given by:

$$\Delta\varphi(x) = A \cdot [\tanh(ax) - \tanh(b(x + c))] + d \cdot x \qquad (18)$$

A…half step size of the structure (in degrees)

a…slope of the beam A with small focal spot

b…slope of the beam B with large focal spot

c…lateral displacement of the beam B due to an angular deviation before the sample lens

d…linear phase factor because of a pivot point mismatch of beam A

2.2.4 Large lateral displacement between the beams

A large lateral displacement of the focal spots caused by a parallel shift between the collimated beams means that the focal spots are not overlapping anymore. In this case, the principle of the method will be different and similar to another differential phase sensitive method that is based on two laterally displaced beams [21]. For extended interfaces (such as a glass plate) a stable phase difference between the beams can be achieved (which will not be the case in scattering objects). The jump in the phase difference signal can then be directly converted to the height of the step (cf. Fig. 15).

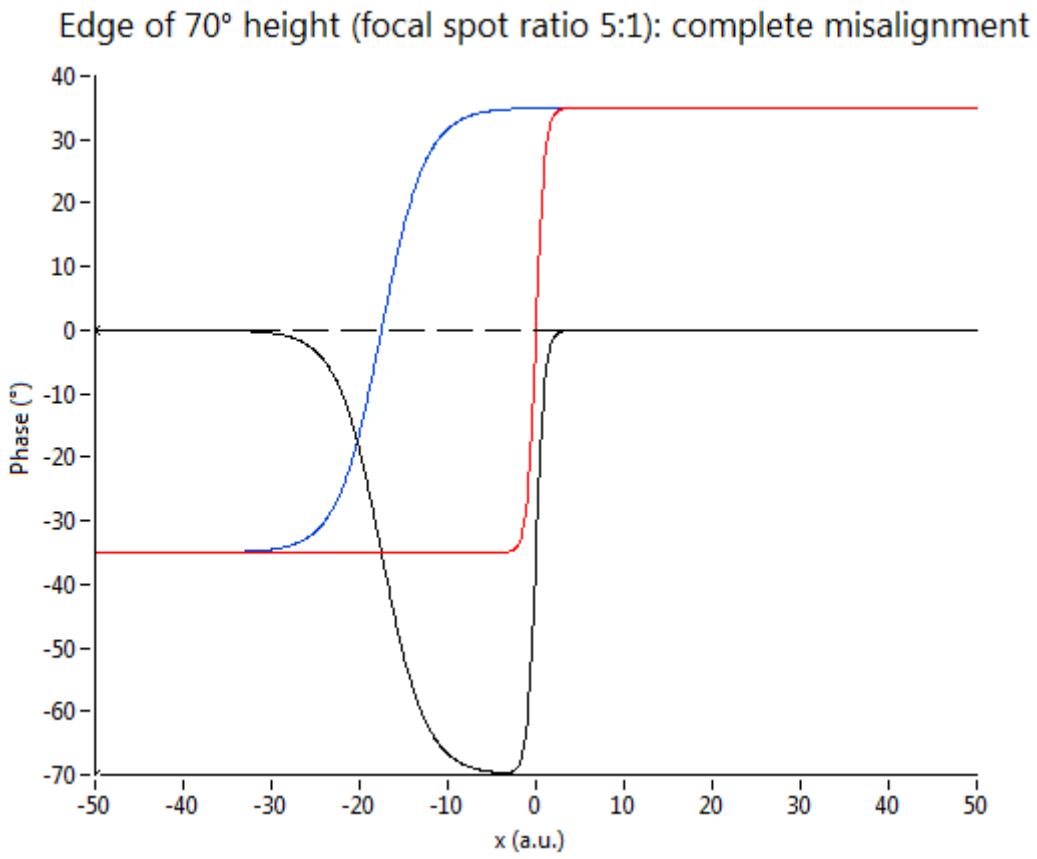

Figure 15: Simulated phase change of beam A (red) and B (blue) when the beams are moved over a step size corresponding to a phase change of 70°. The phase difference between the two beams is displayed in black. Because of the complete lateral separation of the beams, the phase difference signal is changed and allows for a direct estimation of the step size (conversion factor K=1).

2.3 Simulation of imperfect sample structures

2.3.1 Influence of the step steepness

As described in chapter 2.1, the zone of interaction (ZOI) between a perfect vertical step and the beams is determined by the focal spot diameters of the beams $ZOI_i = \Delta\bar{x}_i$. If the step is not perfectly vertical but flattened, the zone of interaction (ZOI) of both beams is increased by the lateral expansion of the step, as can be seen in Fig. 16.

In the simulation, this is reflected by an interval on the x-axis that is extended by the extension of the edge for both beams. For the phase function of the smaller beam $\varphi_A(x) = \tanh(ax)$ this means a more pronounced decrease of the slope than for the phase function of the larger beam $\varphi_B(x) = \tanh(bx)$. Therefore, a flattened edge has a similar impact on the phase difference function as a reduced ratio of coefficients $\frac{a}{b}$ (cf. Fig. 17). In addition, the phase difference function is broadened compared to the sharp edge.

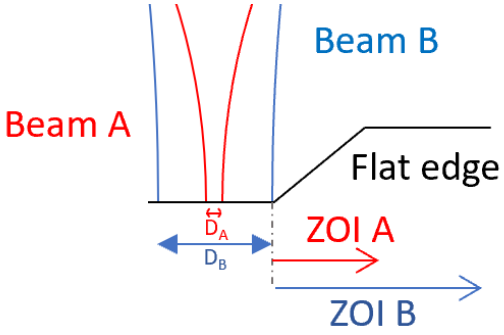

Figure 16: Illustration of the beam geometry for a flattened edge. The zone of interaction (ZOI) of beams A and B in Fig. 9 was limited by their focal spot diameters in case of a perfectly steep edge. If the edge is flattened, the zone of interaction of beam A increases by a higher factor than the ZOI of beam B. This results in slopes that are more equal for the flat edge than for the perfect edge.

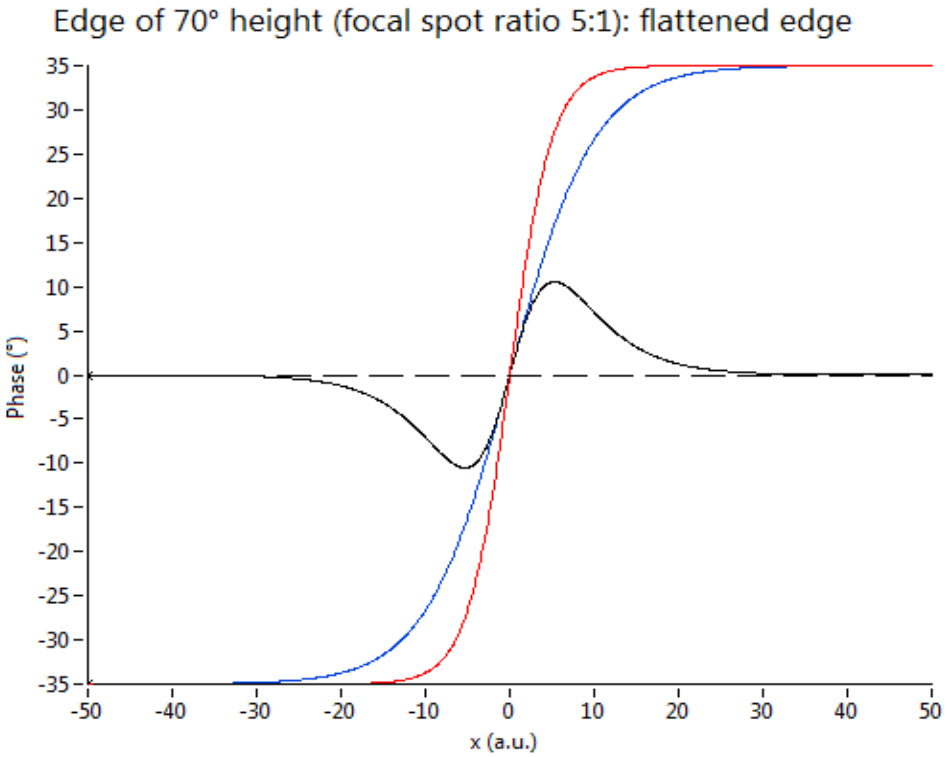

Figure 17: Simulated phase change of beam A (red) and B (blue) when the beams are moved over a flattened step corresponding to a phase change of 70° (edge angle =70° instead of 90°). The phase difference between the two beams is displayed in black. The flattened edge results in a lower differential phase signal and thus leads to a higher conversion factor (K=2.57) as compared to a perfectly sharp edge (cf. Fig.11).

2.3.2 Influence of the angle between scanning direction and edge

As the scanning beams in general do not cross the edge perpendicularly, but the scanning direction of the beams and the orientation of the edge form an angle smaller than 90°, the ZOI is extended for both beams, which is illustrated in Fig. 18.

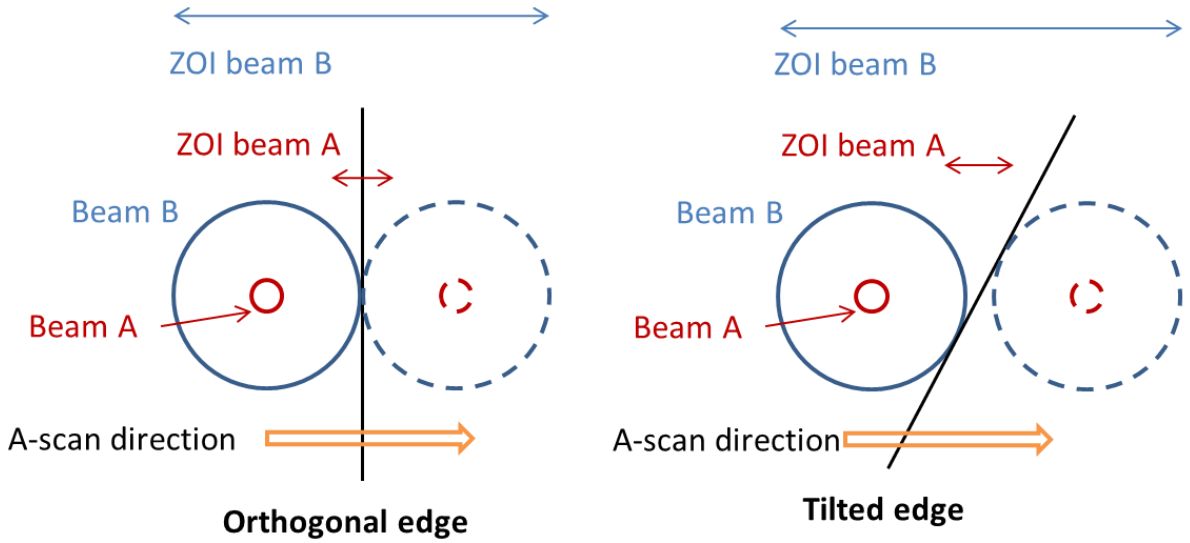

Figure 18: Illustration of the beam geometry for a tilted edge. The zone of interaction (ZOI) of beams A and B in Fig. 9 was limited by their focal spot diameters in case of a perfectly orthogonal edge. If the edge is tilted, the zones of interaction (ZOI) of beams A and B increase by the same factor.

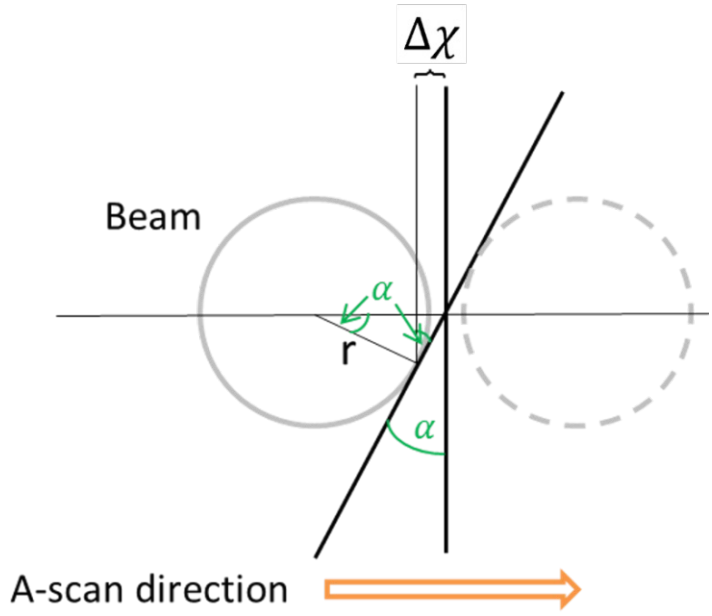

Figure 19: Illustration of the impact of the tilted edge on the ZOI. The zone of interaction increases by 2 elements $\Delta\chi$

The increase of the ZOI $2\Delta\chi$ in dependence of the angle of the edge with respect to the vertical line **α** is illustrated in Fig. 19. The increase is proportional to the radii of focal spots and the angle of the edge with respect to the vertical line and is given by:

$$2\Delta\chi = 2\,\mathrm{r}\,\sin(\alpha)\tan(\alpha) = \Delta\bar{x}\,\sin(\alpha)\tan(\alpha) \qquad (19)$$

Resulting in a new ZOI of

$$\Delta\bar{x} + 2\Delta\chi = \Delta\bar{x}\,[1 + \sin(\alpha)\tan(\alpha)] \qquad (20)$$

For the simulation, the intervals, where the phase functions of the beams increase, are multiplied by the factor $[1 + \sin(\alpha)\tan(\alpha)]$, and consequently both slopes are reduced by that factor.

The phase differential signal of a tilted edge in comparison to an orthogonal edge is shown in Fig. 20.

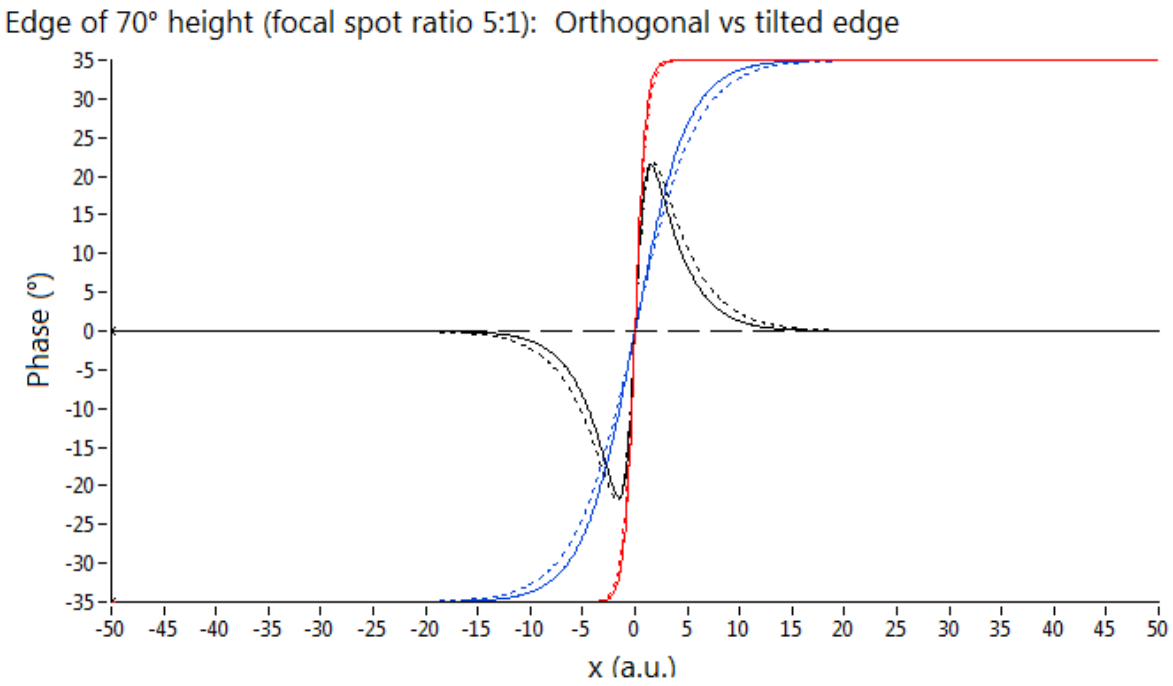

Figure 20: Comparison of the phase change of beam A (red) and B(blue), when the beams are moved over an edge orientated orthogonally with respect to the scanning direction and an edge forming an angle of 60° with the scanning direction (α=30°), corresponding to a phase change of 70°. The phase difference between the two beams is displayed in black.
The solid lines represent the orthogonal edge and the dotted lines the tilted edge. The conversion factor remains the same for both, orthogonal and tilted edge, but the phase difference function is broadened for the tilted edge in comparison to the orthogonal edge.

Conclusions retrieved from the simulations presented in this chapter:

As long as the two beam spots overlap, an edge on the sample is expressed in the phase difference signal as a signal that shows first an upwards then a downwards peak (or the reverse) and the principle theoretically works.

A parallel shift between the beams results in an additional linear phase term (introduced by the off-pivot point illumination of the scanner) that influences the quantitative evaluation of the step size.

An angle between the two beams in a direction orthogonal to the scanning direction results in a focal spot displacement, that causes a reduced focal spot ratio and thereby a reduced amplitude of the phase difference signal.

A flattened edge causes a reduced amplitude and a broadening of the signal of the phase difference that needs to be considered for recalculating the true step size from the amplitude of the phase difference signal.

A tilted edge causes a broadening of the signal of the phase difference but does not change the amplitude.

C. Methods

This chapter deals with the practical realization of the experimental setup as well as the necessary data evaluation steps.

1) The DPC-PSOCT system

In this work a polarization sensitive OCT (PSOCT) system, which was available from previous work [18], was adapted. The two sample beams are realized by installing a polarization sensitive Mach-Zehnder interferometer type configuration in the sample arm that splits the incoming polarized light into two independent beams of different beam diameter that are encoded in two orthogonal polarization states. At the Mach Zehnder exit, these two beams are recombined, are directed to a x-y scanning unit and illuminate the sample via a lens such that one beam produces a small focal spot while the other a large focal spot. The lught returning from the sample propagates the same way back to the main interferometer. The polarization sensitive setup at the main interferometer exit allows to detect both beams independently and simultaneously.

In the following subchapters the light path, polarization state settings and further alignments of the optical elements are described that are necessary to realize the differential phase contrast polarization sensitve OCT (DPC-PSOCT) system. The final subchapter contains the specifications of the created system.

1.1 System setup

The main interferometer for OCT measurements is based on single mode fibers that are birefringent. Thus, the polarization state of the light undergoes changes when light travels through the fiber, depending on temperature and bending of the fiber. Polarization control paddles (PC) allow modifications of the polarization state by applying deterministic bending on the fiber and can be used to compensate for the fiber induced birefringence as well as to set up desired polarization states.

Fig. 21 shows a schematic representation of the experimental setup.

The light source is a tunable laser source (Axsun Technologies Inc., 1060 Swept Laser Engine) operated at a central wavelength of 1045 nm, a sweep range of 100 nm (10 dB drop-off) and a sweep rate of 100 kHz [22].

The outgoing light is linearly polarized by travelling through the polarization paddles PC1 and a linear polarizer, then passes a fiber based beam splitter FB-BS1 (50:50), where half of the light power is lost, and enters the fiber based Michelson interferometer at FB-BS2. The

light is split into equal portions entering reference and sample arm. The sample beam´s input polarization state is set by PC2 in a way that two beams of equal power after the polarization sensitve separation at PBS1 are created.

Between PBS1 and PBS2 the light runs through a Mach-Zehnder interferometer type configuration, but as both channels of the interferometer are orthogonally polarized interference between the channels is prevented. After PBS1 one beam is expanded, while the other is narrowed. At PBS2 both beams are reunited and exit the interferometer co-linearly with different beam diameters. A galvanometer scanner (GS) unit provides a rectangular scanning field. The beams are then focused onto the sample using an achromatic lens resulting in concentric beam focal spots of different size, respectively lateral resolution.

After backscattering from the sample, both sample beams are brought to interference with the reference beam at beam splitter FB-BS2 and the interference signal exits the Michelson interferometer on two paths, whereby both interference signals are phase-shifted by π.

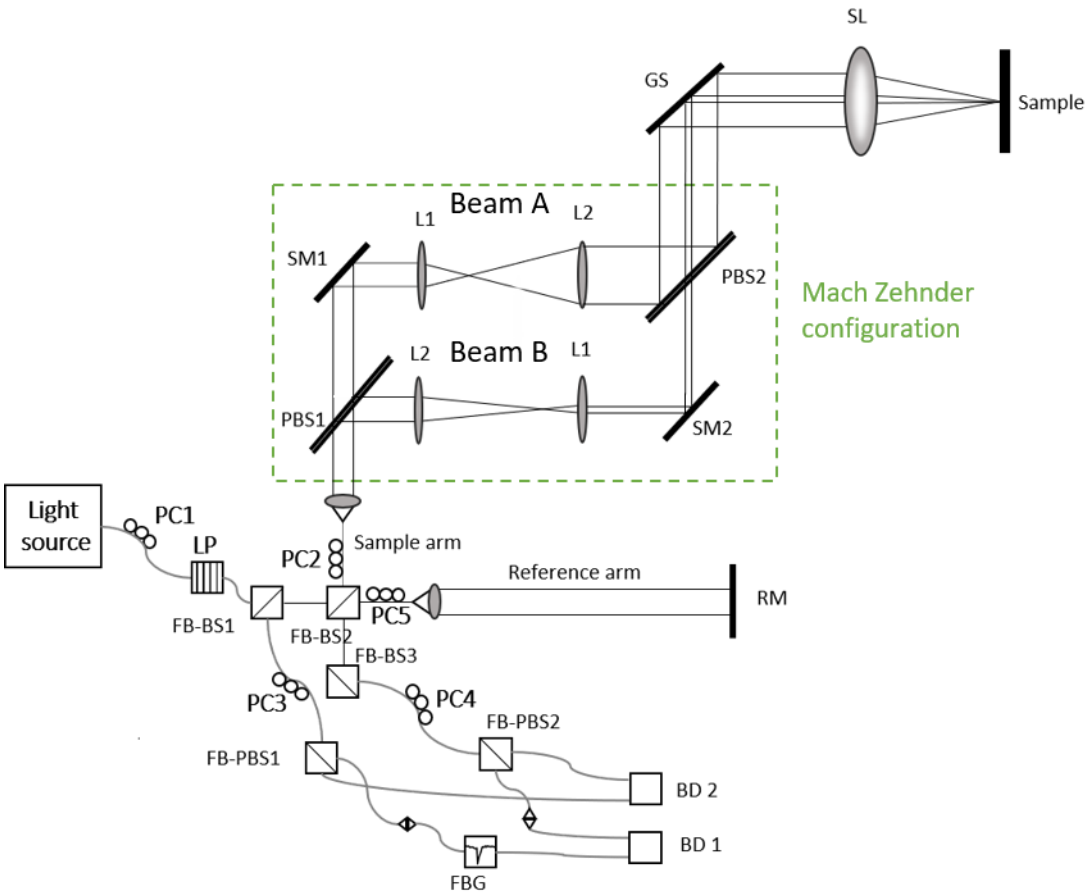

Figure 21: Scheme of the experimental setup: LP…linear polarizer, PC…polarization control paddles, FB-BS…fiber based beam splitter (50:50), FB-PBS…polarizing beam splitter (50:50), PBS…(free space) polarizing beam splitter (50:50), L1…convex lens (f=20mm), L2…achromatic lens (f=50mm), SL…sample lens (achromatic, f=50mm), SM…sample mirror, RM…reference mirror, GS…galvanometer scanner, FBG…fiber Bragg grating,

The light will then travel through FB-BS1(or FB-BS3), PC3 (or PC4) and be separated at FB-PBS1 (or FB-PBS2) into the two orthogonal polarization states. Finally, the light in both

orthogonal polarization states is each detected by the balanced detectors BD1 and BD2 (Thorlabs Inc., PDB 460C) respectively.

As both beams from the two exits of the main fiber based Micheslon interferometer are phase-shifted by π, subtraction of the detected signal allows to double the signal intensity while eliminating noise and auto interference components, which is called “balanced detection” or “balancing”.

In one polarization channel a fiber-Bragg-grating (FBG) was implemented in order to compensate for A-scan trigger jitter of the light source, which will be explained in Chapter C2.2.1.

Fig. 22 shows a photograph of the sample arm. In order to minimize potential motion that introduces phase jitter between the two sample arm paths, all the components of the Mach-Zehnder type configuration are rigidly connected by rods. To further enhance the stability, all components are screwed on a base plate. As can be seen in Fig. 22, PBS2 is placed on a specifically designed mount for a good fine adjustment possibility while maintaining stable and rigid with the rest of the steup at the same time.

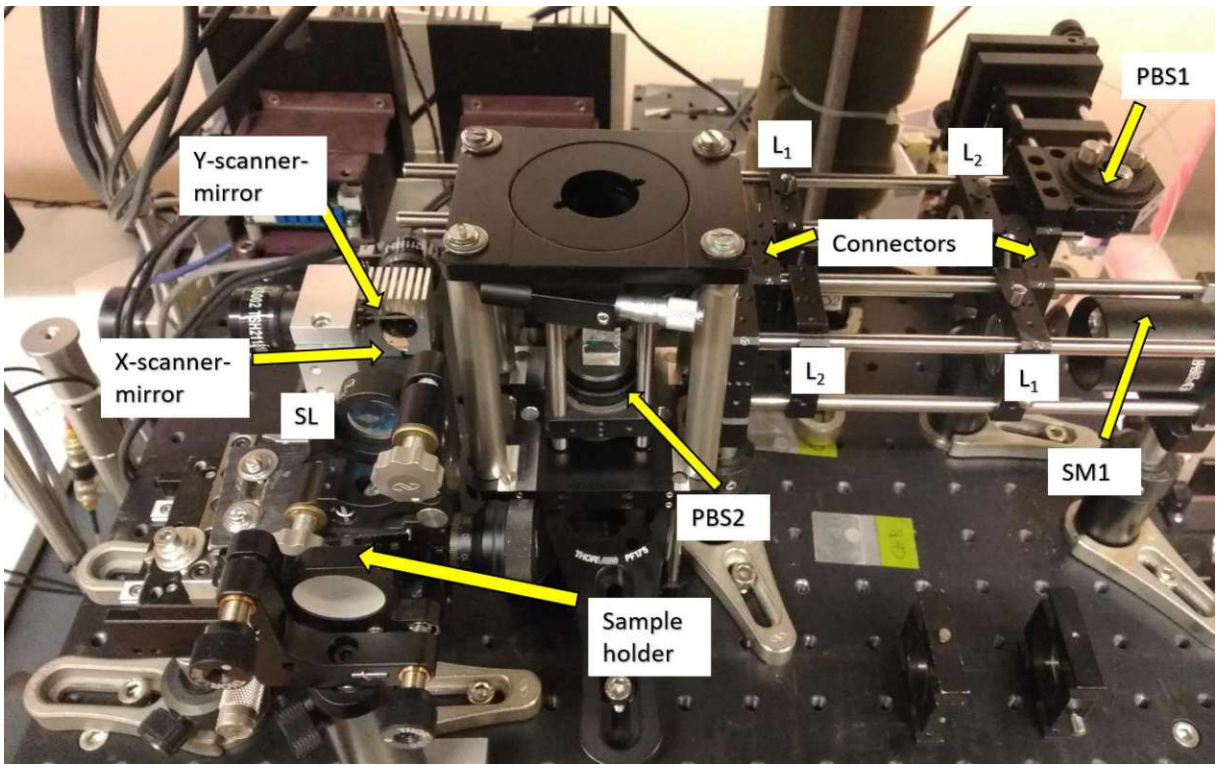

Figure 22: Picture of the Mach-Zehnder type configuration that is placed in the sample arm of the system. In order to achieve high phase stability, the components are screwed on a plate and connected with rods. Sample lens SL and polarizing beam splitter PBS2 need to be placed on adjustable mounts for system alignment.

1.2 Alignment procedure of the polarization control paddles

The outgoing light gets a preferred polarization state by passing through the polarization paddles PC1. A defined linear state is obtained by traversing a linear polarizer (LP, OZ Optics Ltd.) that only allows light polarized parallel to its vertical transmission axis to pass. The polarization paddles PC1 are aligned in a way that the main axis of the polarization state impinging on the polarizer and its transmission axis coincide, hence the power that passes the polarizer is maximized.

Now the sample arm is aligned: For this purpose a mirror is placed at the sample position and the reference arm is blocked. The input state for the Mach-Zehnder interferometer type configuration is set to a linear polarization state with an axis of 45° with respect to the horizontal (corresponding to a diagonal polarization state) by aligning the polarization control paddles PC2. Two sample beams of equal intensity, one in a horizontal and one in a vertical polarization state are obtained after passing through the Mach-Zehnder type configuration. Both beams are reflected by the mirror and enter the fiber based main interferometer.

Both polarization states are altered by birefringence introduced by PC2 as well as the other fiber components. To compensate for that, the next step is to set the polarization control paddles PC3 and PC4 in a way that the light from both beams is separated into the two channels of the polarization sensitive detection unit. Thus, no light from the sample arm is measured at the horizontal polarized light detector when only the horizontal sample beam is blocked in the Mach-Zehnder interferometer type configuration.

This means, that after alignment of PC3 and PC4 one beam (=one polarization state) is now directed to the two inputs of BD1 while the other beam is directed to the inputs of BD2.

Finally, the polarizatoin state in the reference arm is aligned. This is set by aligning the polarization paddles PC5 in such a way that the reference light in both polarization channels is of equal intensity.

1.3 Alignment procedure of the sample lens and pivot point of the scanner

A galvanometer scanner in combination with a convex lens creates a rectangular scanning field for the imaging beam. The x-scanner is driven by a field programmable gate array (FPGA) and is synchronized with the A-scan trigger that is delivered by the light source. The scanner moves the beam laterally one small step over the sample whenever a depth scan (A-scan) is completed. After the x-scanner has completed a line of depth scans (B-scan), the y-scanner moves the beam one step vertically. Thereby horizontal line scans add up vertically to a rectangular scanning field.

The following adjustments are done using only the sample beam that traverses the last polarizing beam splitter (PBS2 in Fig.18) in the sample arm, as it remains unaffected by additional beam adjustments. These will be necessary to align the second beam in respect to the first one in order to create co-linearity between the beams. For this alingmnet procedure, a mirror is placed at the sample position.

The pivot point of the scanner is the position on the scanner mirror that corresponds to its rotation axis.

The beam has to impinge onto the pivot point of the x-scanner in order to avoid phase changes introduced by the scanning of the beam. In addition, the scanner needs to be positioned in the the focal plane of the sample lens, in order to guarantee parallel beams incident on the sample during scanning.

The generation of a line scan by x-scanner movement is illustrated in Fig. 23.

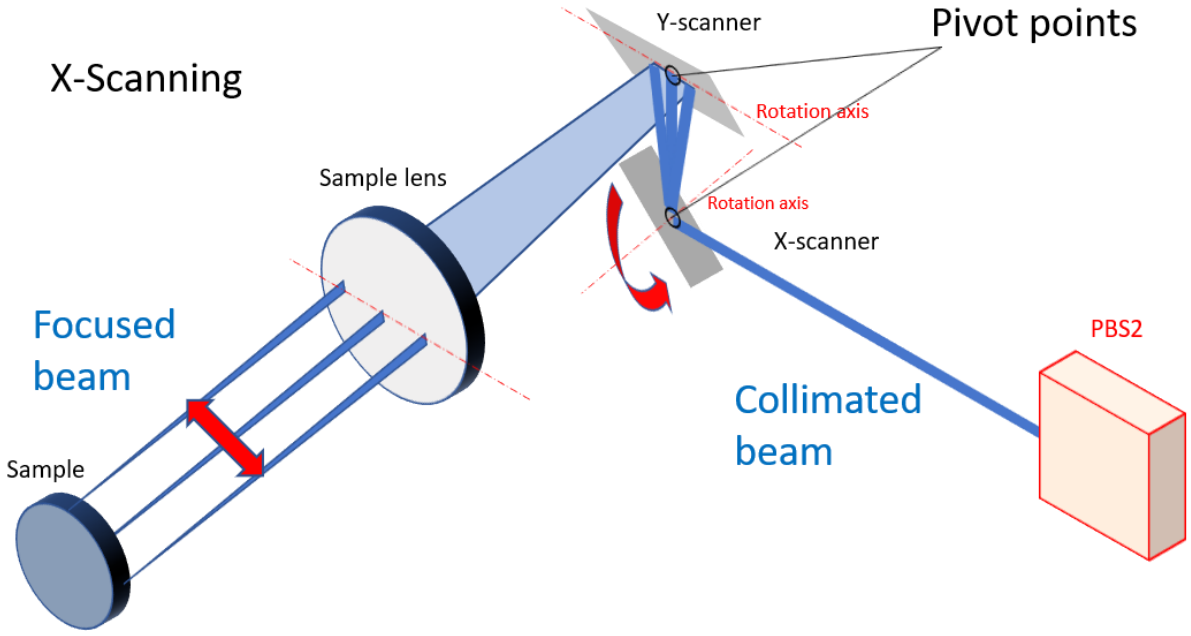

Figure 23: Scheme of the galvanometer scanner geometry for performing a B-scan (horizontal cross section of the sample) by x-scanner rotation. The pivot point of the x-scanner is located in the back focal plane of the sample lens.

If the incident collimated beam does not impinge on the pivot point of the x-scanner, the beams will not travel the same path length to the sample (Fig. 24). Thus, an additional phase change that depends on the scanner rotation angle is introduced.

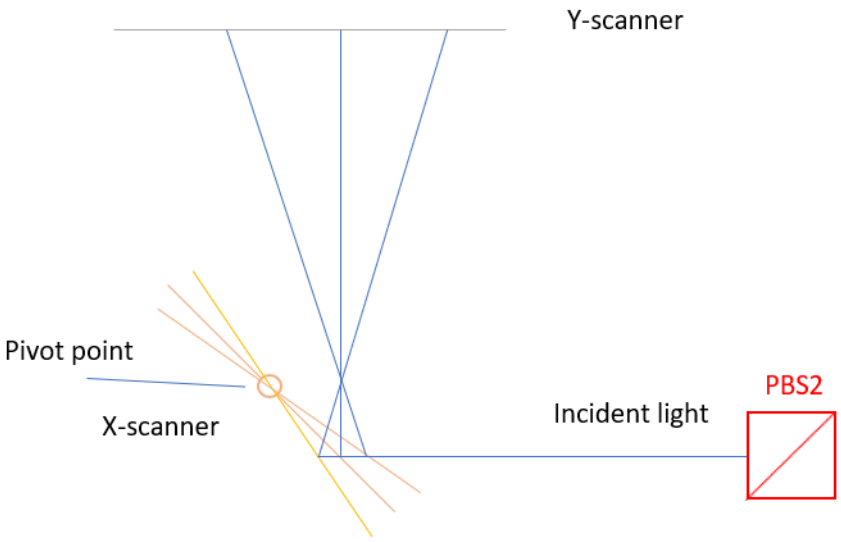

Figure 24: Scheme of a situation where the incident beam impinges on the x-scanner below the pivot point. The optical path length between PBS2 and the sample is shorter for flat angles between x-scanner and incident light.

Another aspect are deviations from the focal distance between pivot point of the scanner and the sample lens, as shown in Fig. 25. If the scanner mirror rotation axis is not placed in the focal point of the lens, the collimated beams are not coupled back into the exact same point of the scanner where they originated from if the sample is a mirror. The back coupled light faces a decrease in intensity and a phase shift increasing with the scanning angle of the beam with respect to the optical axis.

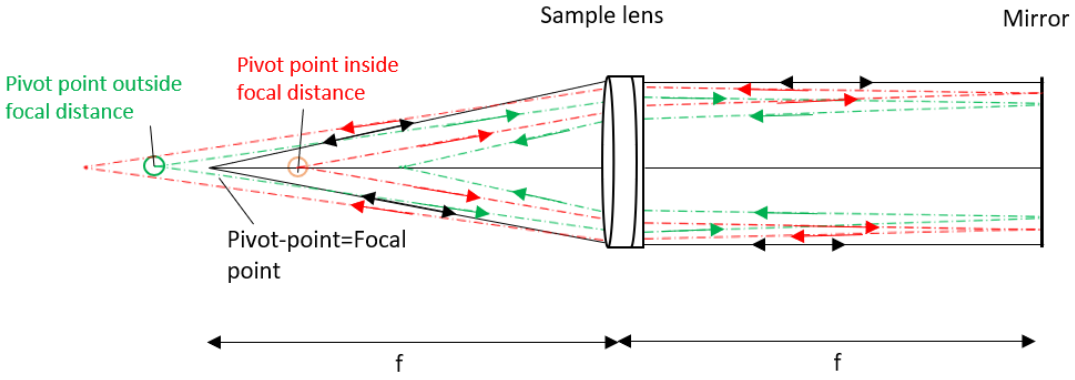

Figure 25: Illustration of the effect of a misplacement of the pivot point of the scanner in respect to the focal plane of the lens. The returning light is tilted with respect to the incident light and only a reduced portion of the light will couple back into the sample arm. Furthermore, a phase-shift will be introduced, as off-axis-beams face a stronger deviation and consequently longer path lengths.

Therefore, it is important that the pivot point of the x-scanner is located in the focal plane of the lens in order to create a line scan with constant phase and intensity.

In order to scan through a sample, the y-scanner is moved as well and shifts the horizontal line-scan through the sample, as shown in Fig. 26. This will introduce path length differences between y-scanner and lens. As the focal condition is already fulfilled for the x-scanner, it

cannot be fulfilled for the y-scanner. Consequently, an intensity loss as well as a linear phase-shift is evoked by the vertical beam movement.

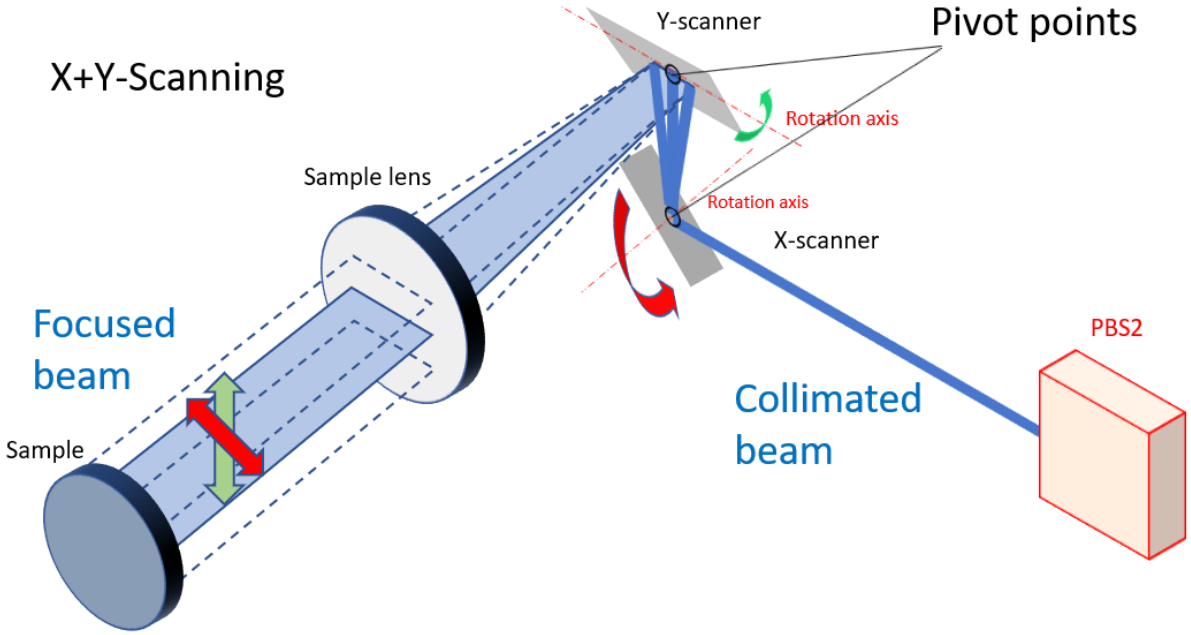

Figure 26: Scheme of 3D scanning of the sample. X-scanner movement is shown with red arrows, y-scanner movement is shown with green arrows.

A setup where the x-scanning and y-scanning are decoupled would allow for the required positioning of pivot point and focal point for both scanners.

One way to realize that is to place a telescope between x-scanner and y-scanner, as presented in [14].

For precise alignment of the pivot point in the current setup, a liveview-tool program was written that is able to detect small misalignments of the pivot point of the x-scanner. This routine will be described in chapter C3.

If the alignment of the pivot point and the sample lens is completed, the two beam alignment is the next step to set up the optical system.

1.4 Alignment procedure of the sample beams

The collinear alignment of both sample beams is the main challenge of the experimental setup. The last sample mirror SM2 and polarizing beam splitter PBS2 in the sample arm (cf. Fig. 21) can be used to align the second beam in respect to the first in such a way that both beams exit the Mach-Zehnder interferometer collinearly. The collinearity is analyzed using a beam profiling-camera, placed in the back focal plane of the sample lens. In order to achieve collinearity, two possible types of misalignments have to be overcome: angular deviation and parallel shift between the beams, as outlined in Fig. 27.

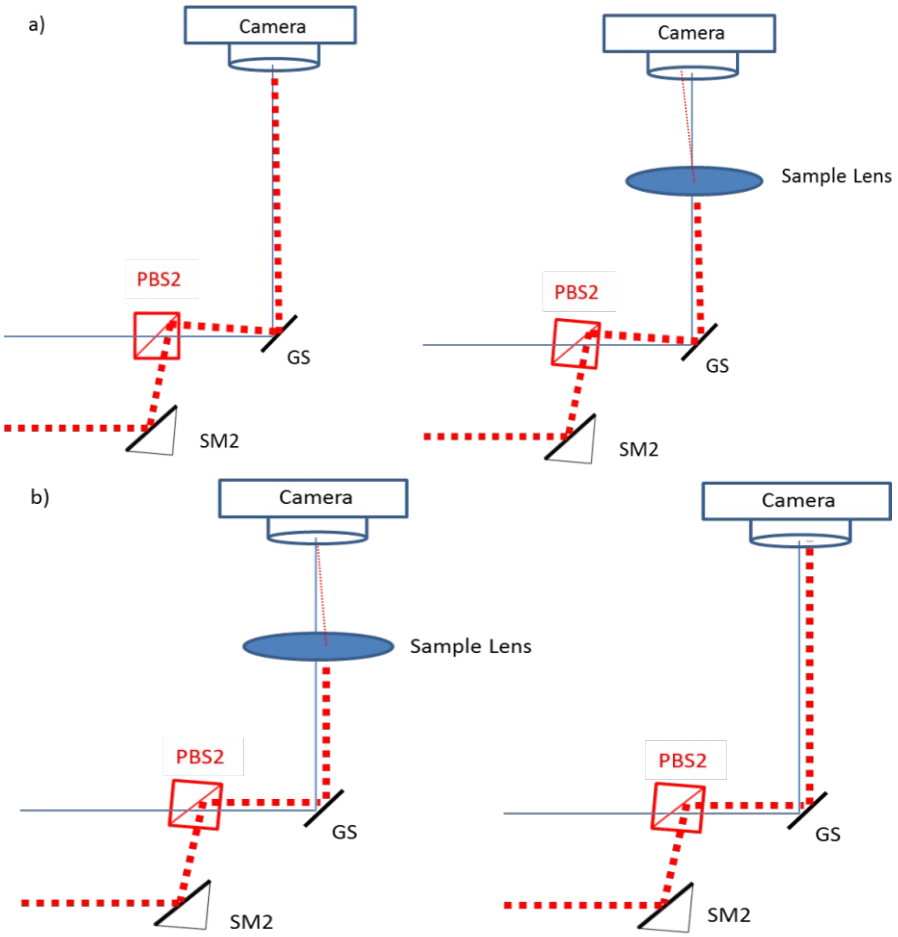

Figure 27: Schemes of the alignment procedure for achieving collinearity between both beams. a) Placing a sample lens into the beam path allows detection of angular deviation between the beams. b) Removing the sample lens allows detection of a parallel shift between the beams (blue line: path of beam 1, red dashed line: path of beam 2).

Angular deviation between the beams can be measured by placing a convex lens in the exiting beam path (Fig. 27a). An angle between the two beams results in a transversal shift of the two focal spots generated by the lens that can be measured by the camera. Parallel beams are focused into the same focal spot, so a parallel shift remains undetected in this configuration and has to be checked in a separate step by removing the sample lens and checking if the two beams are overlapping (Fig. 27b).

In order to provide collinearity of both beams, two criteria have to be satisfied: both beams have to origin from the same location at the dielectric plane inside PBS2 and the plane has to be tilted in a way that it reflects the second beam in the same direction as the other beam is transmitted (no angular displacement between the beams, cf. Fig. 28).

The alignment procedure starts by creating parallelism between the beams by aligning PBS2. Using the lens in front of the beam profile camera, PBS2 is tilted until both focal spots (generated by the two beams) are overlapping (Fig. 28a).

In a second step, the lens is removed, and the beams are in general parallel shifted (a displacement between the beams can be observed on the camera), because they initially originate from different locations at PBS2. In order to correct for this misalignment, the mirror SM2 has to be tilted (Fig. 28b). However, this introduces an angular deviation between the beams. Therefore, the alignment steps have to be repeated until a minimum angular deviation as well as parallel shift between the beams is observed.

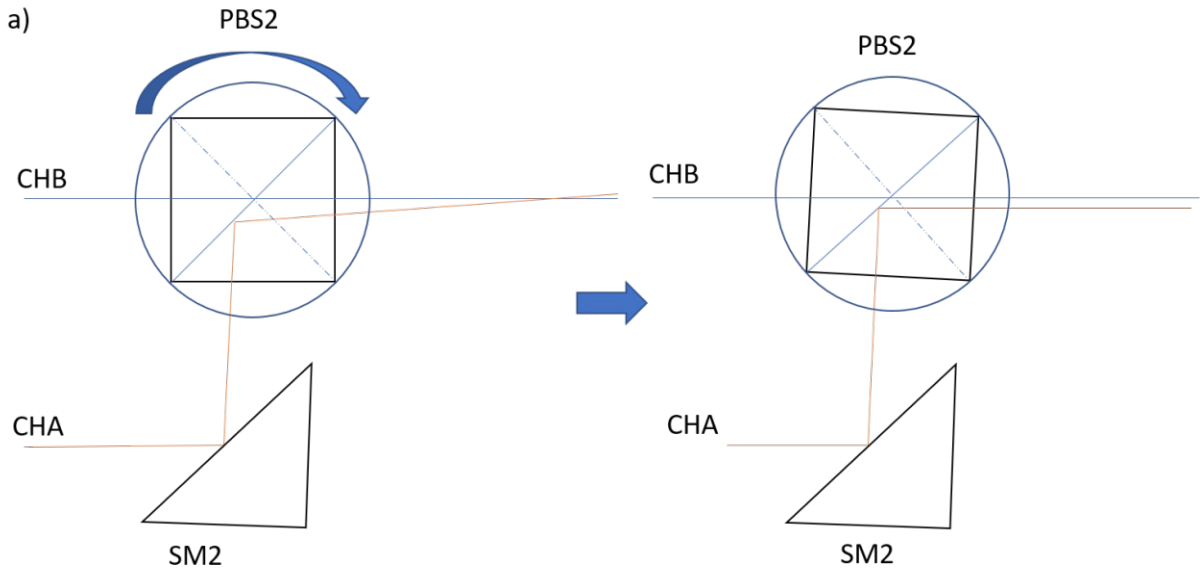

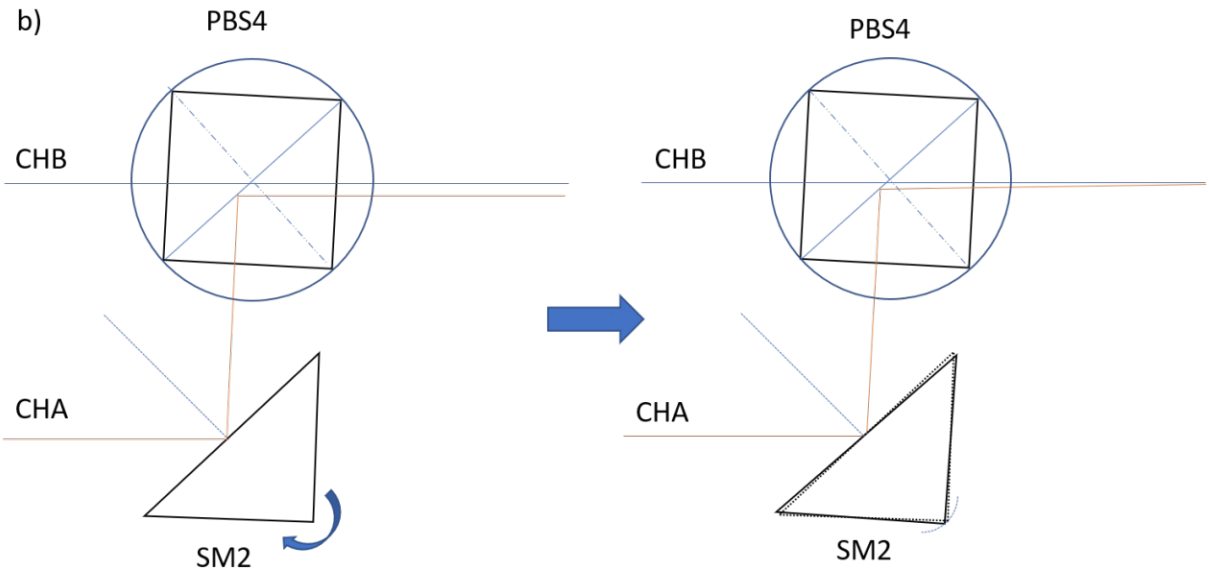

Figure 28: Scheme of the alignment procedure for generating collinear beams. a) The focal points of the two beams observed by the camera with the sample lens in place are matched by tilting/rotating PBS2 to obtain parallelism. b) In a second step the lens is removed and the sample mirror SM2 is tilted to match the point of origin of both beams inside PBS4 better. The solid line in PBS4 represents the dielectric interface, while the dotted line just serves as guidance for the center of the cube.

1.5 Characteristics of the OCT setup

After these alignment steps, the characteristics of the setup are measured and compared with theoretically calculated values. If no measured value is available, only the theoretic value is indicated.

Depth range:

The depth range is a measure of the theoretical limit in depth that can be sampled (without aliasing) and depends on the number of spectral bins N(k) that are included in the measurement. Theoretical calculation of depth range yields [23]:

$$z_{max} = \frac{N{\lambda_0}^2}{4\lambda_{full}} \tag{21}$$

$$= \frac{1510 * (1045 * 10^{-9}m)^2}{4(110 * 10^{-9}m)} = 3.748\, mm$$

With: N…maximum number of k-samples in the sweep, λ_0… central wavelength, λ_{full}…full spectral bandwidth of the wavelength sweep.

Practically the depth range was measured by placing a mirror in the sample arm. The reference arm was shifted a defined distance and thereby the displayed depth profile shifts a defined number of pixels. Thereby, a conversion factor of pixel and length can be calculated, and the depth range corresponds to the total number of pixels.

The value measured is $\mathbf{3.74\ mm}$ depth range.

Axial resolution Δz defines the minimal distance of structures that can be resolved [18] and is calculated by:

$$\Delta z = \frac{2ln2}{\pi}\frac{{\lambda_0}^2}{\lambda_{FWHM}} = \frac{2ln2}{\pi}\frac{{\lambda_0}^2 * 1.82}{\lambda_{10dB}} \tag{22}$$

$$= \frac{2ln2}{\pi}\frac{(1045 * 10^{-9}m)^2 * 1.82}{100 * 10^{-9}m} \approx 8.77\ \mu m$$

λ_{10dB}…the spectral bandwidth where the emission dropped to 1/10 of the maximum emission, and λ_{FWHM} …full width of the spectrum at half of the maximum emission, λ_0… central wavelength.

For the measurement of the axial resolution, a mirror was placed at the sample position and the conversion factor of pixels and length calculated as for the depth range. The pixel interval around the peak of the depth profile (= mirror depth position), where the signal dropped to half of the maximum intensity was measured and converted into the depth interval.

The measured value is $\mathbf{10.04\mu m}$ which is in good agreement with the theoretical value.

Collimated beam diameter

The beam diameters of channel A and B after narrowing respectively expansion of the incoming beam D_0=**2.2 mm** diameter (FWHM, value taken from [18]) are calculated to:

$$D_A = \frac{f_{L_1}}{f_{L_2}} * D_0 = \frac{50\ mm}{20\ mm} * 2.2\ mm = \mathbf{5.50\ mm}$$

$$D_B = \frac{f_{L_2}}{f_{L_1}} * D_0 = \frac{20\ mm}{50\ mm} * 2.2\ mm = \mathbf{0.88\ mm}$$

f_{L_1}, f_{L_2} … focal lengths of lens 1 and 2

Transversal resolution

The transversal resolution of the system corresponds to the smallest transversal distance resolvable by the beam and corresponds to the diameter of the Airy disc. It depends on the collimated beam diameters and the focal length of the sample lens (and is defined by the Rayleigh criterion) [19]:

$$\Delta x^{th} = 1.22\ \frac{\lambda_0}{2NA} = 1.22\ \frac{\lambda_0 f}{2D} \qquad (23)$$

D… diameter of the collimated beam, λ_0 … central wavelength, f…focal length of the sample lens.

Inserting D_A and D_B yields theoretical transversal resolutions of $\Delta \boldsymbol{x_A}^{\boldsymbol{th}} = \mathbf{4.78\ \mu m}$ and $\Delta \boldsymbol{x_B}^{\boldsymbol{th}} = \mathbf{37.5\ \mu m}$.

Measured values according to a beam profiling camera are $\Delta \boldsymbol{x_A}^{\boldsymbol{m}} = \mathbf{16.5\mu m}$ and $\Delta \boldsymbol{x_B}^{\boldsymbol{m}} = \mathbf{50\ \mu m}$.

Measurements of a resolution test target (RTT) yield that structures of $\Delta \boldsymbol{x_A}^{\boldsymbol{mRTT}} = \mathbf{6.96\ \mu m}$ and $\Delta \boldsymbol{x_B}^{\boldsymbol{mRTT}} = \mathbf{24.8\ \mu m}$ are still resolvable with channel A and B.

Focal spot ratio (FSR)

As mentioned in chapter B.2.2.1, the FSR is the ratio of the focal spot diameters, respectively transverse resolutions.

The FSR is determined with the values obtained from the RTT.

$$FSR_{sys} = \frac{\Delta \boldsymbol{x_B}^{\boldsymbol{mRTT}}}{\Delta \boldsymbol{x_A}^{\boldsymbol{mRTT}}} = \frac{24.8}{6.96} = 1{:}\,0.28 = 3.57{:}\,1$$

Depth of focus (DOF)

The depth of focus describes the length of the depth range around the focal distance where the focal spot diameter is only increased by a factor of $\sqrt{2}$. The meaning of this value is that imaging within this range can be regarded as sharp.

$$DOF = \frac{4\,\lambda_0}{\pi NA^2} = \frac{4\,\lambda_0 f^2}{\pi D^2} = \frac{4 * 1045 * 10^{-9} * (50 * 10^{-3})^2}{\pi D^2} \quad (24)$$

D… diameter of the collimated beam, λ_0 … central wavelength, f…focal length of the sample lens.

$DOF_A = \mathbf{0.11mm}$, $DOF_B = \mathbf{4.30mm}$

Sensitivity

The theoretical (shot noise limited) sensitivity of the OCT system is calculated from the sample arm reflected intensities SR_S by the following formula [24]:

$$SNR^{th} = \frac{\varrho SR_S \Delta t}{2e} \quad (25)$$

With ϱ … quantum efficiency, SR_S…reflected intensity of one channel of the sample arm (measured with a power meter), Δt…sweep time, e…elementary charge.

${SNR_A}^{th} = \mathbf{83.38dB}$, ${SNR_B}^{th} = \mathbf{86.62dB}$

The measured sensitivity is calculated from the signal to nose ratio of the OCT signal that is obtained from a mirror placed in the sample arm:

$SNR_A = \frac{I_A}{\sigma_A} = \mathbf{74.6\ dB}$, $SNR_B = \frac{I_B}{\sigma_B} = \mathbf{78.0\ dB}$

Dynamic Range

The dynamic range describes the digital voltage interval, on which the analog signal is mapped. A 12bit data acquisition card provides 2^12 voltage values, which means that the smallest resolvable increment is $\frac{1}{4096}$ of the maximum amplitude value measured.

A 12bit Data card results in a theoretical dynamic range of **72.25dB**. This is lower than the measured sensitivity (see above). Therefore, the light was attenuated by neutral density filters in the sample arm for the sensitivity measurements in order to reduce the signal to noise ratio of the OCT signal. This attenuation was considered in the sensitivity measurements.

2) Data evaluation

Here, the electrical data acquisition and potential errors in the evaluated data will be discussed.

2.1 SS-OCT Signal acquisition

The basic scheme of the data evaluation is depicted in Fig. 29.

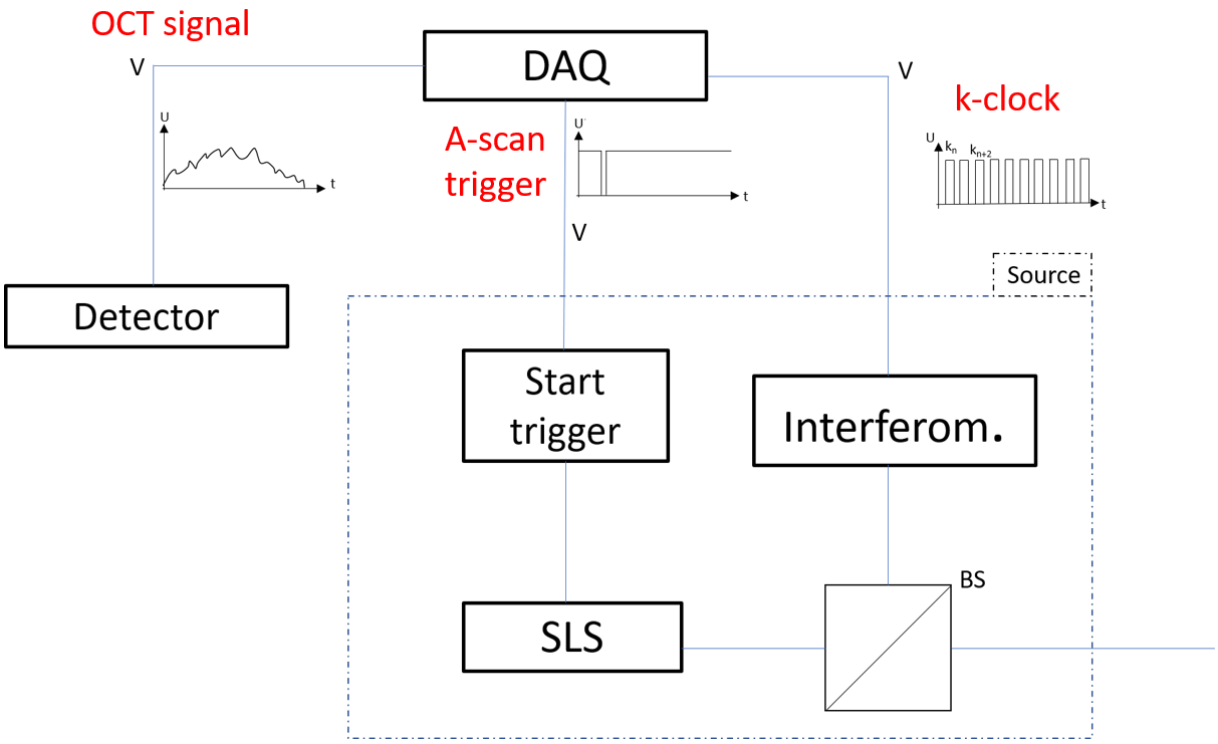

Figure 29: Basic scheme of data acquisition: SLS…Swept Laser Source, BS…Beam Splitter, DAQ…data acquisition card

Three input signals are sent to the data acquisition card (DAQ):

a) The k-clock signal:

Part of the light emitted by the swept light source (SLS) is coupled out by a beam splitter and is analyzed by an internal interferometer (included in the casing of the light source). Thereby, the zero crossings of the interferometric signal during a wavelength sweep are detected and transformed into a TTL signal, where each signal refers to a specific wavenumber (k) and the spacing between the wavenumbers is constant throughout the entire sweep. This signal is nonstop sent to the data card and accounts for a non-linearity in the k-sweep. Thus, the sampling of the data acquisition is not equidistant in time but in wavenumber k.

b) The A-scan start trigger:

This TTL signal is a step function that turns to 0V at the start of each k-sweep and shortly after returns to 1.2V. This signal serves as a marker in order to assign which of

the steps of the k-clock signal reflects the first k-vector of the sweep and corresponds to the starting point of an OCT A-scan.

c) The signal from the detector:

The optical signal is transferred to an electrical (voltage) signal by the detector with a signal bandwidth of 300MHz. This electrical signal is converted to a digital signal by the data acquisition card with a resolution of 12 bit. The detector frequency has to correlate with the frequency of the interferometric signal in order to fulfill the Nyquist theorem.

Every signal has a different path length to the data acquisition card and thus different delay times, which needs to be considered.

An 1D array of voltage values is recorded over time where, due to the k-clock signal, the measured values are equally spaced in k-space. The data is Fourier transformed as mentioned in chapter B, in order to generate the phase and amplitude depth profile of each transversal data point (x,y).

2.2 Noise sources and methods of compensation

Noise can be caused by vibrations in the system, irregularities in the electric signals or theoretical sampling limitations. Their background and how they can be compensated will be discussed in the following subchapters.

2.2.1 Fluctuations of start trigger

The start trigger (A-scan trigger) provided by the light source is subject to fluctuations that result in a shift of the whole k-spectrum (by one to three pixels) between A-scans. This results in fluctuations of the measured phase and has to be corrected, for example by the use of a fiber Bragg grating. A fiber Bragg grating (FBG) reflects a certain narrowband wavelength region (wavenumber k) and enables detection of this specific wavelength in the recorded spectrum of an A-scan. The FBG is integrated in one arm of the balanced detection in order to allow non-balancing at the specific wavelength (that is reflected by the FBG). A recorded, representative spectrum of one A-scan is shown in Fig. 30. The data is recorded in unsigned 16bit which results in an offset of the zero voltage measurement of 32768 a.u.

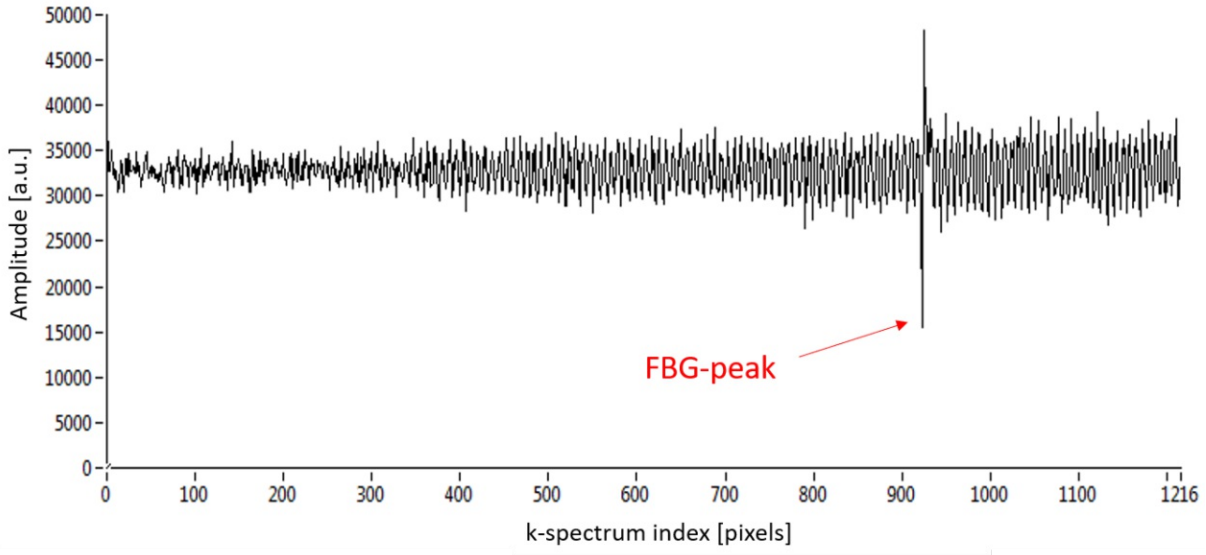

Figure 30: k-spectrum of a representative A-scan. The wavenumber k is represented by its index in the k-sweep. The FBG produces an additional signal in the spectrum (see red arrow) that can be used as wavelength marker of the spectrum. The minimum of the entire spectrum is detected and used to correct for fluctuations of the A-scan trigger.

Fig. 31a shows a comparison of all recorded A-scan spectra inside one B-scan. The minimum of the signal introduced by the FBG (corresponding to a specific k-position) does not remain at the same position for the A-scans (see enlarged Fig. 31b).

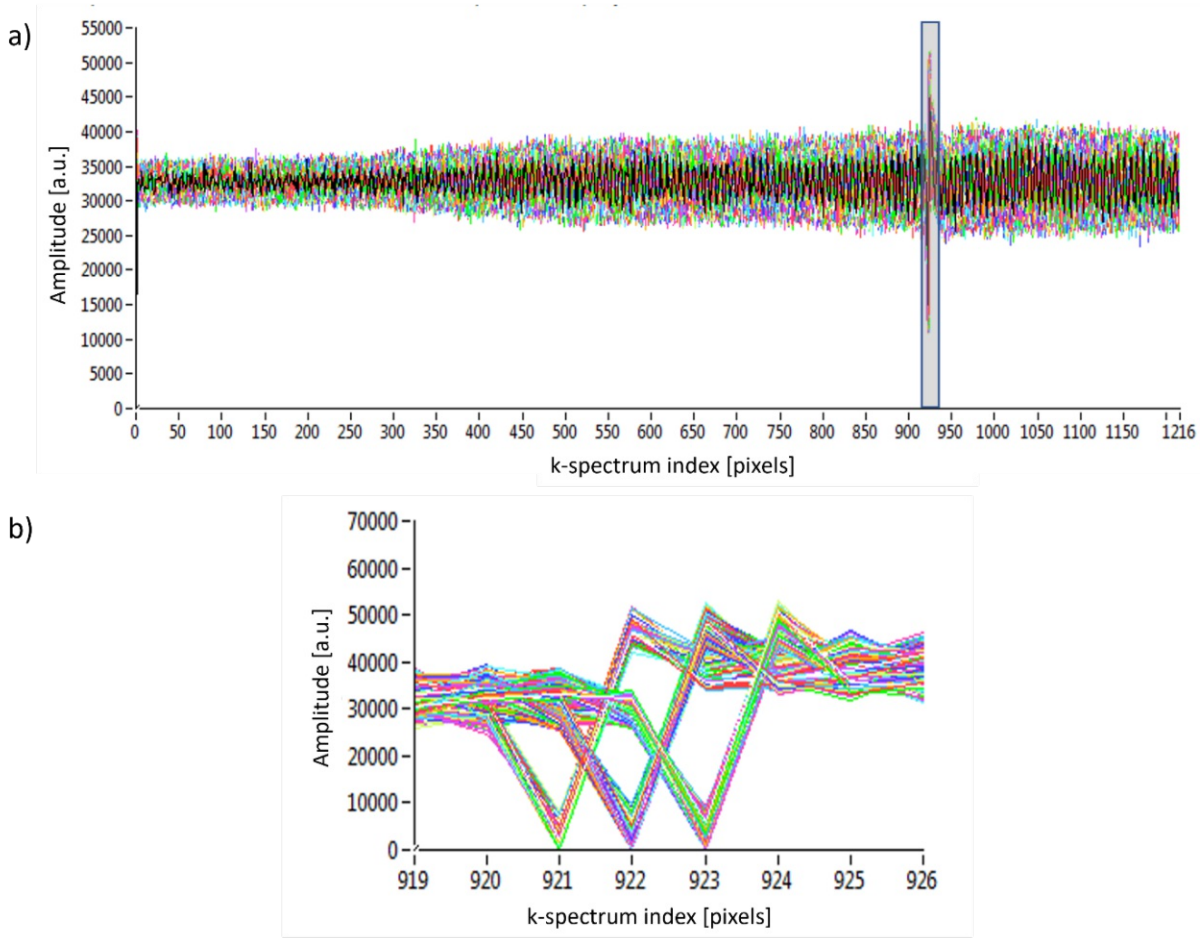

Figure 31: k-spectra of 512 A-scans contained in one B-scan. a) Entire A-scans that are depicted with different colors. b) Enlarged region around the peak of a). A clear shift along the abscissa between the A-scans can be observed in the enlarged plot.

The fluctuation in the A-scan trigger (k-shift) affects the polarization channels CHA and CHB differently because their path lengths in the Mach-Zehnder set-up are not exactly equal. Thus, CHA and CHB deliver different zero-delay positions leading to different distances from the zero-delay to the sample. The path length difference is such that it results in different frequencies in the k-spectra of the channels. Consequently, the higher frequency will face a higher phase shift by the k-shift as a lower frequency and the error is not cancelled out by phase-subtraction.

An algorithm was implemented in post processing, that detects the minimum in each A-scan and shifts each spectrum in such a way that the minima of all A-scans are matched. The corrected A-scan spectra of one B-scan are shown in Fig. 32.

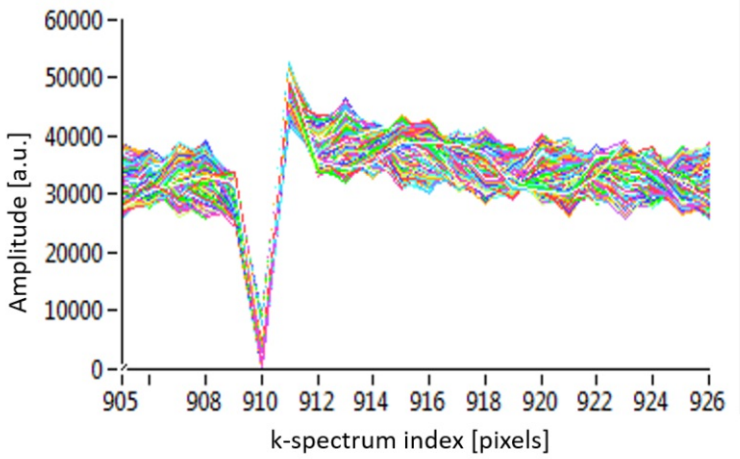

Figure 32: Enlarged region of A-scan spectra within a B-scan after applying the correction algorithm.

2.2.2 Cross coupling

The signals of Channel A and B are principally separated by their polarization states, but a residual amount of light is coupling into the other channel.

This can be detected using a mirror as a sample. The cross coupling CHA can be determined by blocking only the beam path of CHA in the sample arm (CHB is not blocked) and by monitoring the OCT signal retrieved from channel A. Without cross coupling no signal from the mirror should be observed, otherwise a residual amount of light of CHB reaches the detectors of CHA.

The cross coupling mainly originates from the fiber based components.

The cross coupling has to be minimized by aligning the polarization control paddles PC3 and PC4 in the detection arm. This is done by blocking CHA and CHB and minimizing the cross coupled OCT signal from the mirror.

2.2.3 Auto interference

As described in chapter B1 auto interference describes interference between light backscattered from different depths. As these interference signals are not phase shifted at the balanced detection unit (in contrast to the cross interference term arising from interference between sample arm and reference arm), these signals are eliminated by the balancing.

2.2.4 Aliasing

If the distance between sample and zero delay exceeds the depth range of the OCT system, the corresponding modulation frequencies in the k-spectrum become too high to be sampled by the detector. These high frequencies are thus under sampled and generate aliasing artefacts.

This means that high frequencies are mapped into a lower frequency band (that is detectable by the detector) and distanced structures appear erroneously closer to the zero delay.
To remedy for those artefacts, the frequency range of the detector is limited by 350 MHz which attenuates higher frequencies and thereby works as a low-pass filter.

2.2.5 Imperfect balanced detection

The following descriptions refer to observations of only one polarization channel (but the conclusions can be transferred to the other channel as well) when the sample arm is blocked (no interference signal, just light returning from the reference arm impinges on the detector).
Imperfect balancing (due to imperfections in the fiber optics) of the two input channels at the detector leads to saturation of the AD-converter of the data acquisition board. As the signal subtraction of the arms does not work perfectly, a remaining low frequency component ("DC term") appears over the recorded spectrum. In order to compensate for this artefact, an electronic high-pass filter needs to be implemented between detector and data acquisition Board that filters out this low frequency component and prevents a saturation of the AD-converter. This low frequency component represents z-positions, close to the zero path length delay. Thus, the available depth range is slightly reduced (by ~50μm).

2.2.6 Dispersion

The refractive index and thus the travel speeds of the light in material differs for the different wavelengths, an effect known as dispersion. In the current setup this is mainly introduced by the fibers and the fiber-based components. As a result of the dispersion, the interferometric signal, although recorded in k-space, shows a chirp of the modulation frequency. This causes a broadening of the axial point spread function and needs to be compensated. The dispersion effect is compensated in post-processing by an algorithm introduced by Wojtkowski et al. [25].
Thereby, a different phase-shift for each wavelength (k-pixel) is introduced to the interferometric signal. For correcting the second order dispersion (zero and first order dispersion do not broaden the axial point spread function) the phase-shift has a quadratic dependency of the k-pixel, higher orders of dispersion can be compensated accordingly. For the used system, compensating second order dispersion was sufficient in order to generate a sharp peak after Fourier transformation of the spectral data.

2.2.7 Mismatch of the path lengths in the sample arm

The light in the sample arm is split into two beams that do not travel the exact same distance in the two beam paths of the Mach Zehnder Interferometer. This results in a different modulation frequency in the two spectra for a specific sample depth. To correct for this, a linear phase term is added to one of the channels which corresponds to a change of first order dispersion and thus to a linear shift in z-direction of the corresponding axial point spread function. The used value for this correction is manually set by monitoring the depth position of a mirror in the sample arm for both channels while changing the parameter for the first order dispersion correction.

3) Adjustment of the pivot point position of the x-scanner

As outlined in chapter C1.3 the position of the x-scanner needs to be aligned in such a way that the beams exactly impinge on the pivot point of the scanner. In order to check that this condition is fulfilled, the phase difference between adjacent A-scans at a certain k-position is taken as a measure.

A misaligned pivot point in respect to the imaging beam goes hand in hand with an increasing or decreasing phase when lateral positions are compared. This is illustrated in Fig. 33, where the interferometric signal and phase at k-pixel position 30 (red line) is shown for adjacent A-scans.

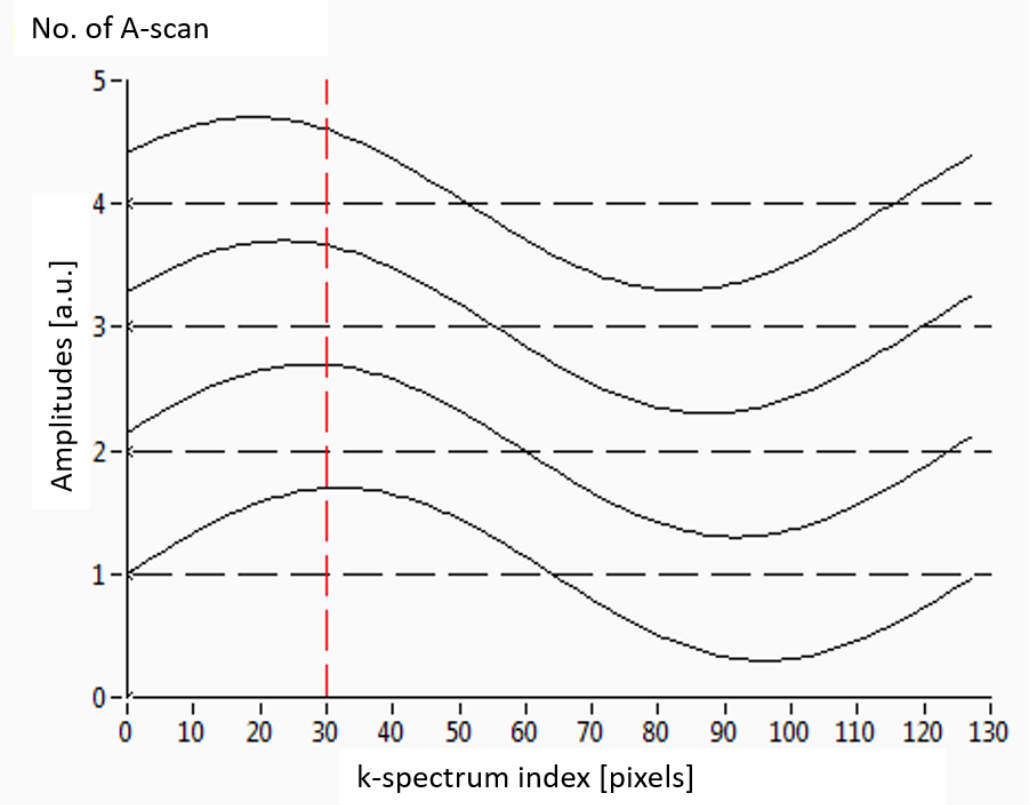

Figure 33: Illustration of a phase shift between adjacent A-scans introduced by misalignment of the pivot point of the scanner. The phase of adjacent A-scans inside a B-scan is changing with the scanner position. The interferometric signals are displaced in y-direction for better visibility.

The different phase values are equivalent to a modulation of the interferometric signal in lateral direction.

Fourier transformation of the interferometric signal of a B-scan in lateral direction (and not along the spectral direction for generating the B-scan) delivers a spectrum that corresponds to the spatial frequency of the recorded B-scan. The frequency components are symmetrically distributed around the zero frequency. The phase shift introduced by a pivot point misalignment shows a linear phase progression and the center of the spatial frequency spectrum will be shifted away from the zero frequency. A representative Fourier transformed

spectrum obtained by recording a B-scan with a misaligned pivot point is shown in Fig. 34 and shows two symmetrical distributions around zero spatial frequency. In case of a perfect pivot point position alignment, no additional modulation of the phase over lateral A-scan position occurs (cf. Fig. 35) and the spatial frequency spectrum shows a peak at the zero-frequency.

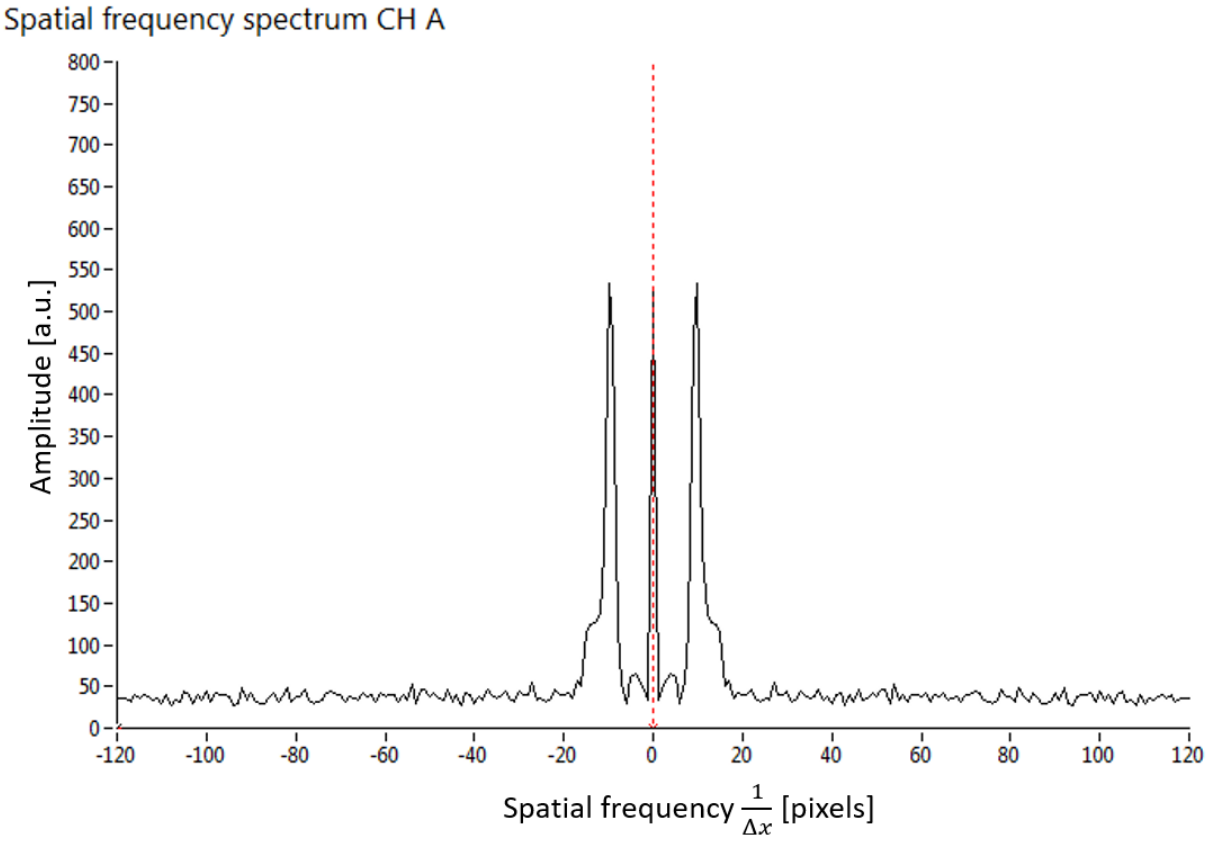

Figure 34: Spatial frequency spectrum obtained from a B-scan. The center of the frequency spectrum is shifted from the zero spatial frequency position and the spectrum is split into two components, indicating a misalignment of the pivot point position of the scanner in respect to the imaging beam.

The Fourier transformation always creates a positive and negative frequency spectrum. With improvement of the alignment the two peaks move to the zero position, which means no lateral phase modulation occurs.

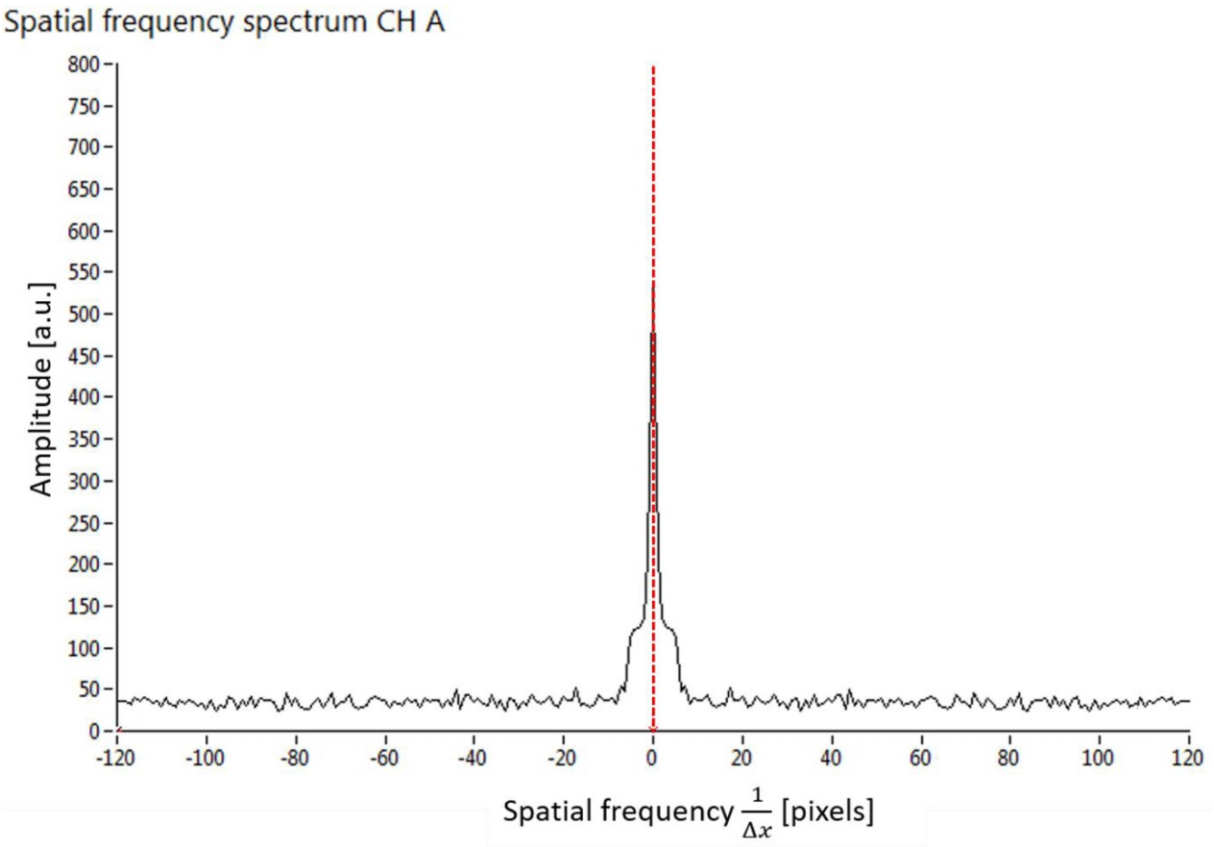

Figure 35: Spatial frequency spectrum obtained from a B-scan. The center of the frequency spectrum is located at the zero spatial frequency position, indicating a correct alignment of the pivot point position of the scanner in respect to the imaging beam.

D. RESULTS

In order to determine the system´s stability, measurements with a mirror were performed. In a next step the transversal resolution was determined experimentally using a resolution test target (RTT). In the final step, the system was used to measure *three calibrated sample*s of defined step sizes (50, 100, 200 nm).

The test samples were manufactured at the Vienna University of Technology (Institute of Solid State Physics) by applying a chromium coating on a glass plate. In contrast to the RTT where only the test structures are coated with chromium while the surroundings are uncoated, these samples are entirely coated in order to eliminate any additional phase changes (introduced for example by reflection at different kind of surfaces). At first a primary coating is evaporated onto the glass plate so that the glass is completely covered by the material. Then an additional glass sample is placed on the primary coated glass plate and a layer of defined height is applied. After removing the glass sample, a deepening of defined depth is created. Fig. 36 shows the manufactured sample schematically.

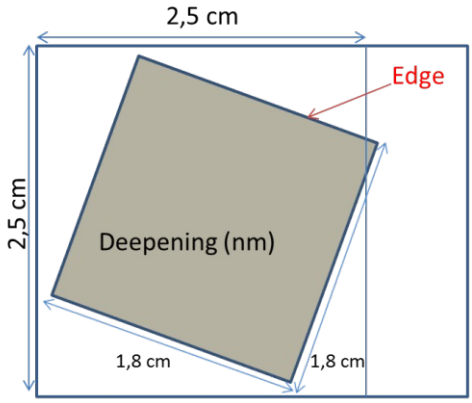

Figure 36: Schematic drawing of the test sample with varying step depths. A different coating thickness is present in the center (thinner coating) and periphery (thicker coating) of the sample. The thickness difference can be arbitrarily set with a precision in the nanometer range.

The measurements are taken with a scanning pattern of 512 A-scans per B-scans and 500 B-scans. Because of post-processing reasons the last 5 B-scans are cut off.

As time dependencies of the signal will be examined, it is worth mentioning that A-scans (x-data points of the volume scan) are recorded at $100\ kHz$ and B-scans (horizontal line scans) with a frequency of $\frac{100\ kHz}{512+100} \approx 163\ Hz$. The added 100 A-scans in the denominator result from the time the x-scanner needs to set back to the initial position before the next line scan is started.

The amplitude and phase depth profiles will be evaluated at a specific depth position Δz, where an amplitude maximum of a preset reference point x_0,y_0 occurs in Channel A. Thereby an amplitude and phase en-face image are generated at a certain depth Δz.

1) Stability measurements

In order test the phase stability of the system, the temporal evolution of the phase has to investigated, starting with the simplest sample, which is a *mirror*.

1.1. M-scans

In a first step, M-scans, that are depth scans repeated at the same transversal position (no x- and y-scanning), are recorded. The acquisition runs non-triggered, which means that 512·495 A-scans are recorded sequentially at the A-scan rate of 100 kHz.

These repetitive measurements contain information about fast fluctuations onto the phase that occur independently of the galvanometer scanner. In addition, M-scans allow comparison of the phase stability in dependence of the activation of the galvanometer scanner, as the scanners maintain the position by servo control even if no scanning voltage is applied.

The recorded spectral data is converted to A-scans and the pixel along the z-direction with maximum intensity (corresponding to the mirror position) is used for phase evaluation.

The 1D array of these phase pixels is mapped onto a 2D image, by cutting it into portions of 512 pixels and arranging them in parallel vertical lines. Consequently, the vertical axis represents the fast axis with 10µs time between the pixels (100 kHz A-scan rate). The horizontal axis represents the slow axis with ~5ms delay between the pixels (scan rate of $\frac{100\ kHz}{512} \approx 195 Hz$).

At first, the advantage of the differential phase technique is investigated by comparing the absolute phase images.

Figs. 37 and 38 show the images of the absolute phase signals of both channels and the phase-difference, retrieved from an M-scan recorded with no voltage applied onto the galvanometer scanner. A slow fluctuation can be observed, that oscillates with 300 Hz. The improvement on phase stability can be recognized in the different color scales, as the amplitude of the phase fluctuation strongly decreases.

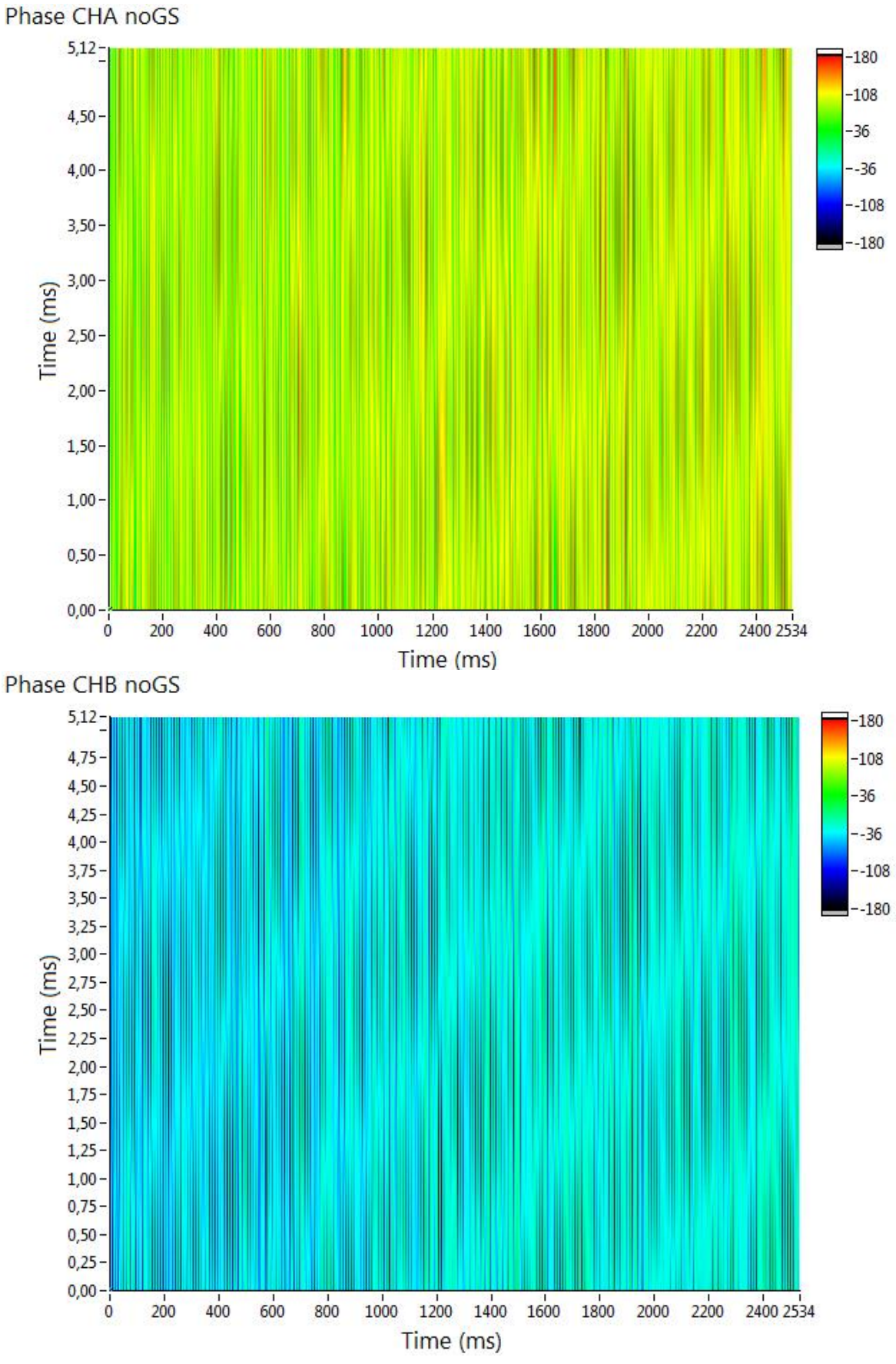

Figure 37: M-scans of the phase at the maximum intensity of an A-scan recorded with no voltage applied to the galvanometer scanner. The absolute phase in the channels fluctuates around a constant value with a frequency of 300 Hz. The color bar indicates the measured phase in degrees.

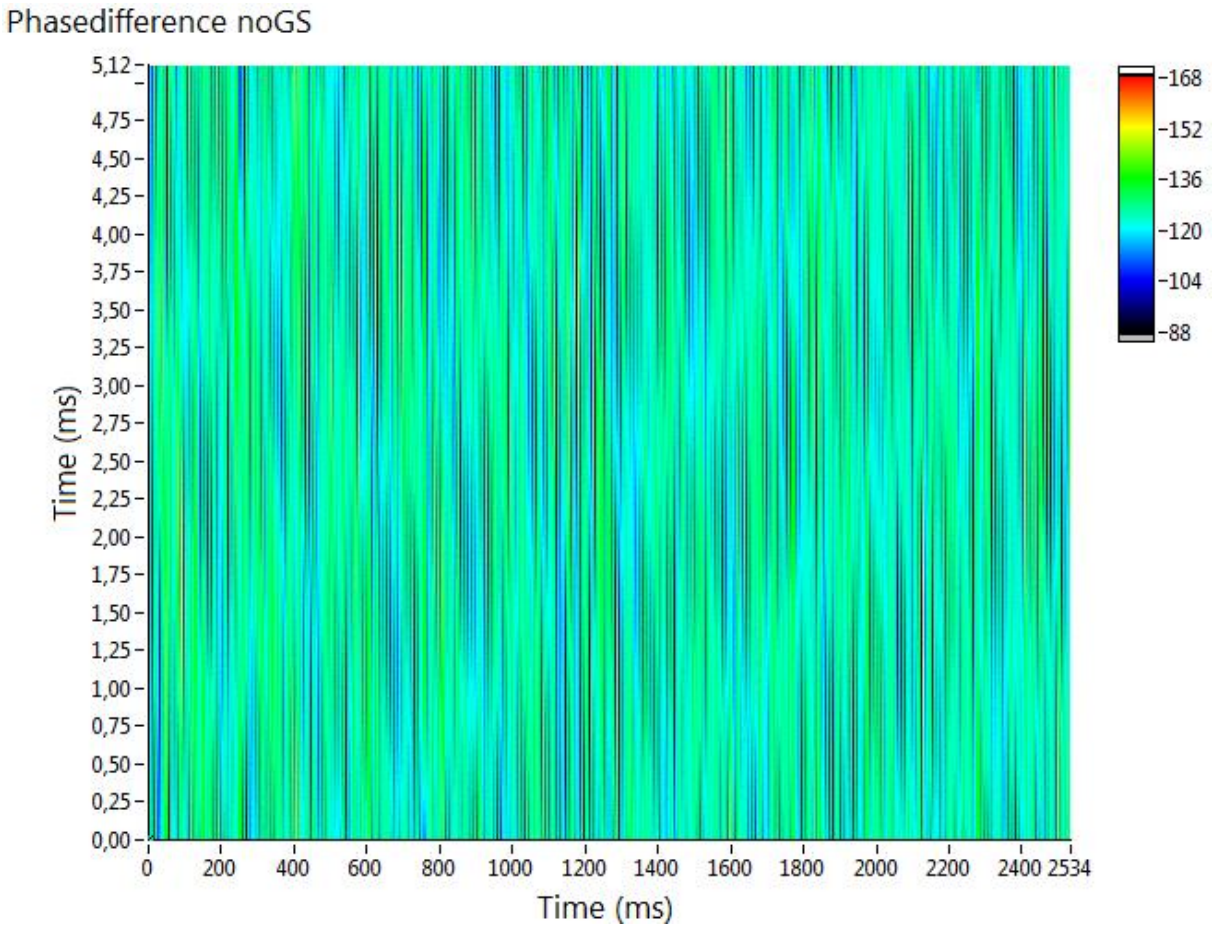

Figure 38: M-scan of the measured phase difference between the two channels. Although a similar behavior as in Fig. 37 can be observed (fluctuations with 300 Hz), the phase subtraction decreases the amplitude of this fluctuation. Color scale: Phase difference in degrees

The measured phase noise is calculated by the standard deviation of the phase difference values recorded:

$$\varrho_{Ph}^{m} = \sigma(\Delta\varphi) = \sqrt{\frac{\sum_{i=1}^{N}(\Delta\varphi_i - \overline{\Delta\varphi})^2}{N-1}} \tag{26}$$

The theoretical phase noise is calculated by Gaussian error propagation of the phase noise of the single channels.

$$\varrho_{Ph}^{th} = \sqrt{\left(\varrho_{Ph}^{th\,A}\right)^2 + \left(\varrho_{Ph}^{th\,B}\right)^2} = \sqrt{\frac{1}{SNR_A} + \frac{1}{SNR_B}} = \sqrt{\frac{\sigma_A}{\overline{I_A}} + \frac{\sigma_B}{\overline{I_B}}} \tag{27}$$

The values calculated from M-scans without active galvanometer scanner is shown in Table 1.

Table 1: Comparison of theoretical and measured phase stability. The measured absolute phase values are far off the ideal theoretical values, while the subtracted phase shows a huge reduction of phase noise

	Channel A	Channel B	Phase-difference
Phase noise measured	27.95°	30.5°	8.8°
Phase noise theoretically	5.22°	4.6°	6.96°

The activation of the galvanometer scanner has a huge impact onto the absolute phase values of both channels, while the phase difference between the channels remains the same, which can be seen in Figs. 39 and 40.

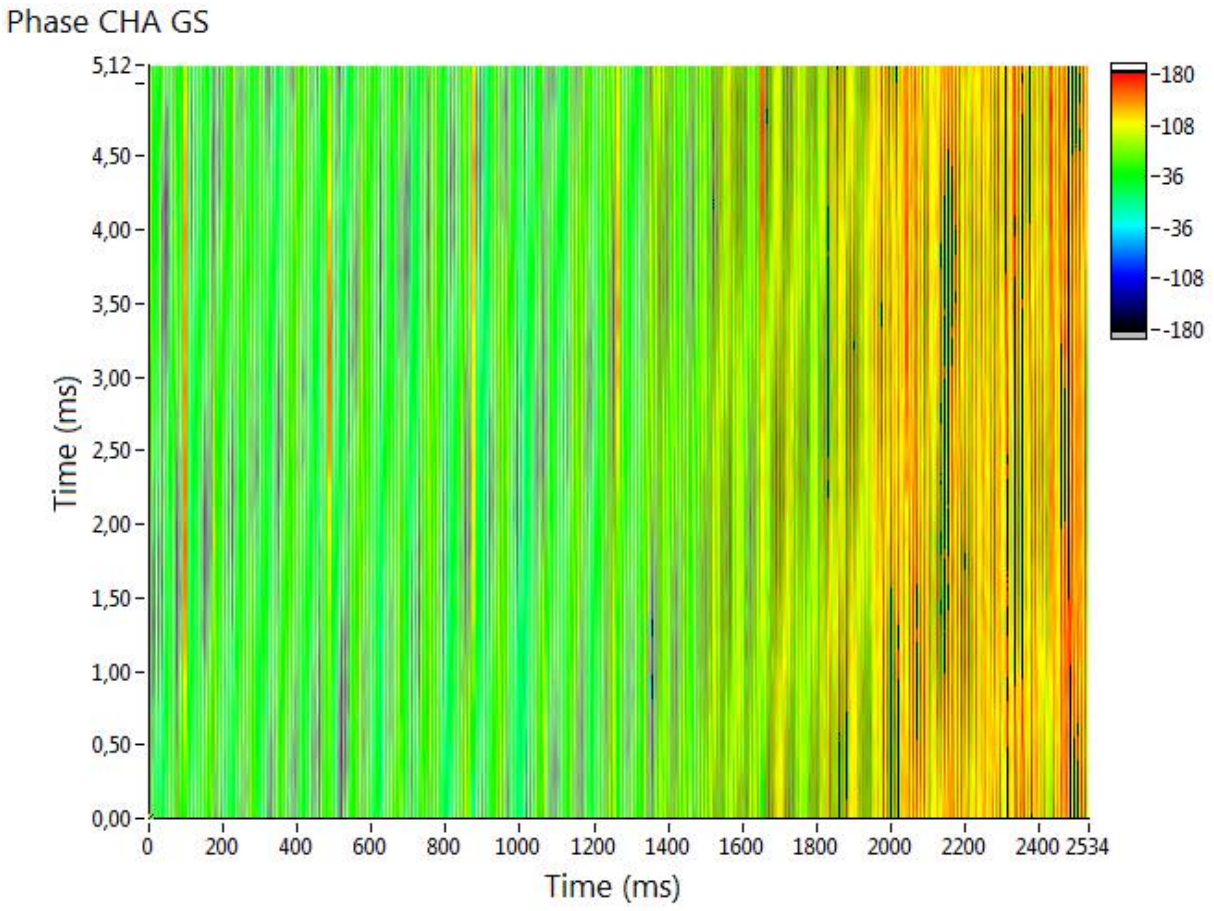

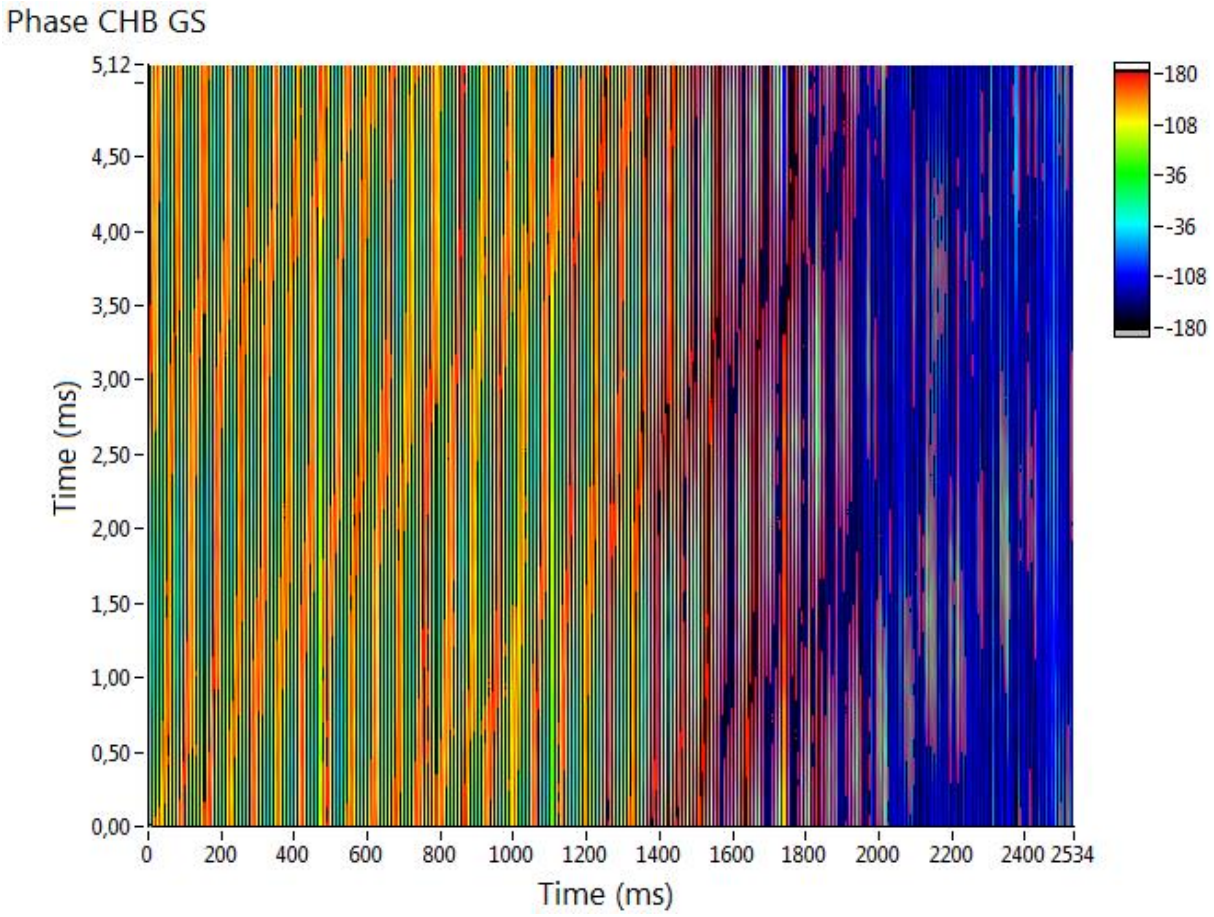

Figure 39: Absolute phase values of an M-scan with the galvanometer scanner turned on. A strong drift can be observed additionally to the fluctuation with 300 Hz. Color scale: Phase difference in degrees

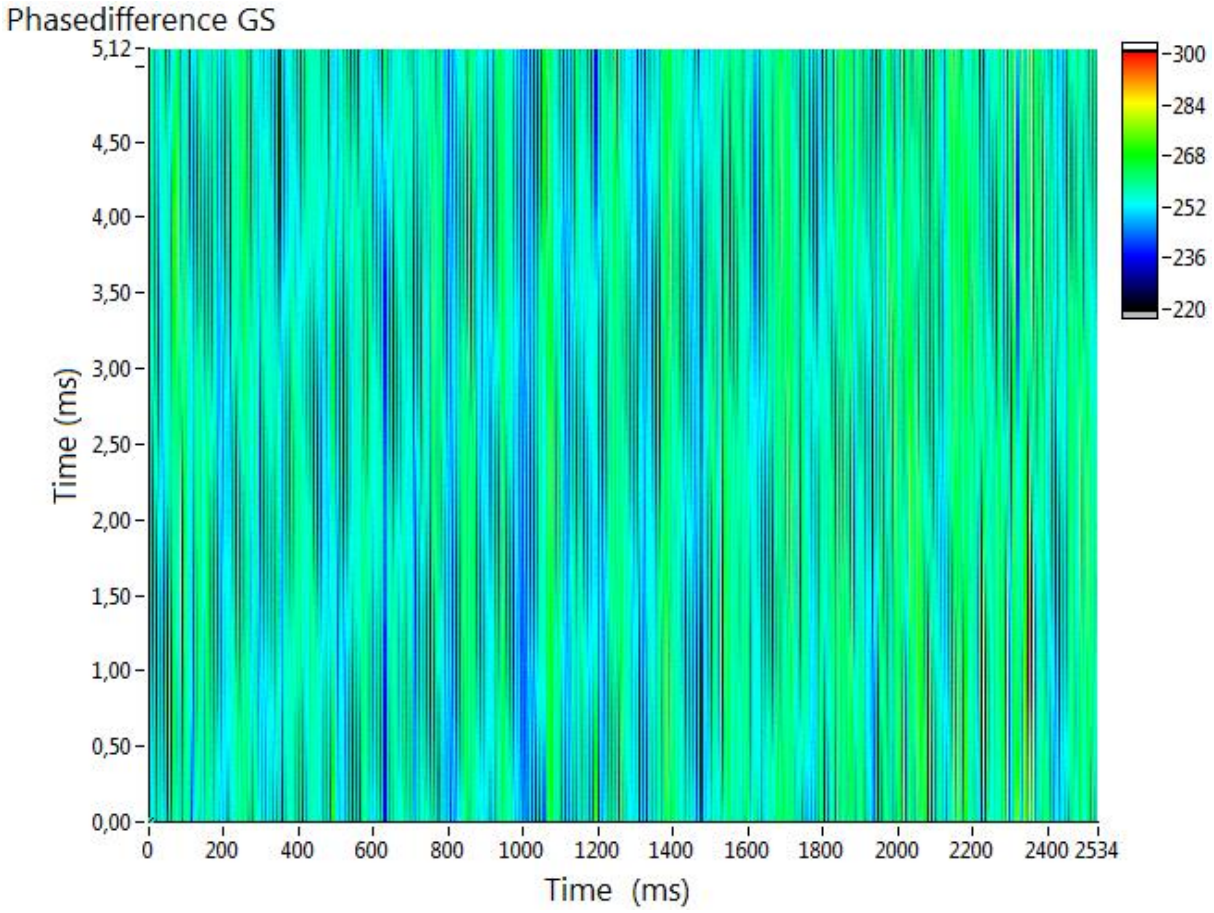

Figure 40: Phase difference values between the channels of an M-scan with the galvanometer scanner turned on. The impact of the galvanometer scanner onto the phase difference between the channels is negligible. Color scale: Phase difference in degrees

The evaluation of the phase-stability of M-scans with activated galvanometer scanner is summarized in Table 2.

Table 2: Comparison of theoretical and measured phase stability. The measured absolute phase values increased heavily when the galvanometer scanner is turned on, while the noise in the phase difference signal increased only slightly

	Channel A	Channel B	Phase-difference
Phase noise measured	66.27°	61.03°	9.31°
Phase noise theoretically	5.2°	4.3°	6.75°

A closer look into the phase progression of the M-scan is shown in Fig. 41. The scanners introduce a high frequency of 2 kHz additionally to the 300 Hz on the measured absolute phase values as well as a linear drift in the phase values. Both observations indicate a residual pivot point misalignment. In a perfectly aligned system, a vibrating x-scanner mirror would not affect the measured phase values, because the path length remains the same and is independent from the rotating angle of the scanner. In case of a misalignment, the vibration (small rotation around the set scanning angle due to the servo control) of the mirror introduces slightly different path lengths and thus cause phase fluctuations. In the difference of the absolute phase signals of the two channels (shown in Fig. 41) the 2kHz frequency cannot be observed anymore (Fig. 42).

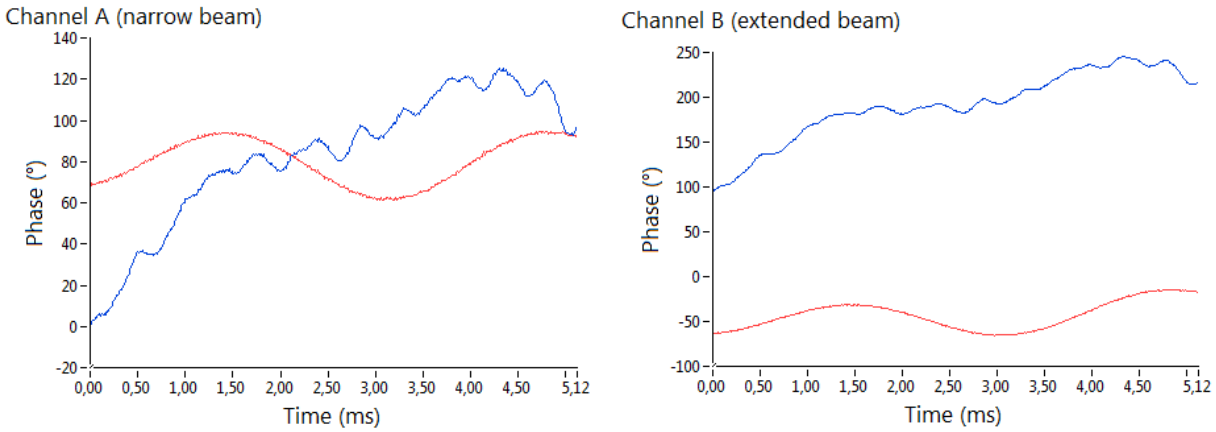

Figure 41: The phase progression with time in one channel of one vertical line (B-scan index 21) is plotted and the influence of the galvanometer scanner (GS) is shown. GS deactivated (red line), GS activated (blue line)

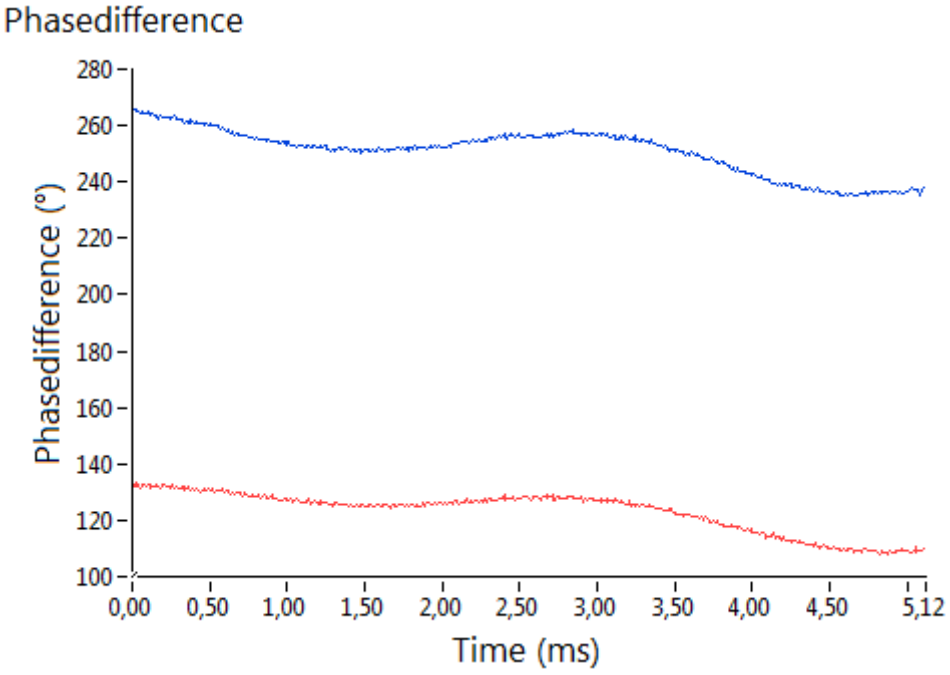

Figure 42: Comparison of the phase difference between the two channels alongside B-scan no. 21 with activated (blue line) and deactivated (red line) galvanometer scanners.

In order to examine the source of the fluctuations, a differentiation between interferometric jitter in the sample arm and fluctuations introduced by the fiber or electronic part of the system has to be done:

For this purpose, one beam is blocked and the other beam is coupled equally into the detectors of channel A and channel B by aligning PC3 and PC4 accordingly.

Thereby the subtraction of the phase measured in channel A and channel B results in cancelling out influences of the bulk optics setup and the remaining fluctuations can be traced back to the fibers or electronic components. The phase difference image obtained with this configuration is shown in Fig. 43.

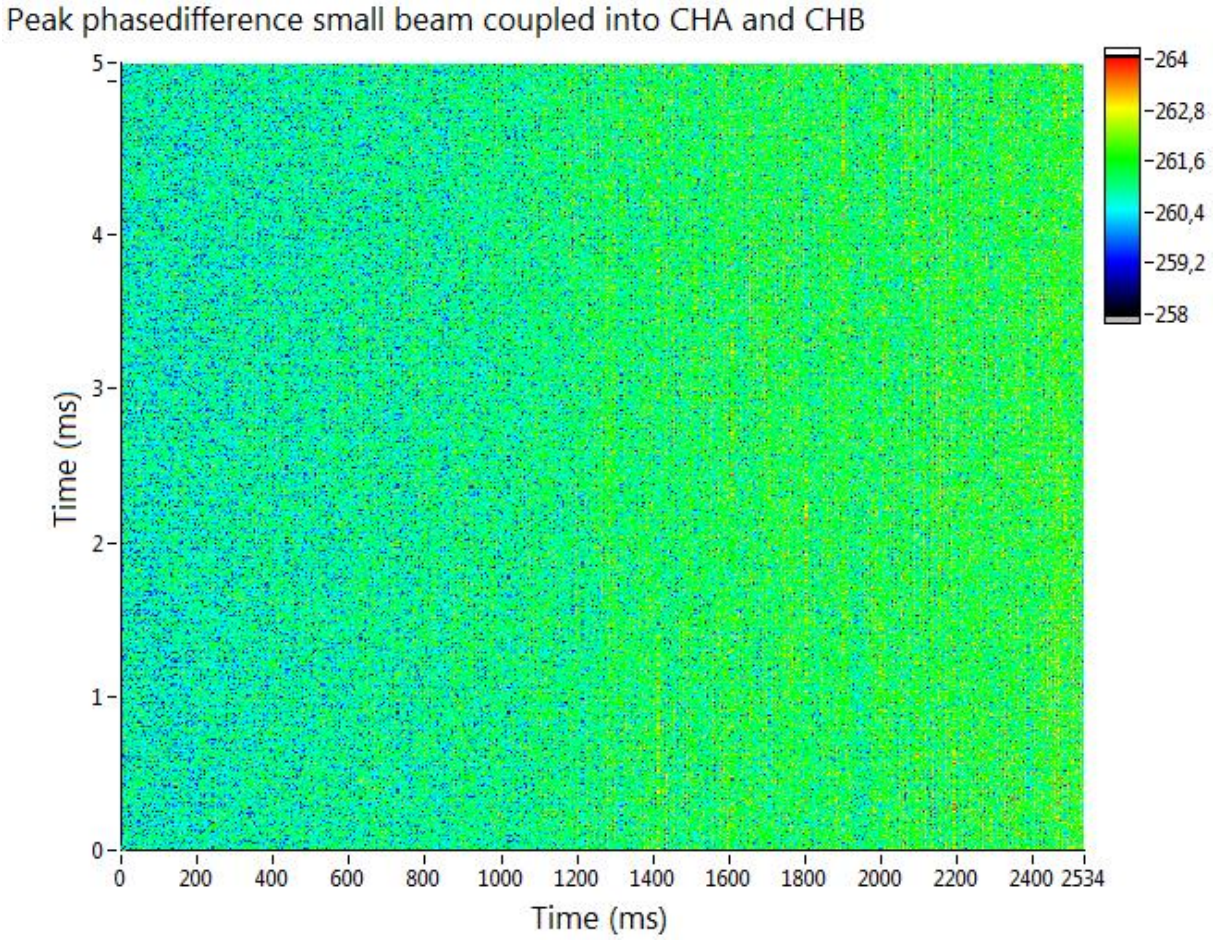

Figure 43: M-scan of the phase difference between the two channels when the beam with narrow focal spot diameter is coupled into CHA and CHB and the other beam is blocked. The phase-difference shows small fluctuations with 300 Hz that can be seen in the striped pattern. Color scale: Phase difference in degrees.

Although the phase noise is very low, the oscillation of 300Hz is not completely eliminated and has to come from the fiber based setup or electronic components.

1.2 BM-scans

A BM Scan is a line scan recorded repeatedly at the same y-scanner position. The BM-scans allow detection of the deviation from the optimum pivot point positioning of the scanner as mentioned in chapter C3 as well as investigation of the reproducibility of the lateral scanning pattern.

The phase within the B-scan is evaluated at the peak position of the mirror in the sample arm, which is the depth pixel position of highest intensity. Scanning along x-direction results in a certain lateral phase difference progression. Repeating the B-scan and arranging the recorded B-scans adjacent to each other ideally results in repeatable phase values between adjacent B-scans at the same lateral position.

In Fig. 44 the phase values at the axial peak position are plotted for each channel and shows strong fluctuations between adjacent B-scans. The stripe pattern results from phase wrapping (2π ambiguity) inside a linear phase progression in lateral direction. This linear phase progression might either result from a combination of a tilted mirror and a residual pivot point misalignment.

Adjacent B-scans are shifted to each other (cf. ripples of the horizontal bands in Fig. 44) which could be caused by the 2 kHz vibration of the scanners. The B-scan sample rate is 163 Hz which is not sufficient to determine this frequency.

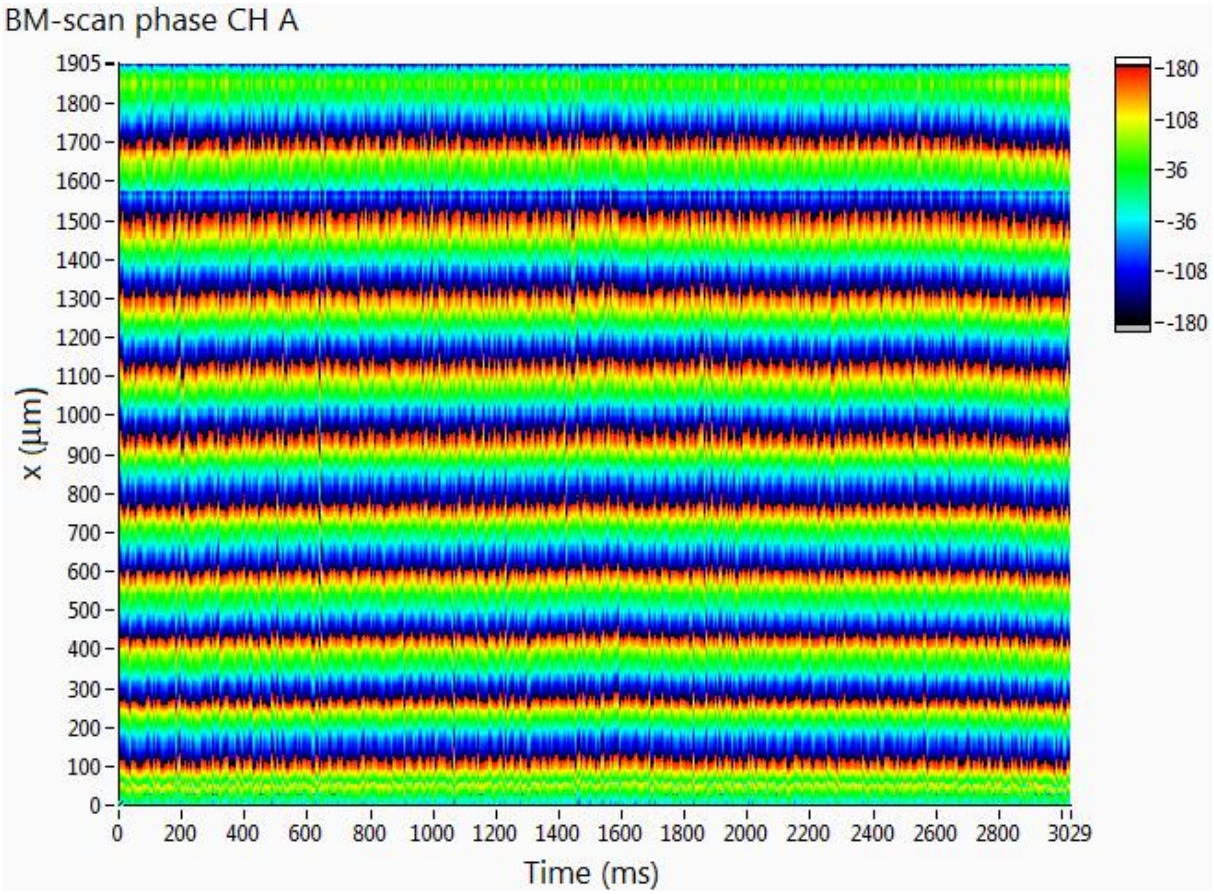

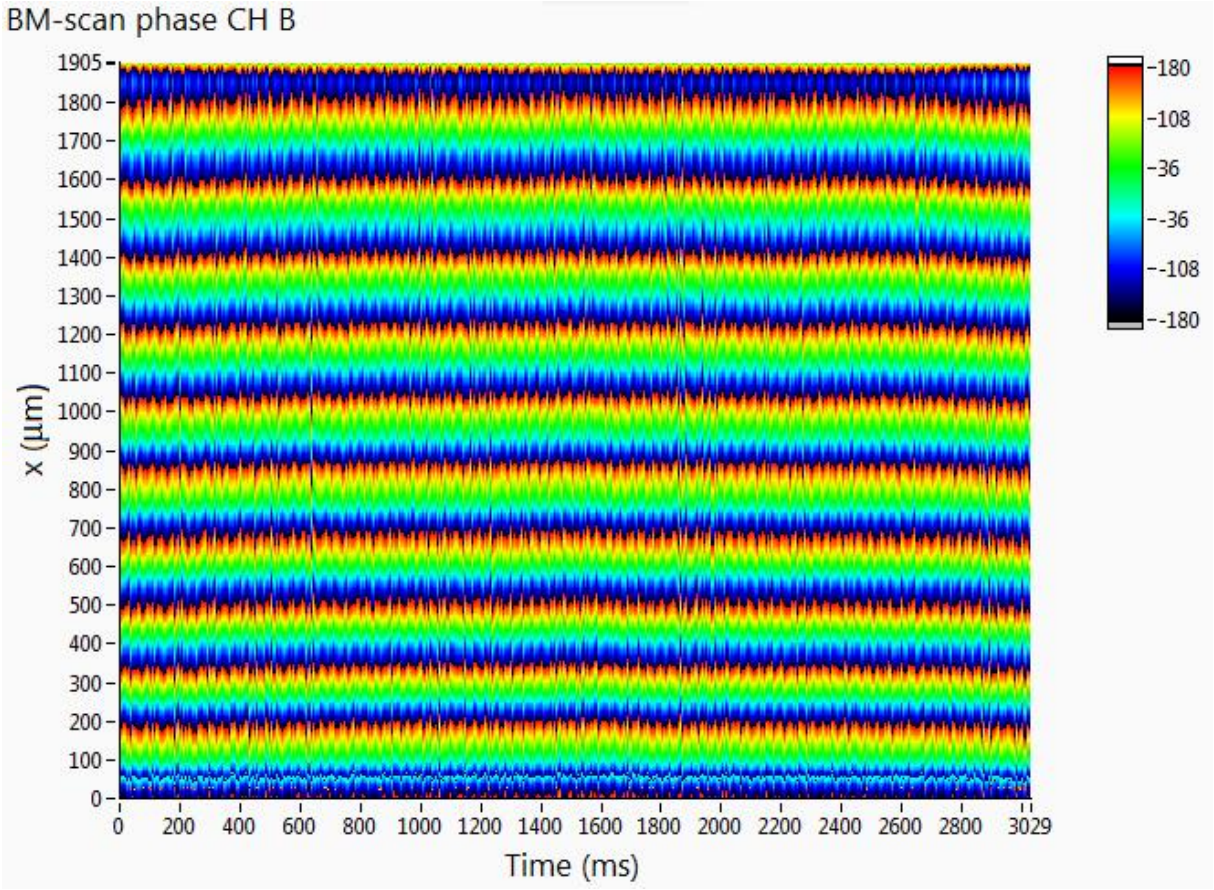

Figure 44: BM-scan of the phase retrieved at the maximum of the axial coherence function of a mirror. Strong phase fluctuations can be observed in both channels as well as a strong phase change along the x-direction. Color scale: Absolute phase values in degrees.

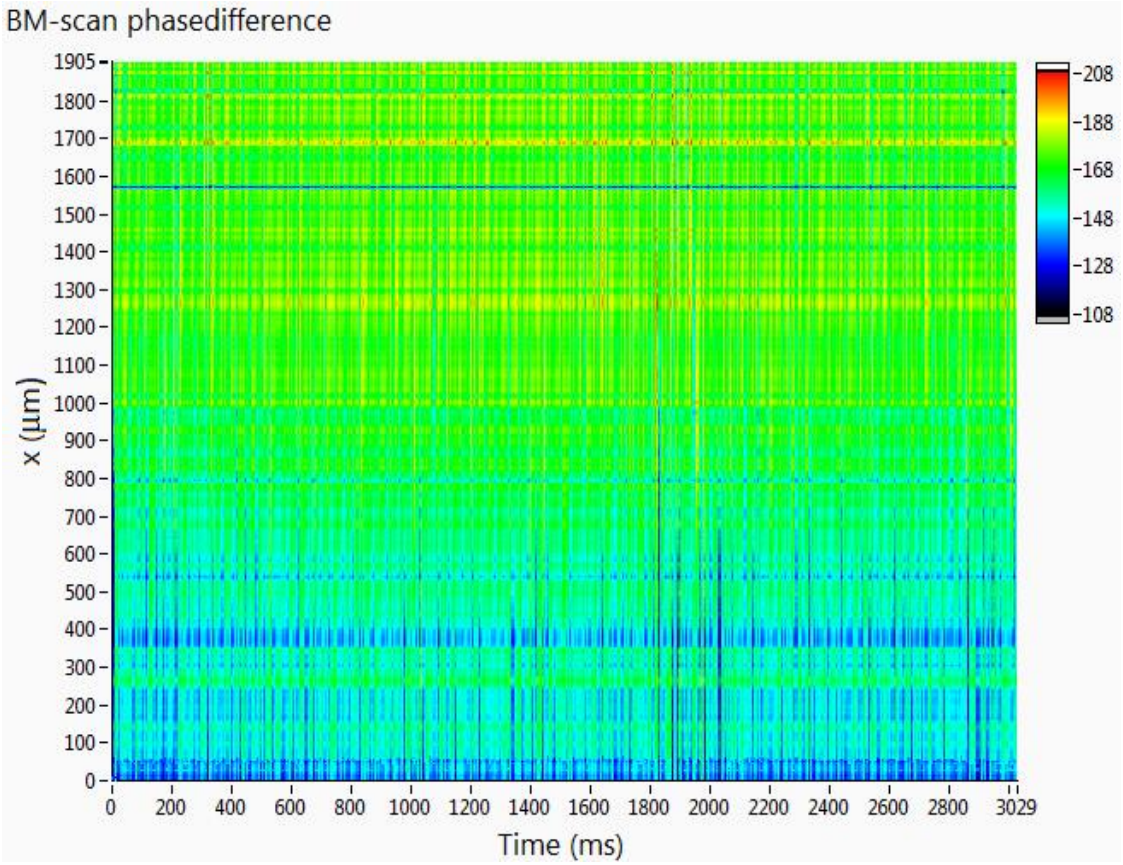

Figure 45: BM-scan of the phase difference between the two channels retrieved at the maximum of the axial coherence function of a mirror. The phase difference shows residual small fluctuations from B- to B scan and a greatly reduced phase change along x-direction. Please note the different scale of the phase values compared to Fig. 39. Color scale: Phase difference between the two channels in degrees.

The subtraction of the phase values recorded for each channel reduces phase noise evoked by the scanner irregularities as can be seen in the BM-scan measurements, visualized in Fig. 45. In addition, the phase shift along x-direction that is associated with a tilt of the mirror or a residual misalignment of the pivot point of the scanner is greatly reduced.

The reproducibility in terms of absolute phase and phase difference between the channels is analyzed by calculating the standard deviation of the phase values retrieved at the same A-scan position (lateral position) for repetitive B-scans. After calculating the standard deviation at each A-scan position, the mean value is calculated by averaging over the standard deviations. This procedure eliminates the influence of the strong phase shift with lateral position introduced to the absolute phase during scanning. The measured phase noise shows a strong influence of the scanner motion on the phase stability (Table 4). In comparison to the phase noise of M-scans, the theoretical stability of the phase difference is reduced, as the phase noise is increased, but the measured stability is increased. This shows the benefit of phase subtraction, as the noise introduced by scanners can be decreased.

Table 4: Comparison of theoretical and measured phase stability during scanning in x-direction. The noise in the measured absolute phase values increases when the galvanometer scanner is turned on, while the noise of the calculated phase difference remains close to the theoretical expected (see Eq. 20) value.

	Channel A	Channel B	Phase difference
Phase noise measured	15.33°	15.36°	7.07°
Phase noise theoretical	6.02°	4.18°	7.39°

2) Volumetric measurements

In order to quantify the geometric properties of the scanning field, a *resolution test target (RTT)* is placed in focal distance of the sample lens.

In a first step, the extension of the scanning field is measured. The scanner amplitudes for x-scanner and y-scanner are set to an arbitrary value of 2000 which theoretically results in a scanning field of 2000 x 2000 μm^2, when using a convex lens with a focal length of 50mm.

The recorded scanning pattern contains 500 B-scans, each consisting of 512 A-scans. However, the data evaluation software cuts off the first 5 B-scans.

The measurements with the RTT indicated a step width of 3.72µm in x-direction (=A-scan-direction) resulting in total lateral extension of 1904.76µm. The step width in y-direction (=B-scan direction) is measured to be 4.01µm and the vertical field expansion is 2056µm.

In a next step, an attempt is made to quantify the potential lateral displacement of the sample beams by comparing the position of landmarks (e.g. edges of the pattern) of the RTT in the amplitude images of both channels as shown in Fig. 46.

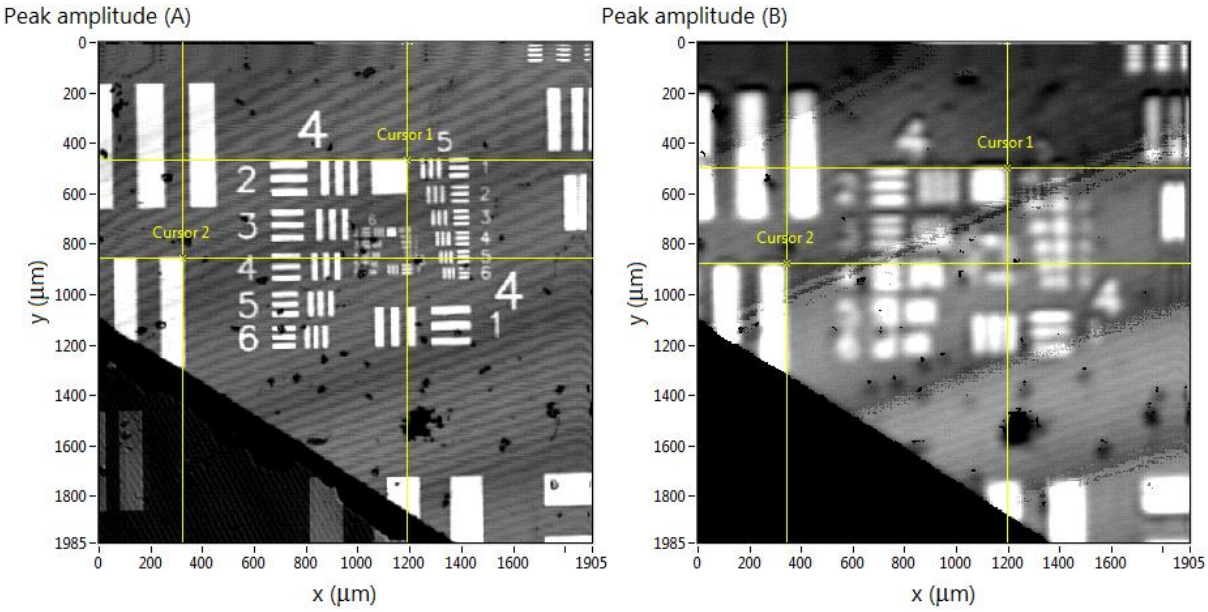

Figure 46: En-face amplitude images of channel A and B. Two significant landmarks (edges in the RTT pattern) are marked by Cursors. The coordinates of the cursors in both pictures deviate from each other that reflects a beam displacement.

A very precise evaluation is difficult because of the low transverse resolution of channel B. Channel B only resolves group 4 element 3 of the RTT indicating a transverse resolution of $\Delta x_B{}^{th} = 24.8\ \mu m$. A rough estimation, deduced from the amplitude images, indicates the displacement values presented in Tab. 5.

As the displacement lies within the transverse resolution of channel B, the "measured phase" values should be treated with caution. A stronger misalignment in vertical direction can be observed and the displacement changes within the field of view. A more precise assessment of the variation of the displacement between cursor 1 and 2 cannot be done, as the shift lies within the resolution limit of channel B.

Table 5: Measured lateral displacement between the two imaging beams obtained from amplitude images.

	Horizontal displacement (A left to B)	Vertical displacement (A above B)
Cursor 1	3.72 µm	36.09 µm
Cursor 2	11.16 µm	28.08 µm

The theoretical transverse resolution of the system is given by the transverse resolution of channel A. In order to detect that limit, the scanning field is reduced by a factor of 4. The amplitude image of channel A is shown in Fig. 47 and indicates that the last resolvable element is Group 6 Element 2, corresponding to a linewidth or transverse resolution of 6.96µm.

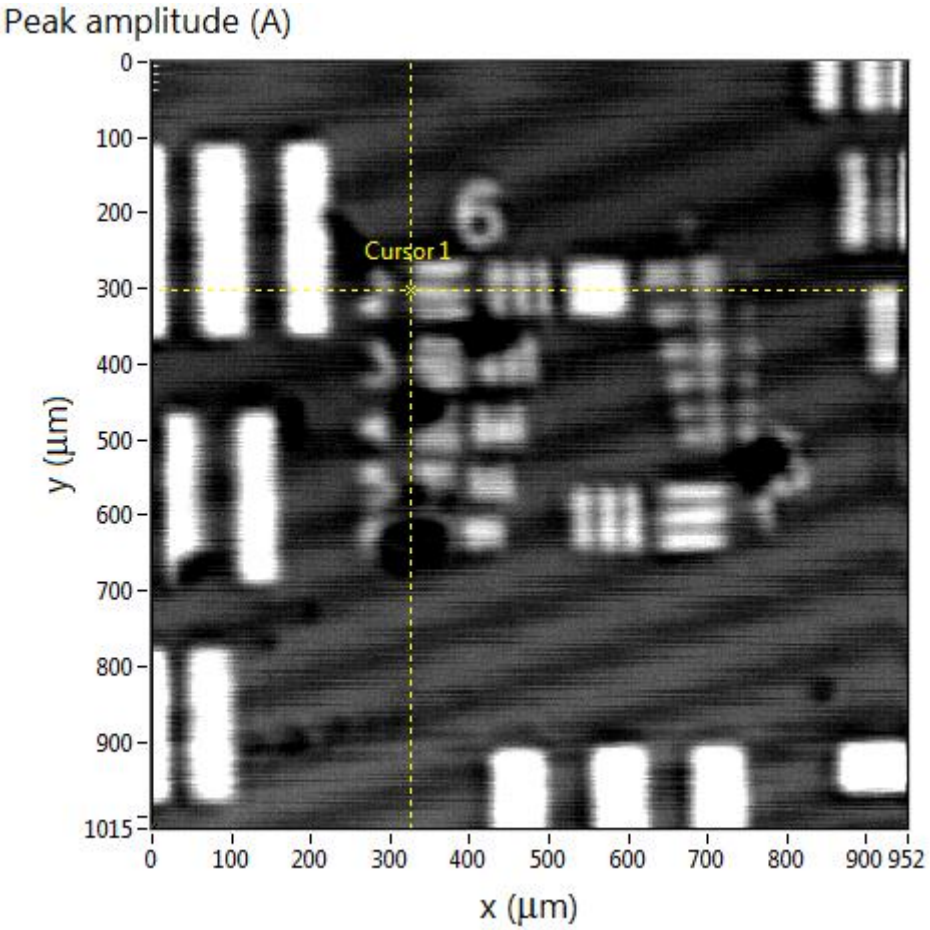

Figure 47: En-face image of the amplitude in channel A of a resolution test targe. The scanning field is reduced in order to measure the transverse resolution. The cursor marks the last group of stripes that can be resolved.

In order to investigate the impact of calculating the phase difference between the channels within the entire scanning field, the absolute phase values and the phase difference between the channels of the en-face scans are evaluated.

The absolute phase images (Fig. 48) show phase oscillations in A-scan direction that resemble the A-scan oscillations in the BM-scan image retrieved from the mirror (Fig. 44). Additionally, a strong phase shift along the orthogonal (vertical) direction can be observed.

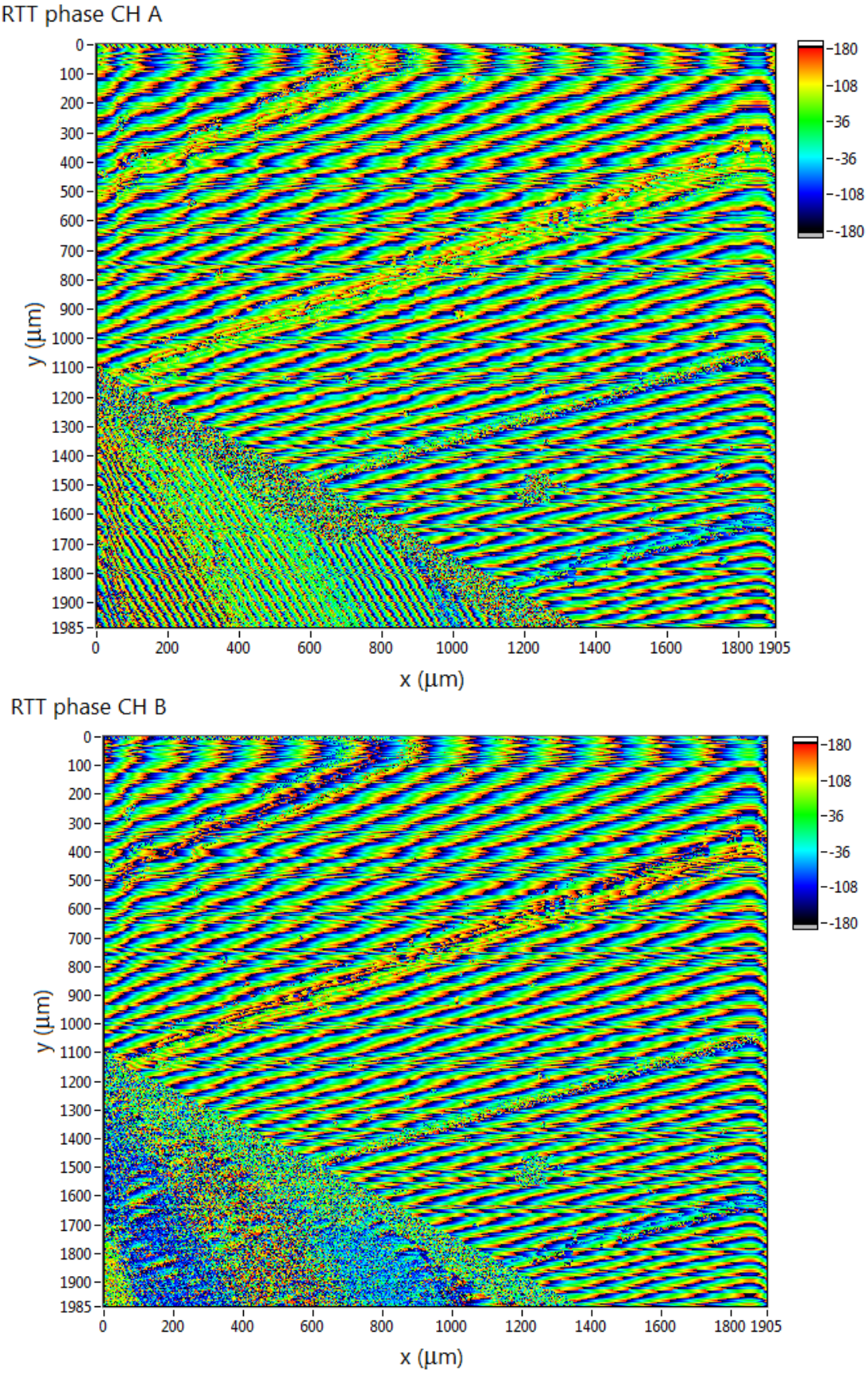

Figure 48: Absolute phase values measured at the top surface of the RTT in both channels. Strong phase changes associated with the orientation of the RTT in respect to the imaging beam dominate the image that impede direct detection of the structure of the RTT. Color scale: Absolute phase values in degrees.

The absolute phase can in principle be corrected for these phase shifts in post-processing (as outlined in e.g. [14]). However, problems arise at locations of low signal intensity (cf. bottom left corner in Fig. 48).

Before subtracting the absolute phases, an algorithm is applied on the absolute phases to ensure that Pi-jumps in the absolute phases do not evoke errors in the subsequent phase difference calculation.

Calculating the phase difference between the channels eliminates phase fluctuations. Fig. 49 shows the corresponding phase difference image and resolves the structures of the RTT with the transverse resolution of channel A.

A slight drift of the differential phase in vertical direction (B-scan direction) suggests that the beams are not perfectly co-linear and that one of the beams faces a pivot point misalignment resulting in a phase shift over the scanning field as simulated in chapter B2.2.3.

An angular displacement of the beams before the lens leads to a shift between the scanning fields after the lens. This shift is reflected in the phase difference image by asymmetric shadows that are cast by structures. The sharp beam (A) produces a sharp edge that is shifted to the left in comparison to the smooth edge produced by of the broad beam (B). In a perfectly aligned system, the shadows should be located symmetrically around the sharp structures.

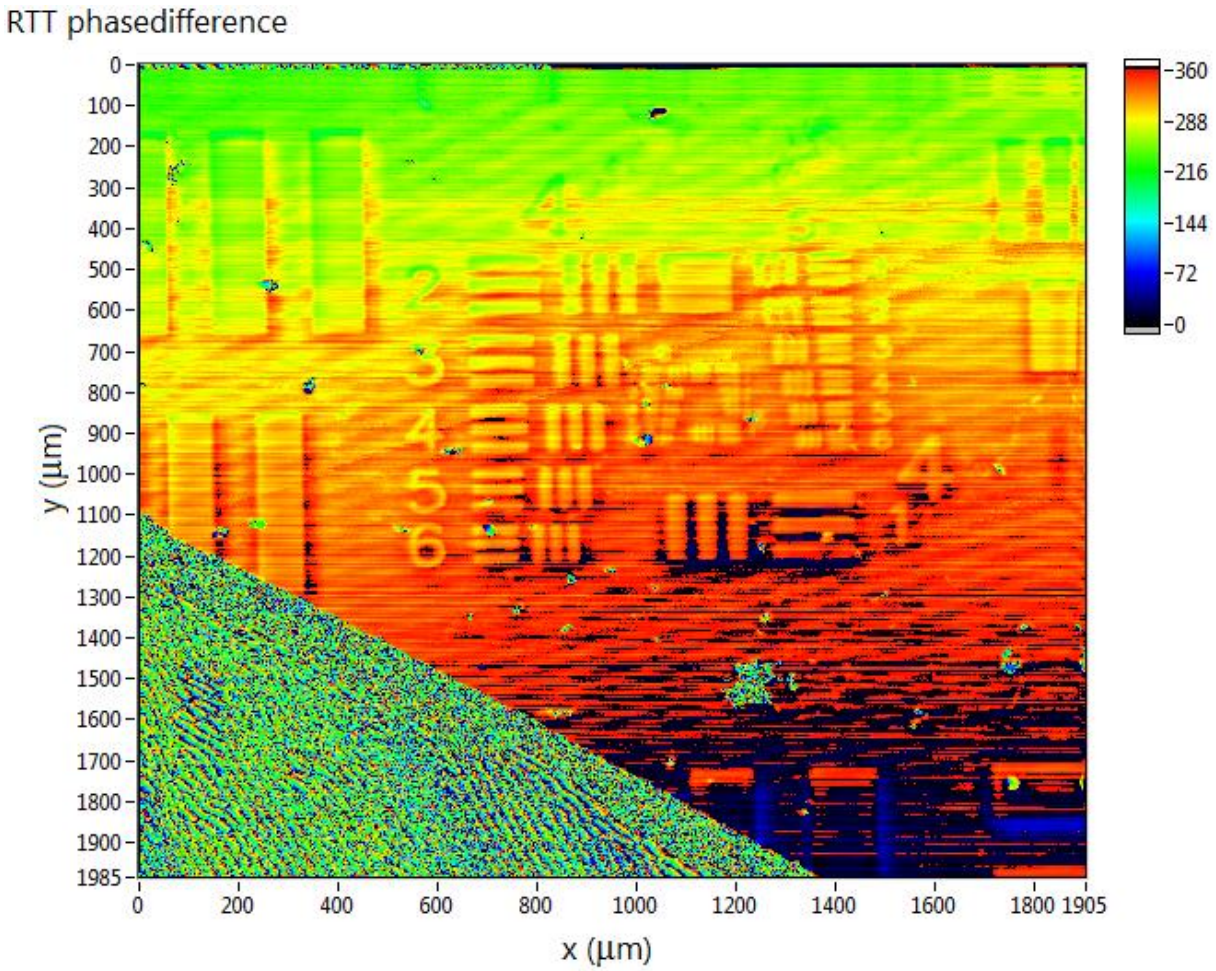

Figure 49: Phase difference image at the top surface of the RTT. Every line structure casts a shadow to the right and downwards. The transition of the shadow is smooth in comparison to the transition of the structure itself and can therefore be assigned to beam B, while the sharp edges of the structure are produced by beam A with sharper focus.

3) Quantitative phase measurements

For quantitative phase measurements three calibrated test samples of defined step sizes (50, 100, 200 nm) are measured.

3.1 BM-scans of the test samples

At first, BM-scans are taken at a position, where falling and rising edge of a predefined depth are included in the horizontal line scan.

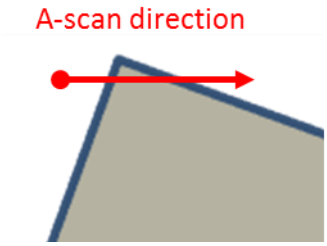

Figure 50: Illustration of the position of the BM-scan on the test sample

The edge appears steep in the imaging beam if the angle between edge and A-scan direction is rather perpendicular and flat if the angle is small as indicated for the first and second edge crossing of the beam in Fig. 50.

Additionally, imperfections of the sample and the already outlined beam displacements require a careful interpretation of the phase-difference images.

Fig. 51 shows the phase-difference image and quantitative evaluation of the sample with a 50nm step. A slight linear drift in the phase along x-direction indicates a pivot-point misalignment of at least one beam. The different phase changes associated with the beam transition over the two edges indicate different beam displacements at these locations. While the first edge (at x-position 800µm) can be used for evaluation of the local beam displacement, the second edge (at x-position 1650µm) cannot be used, as the expected upwards-downwards peak is not visible. Modulations in the phase along the x-direction and changes due to the edge on the phase-difference signal cannot be separated.

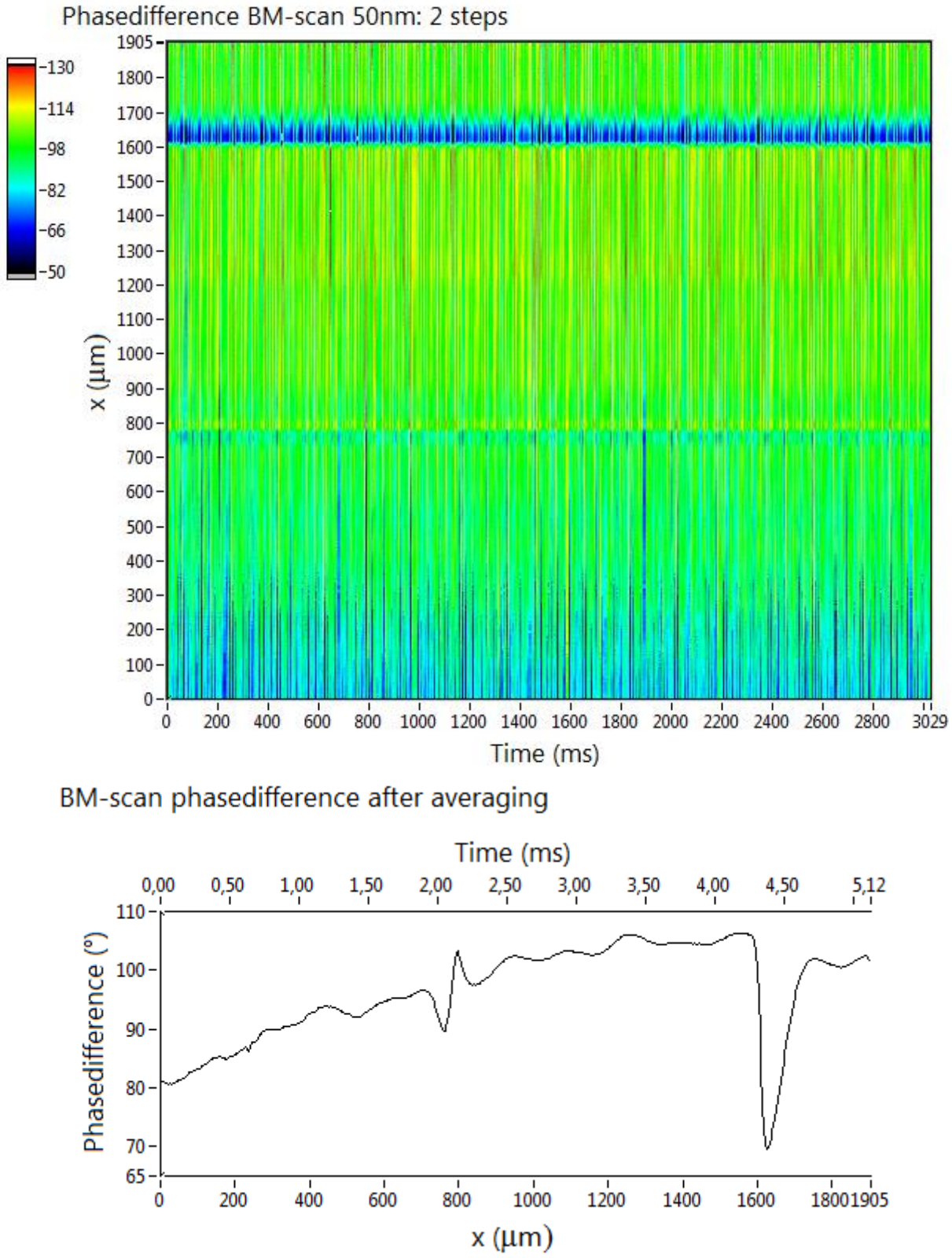

Figure 51: BM-scan of the test sample with a 50nm step. Above: Phase-difference image, bottom: Phase-difference along the x-direction after averaging over all B-scans displayed above. The two edges are located at x-position 800µm and 1650µm respectively. Color scale: Phase difference in degrees.

The angles of edge 1 and 2 with respect to the A-scan direction are retrieved from the en-face scan image (Fig. 55) and are measured to be 57° for edge 1 and 147° for edge 2, while 90°

indicates a perfectly orthogonal transition of the beam over the edge. The lateral phase shift along x-direction shows a pivot point problem that is reflected in the approximately linear increasing phase difference.

Different shapes of the phase difference signal at edges 1 and 2 can be observed that are due to the different angle between beam and edge and the displacement of the beams.

The expected change in the absolute phase values resulting from a step size of Δz is calculated by formula (11). The obtained theoretical value corresponding to a 50nm step and an imaging wavelength at 1045nm is 34.4° (half step size 17.2°).

Formula (18) is used for the simulation. The parameters a and b are calculated from the transversal resolutions as shown in formulae (15a) and (15b) denoting values of a=0.157µm^{-1} and b=0.044µm^{-1}. As a result of a non-orthogonal transition over the edge, the slopes are divided by a factor of $1 + \sin(\alpha)\tan(\alpha)$ (cf. chapter B2.3.2). In this case, α=33° and both slopes are divided by a factor of 1.35. The pivot point mismatch can be estimated with a linear approximation of the differential phase progression in Fig. 51, which results in a value of d = 0.015°/µm.

The parameters A (half step size) and c (lateral x-displacement between focal spots of the beams) are the unknown variables that are fitted with the model.

A value of A=14° for the half step size and a displacement of c = -2µm were obtained by the simulation.

The value of the half step size A lies below the theoretical value of 17.2°. The reason for that is the finite lateral extension of the edge, which results in a reduced FSR and thereby in a smaller amplitude of the phase difference peak (Chapter B2.3.1).

The peak in the phase difference signal introduced by edge 2 in Fig. 51 shows a completely different shape and an amplitude that roughly matches the absolute step size. This indicates that the two beams are laterally displaced such that one beam fully (with the entire beam diameter) traverses the edge (undergoes a phase change according to the step size) before the second beam reaches the edge. When the second beam traverses the edge, a similar phase change is introduced to this beam which results in the observed decrease of the phase difference signal (see also description in chapter B2.2.5).

Next, a sample with a 100nm step is examined. This sample shows higher jumps in the phase difference but the upwards-downwards peak which is required for the theoretical calculation outlined above cannot be observed. The small peak after the first valley is another structure (probably just a dust particle) and not related to the edge.

The expected absolute phase jump for the sample with a 100nm step is 68.8°.

Similar as for the sample with 50nm step size, different amplitudes in the phase difference image of the two edges can be observed. These are a result of different lateral displacements between the beams when scanning over the edges. Specifically, the lateral displacement of the two beams in direction orthogonal to the scanning axis greatly influences the corresponding phase measurements. Thereby, the delay between the transitions of the center of each beam over the edge plays a major role. Small delays (as in the case of almost perpendicular transition of the beams over the edge) results in a phase difference signal that shows first a slow decrease that is followed by a steep increase and again followed by a slow decrease until the original phase difference signal is reached (cf. left part in Fig. 51). Larger displacements between the beams result in a disappearance of this typical signal and only a slow decrease of the phase difference can be observed that is the followed by a slow increase (cf. Fig. 52). Thereby, the amplitude of the signal (i.e. how strong the phase difference change is) depends on the step size as well as on the displacement between the center of the beams at the edge of the transition.

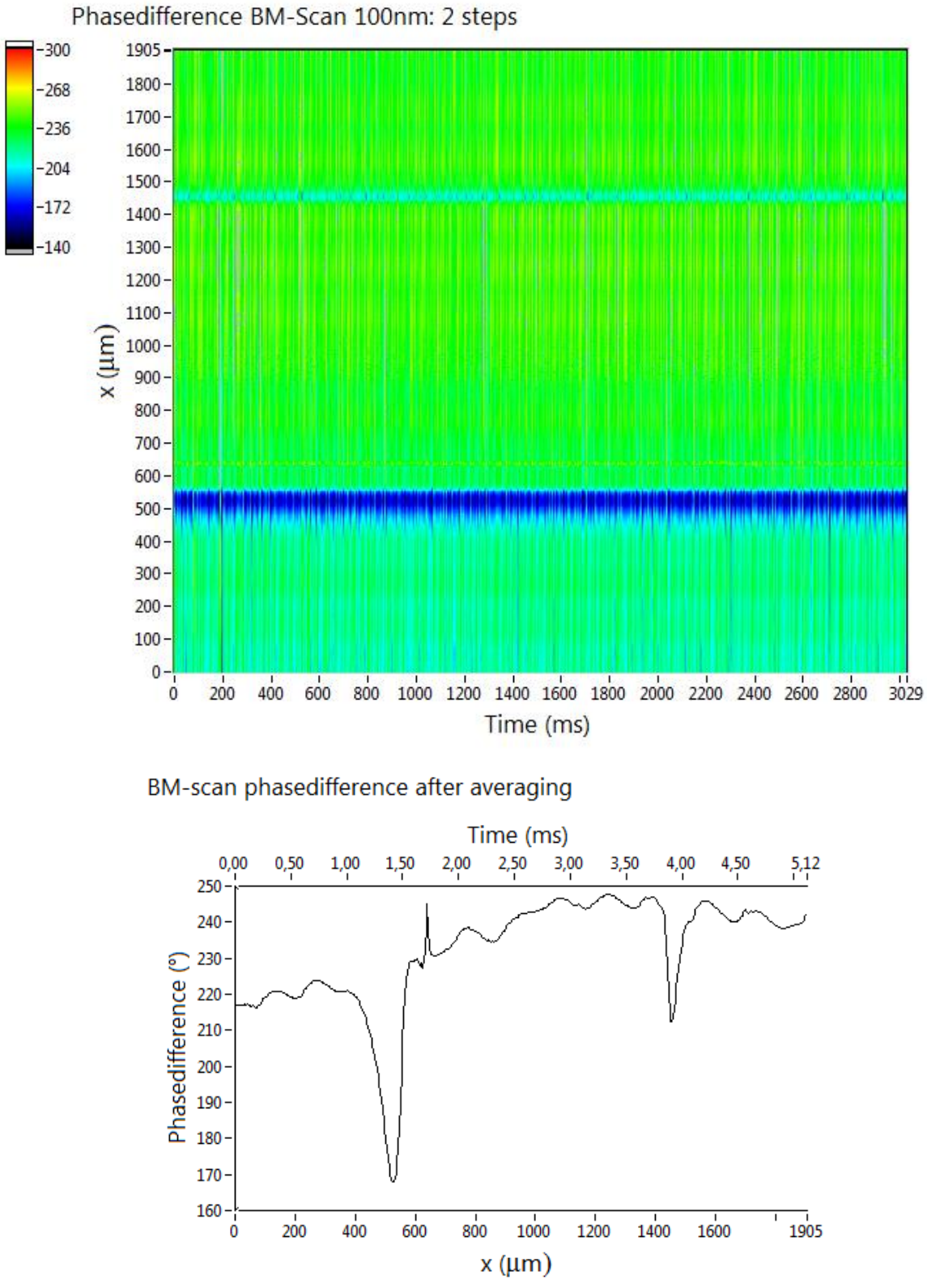

Figure 52: BM-scan of sample with 100nm step size. Above: Phase-difference image, bottom: Phase-difference after averaging over the B-scans

The expected absolute phase jump of a 200nm step is 137.6°.

The BM scan of a sample with 200nm step height (Fig. 53) shows higher jumps in the phase difference image than the 100nm sample. The dataset does not show the expected phase change (as the first peak in Fig.51).

In the sample with the 200nm step, the measured phase difference is not double the value of the phase difference measured at the sample with the 100nm step as it theoretically should. The reason for this is a possible flattening of this large step (which can be seen in the amplitude en-face images, cf. Fig.56).

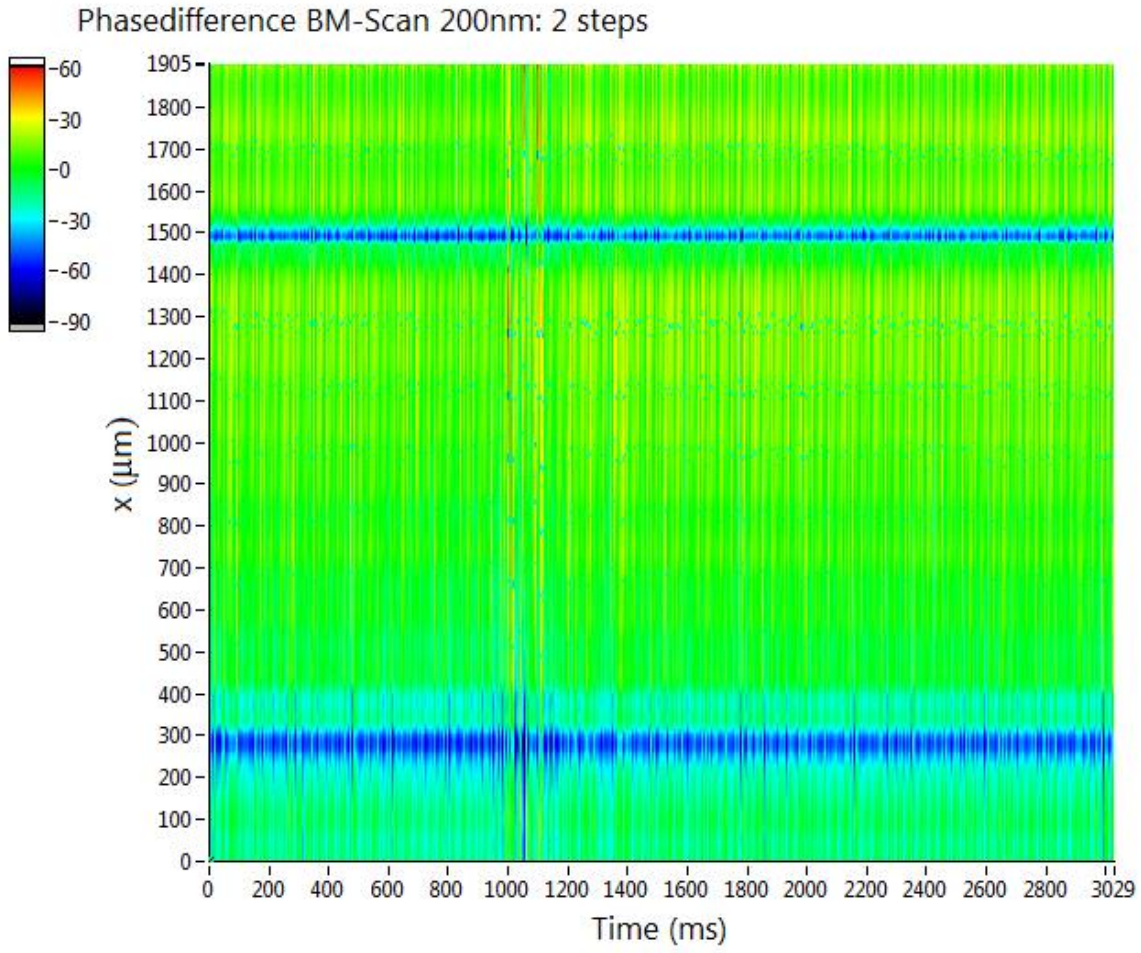

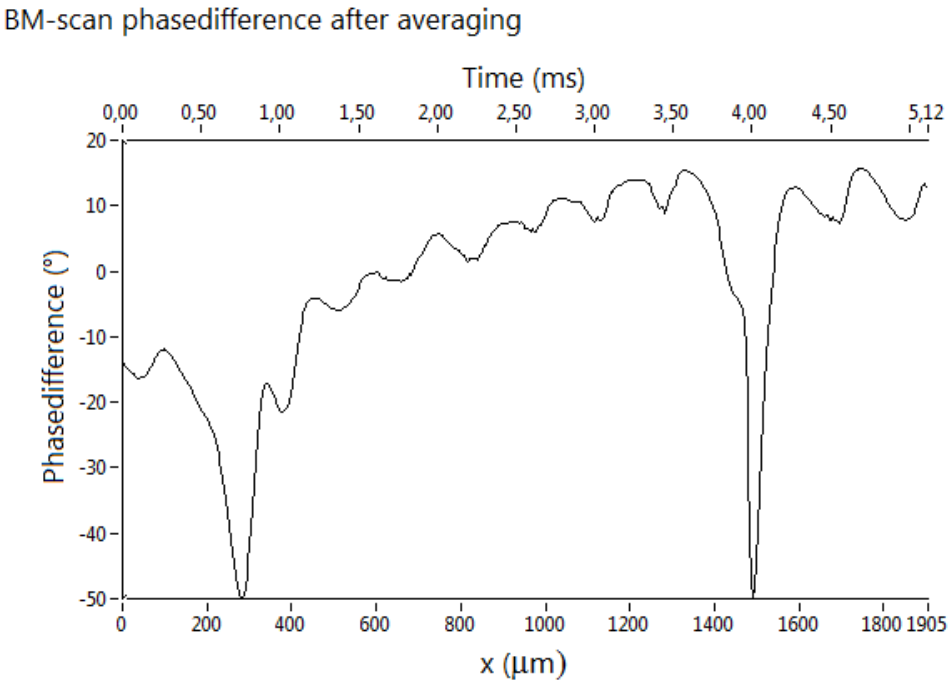

Figure 53: BM-scan of a sample with 200nm step size. Top: Phase-difference image. Bottom: Phase-difference after averaging over the B-scans

An investigation in terms of reproducibility of the measured phase difference values for the different step heights is summarized in Table 6.

Table 6: Reproducibility of the measured phase difference values within a BM scan. The mean reflects the average phase difference measured for each step and the standard deviation reflects the fluctuations between the recorded B-scans.

Step size	50nm		100nm		200nm	
	Edge 1	Edge 2	Edge 1	Edge 2	Edge 1	Edge 2
Mean	14.26°	38.15°	62.54	36.87°	34.04°	63.44°
Std.dev.	1.56°	1.66°	2.05°	1.63°	1.67°	2.22°

3.2 En-face scans

In the next step performed, entire volumes were recorded in order to generate en-face images of the sample. The measured en-face images of the different samples are shown in Fig. 54-56. All three images show a linear phase shift along the vertical (B-scan) axis and horizontal (A-scan) axis.

In a first step, the mean values of the jump in the phase difference images are calculated by averaging over 80 adjacent B-scans as summarized in Tab.7.

Table 7: Phase difference changes associated with the edges of the sample assessed by averaging over adjacent B-scans (n=80). The two columns represent the upper and lower edge of the samples.

Step size	50 nm		100 nm		200 nm	
	Upper edge	Lower edge	Upper edge	Lower edge	Upper edge	Lower edge
Mean value	11.9°	35.35°	20.5°	62°	62.75°	32.72°
Standard deviation	3.86°	2.89°	6.58°	6.96°	3.7°	2.47°

The edge of the 200nm sample is flatter than the edges of the other samples. Thus, the measured jump in the phase difference is not significantly larger, as a higher step would otherwise indicate.

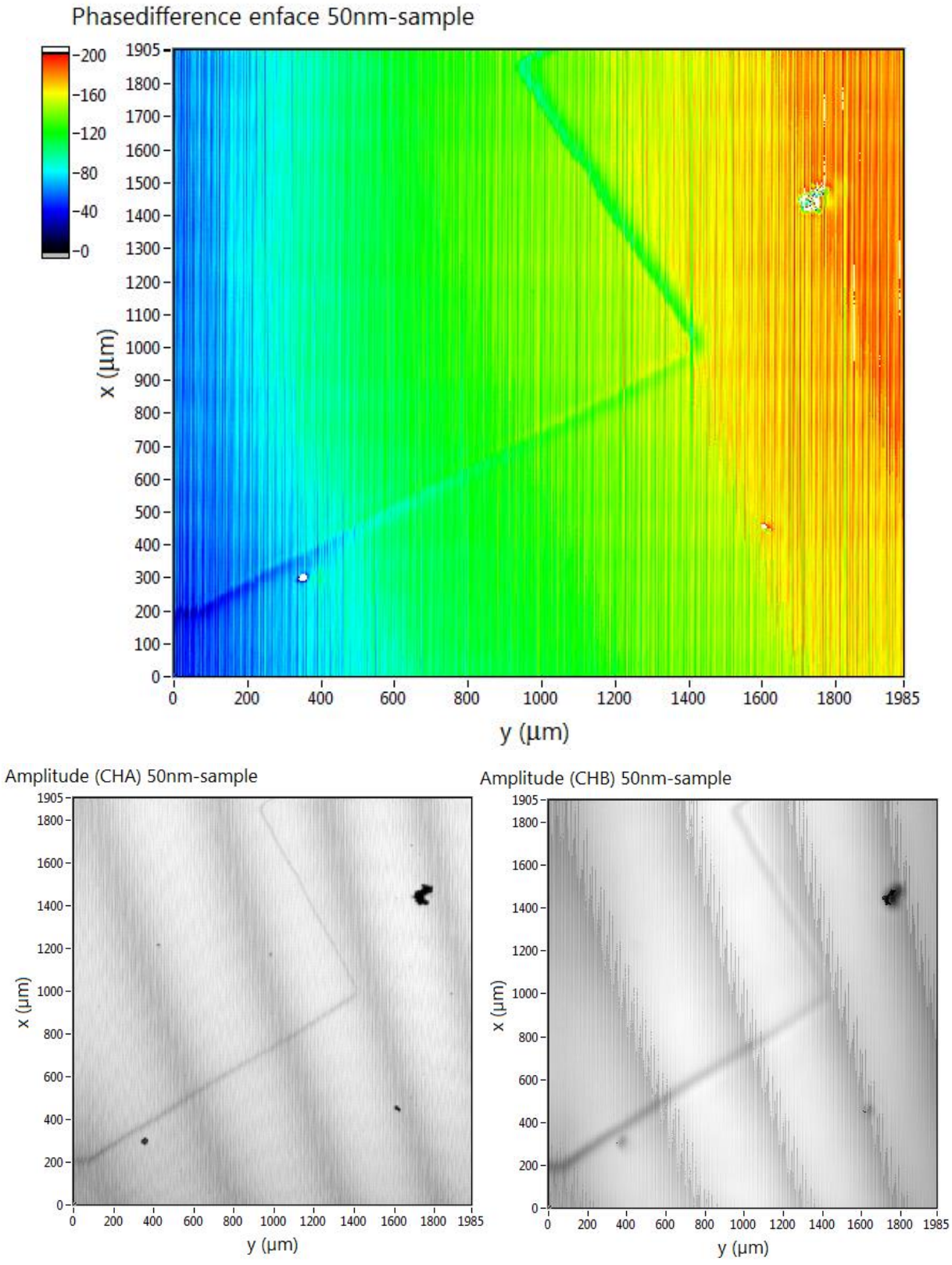

Figure 54: En-face Images of the sample with a 50nm step sizes. On top: the phase difference image with the color bar depicting the phase difference in degrees. Bottom: Amplitude images of the beam with narrow focal spot diameter to the left and the broader focal spot diameter to the right. The grey-values contain the amplitude of the back reflected light of the sample. The amplitude images are taken as a measure of the edge orientation, while the phase difference image allows a quantification of the edge. The first edge has a smaller extension in the phase difference image than the second edge, as the phase changes slower when the edge and (x-)scanning direction form a smaller angle.

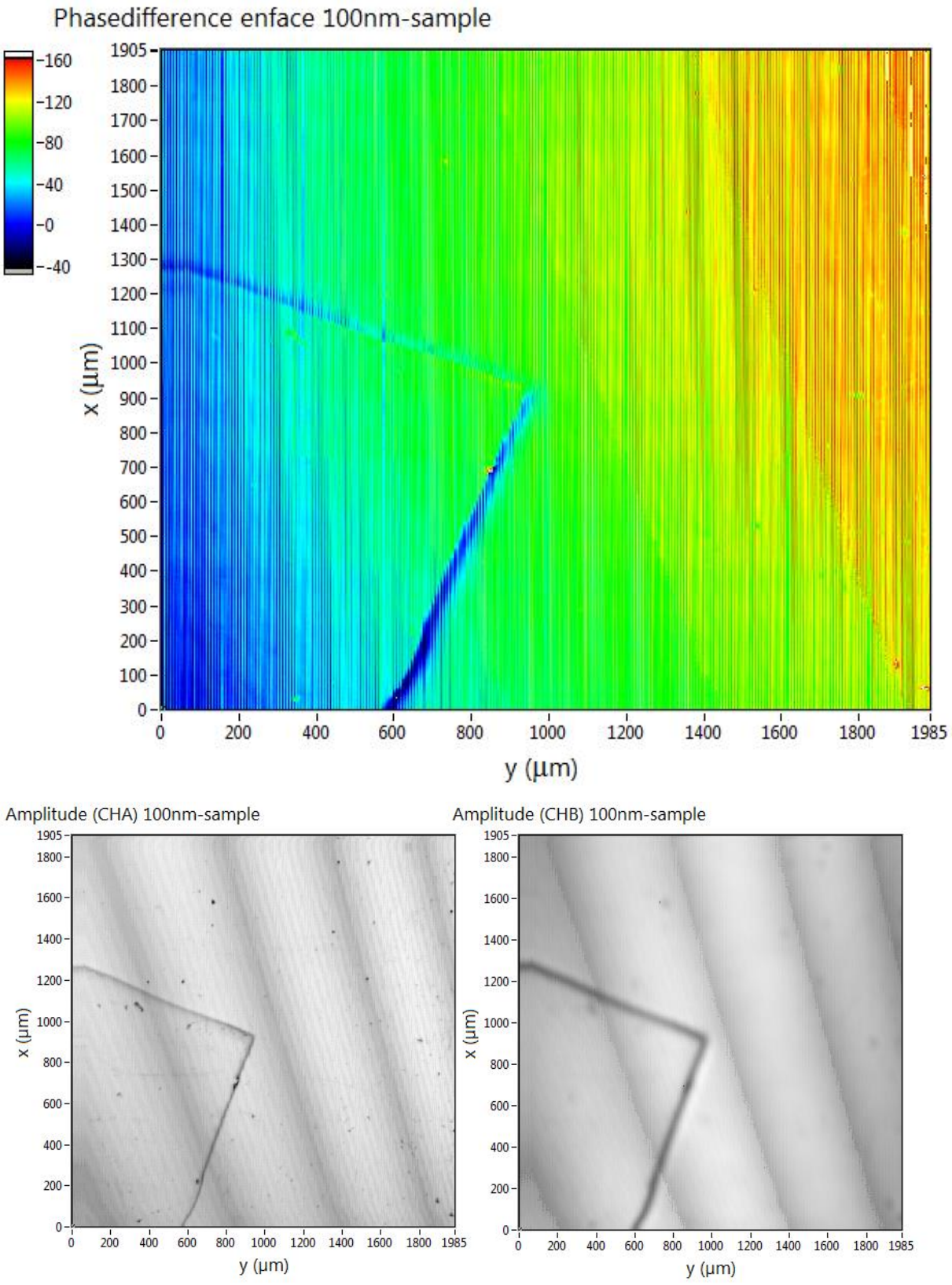

Figure 55: En-face images of the sample with 100nm step size. On top: The phase difference image with the color bar depicting the phase in degrees. Bottom: Amplitude images of the beam with narrow focal spot diameter to the left and the broader focal spot diameter to the right. The grey-values contain the amplitude of the back reflected light of the sample. The differential phase changes very slowly for the edge that forms a small angle with the scanning direction (which is starting at y=600µm). A higher contrast in the amplitude image can be observed in comparison to the sample with 50nm step size.

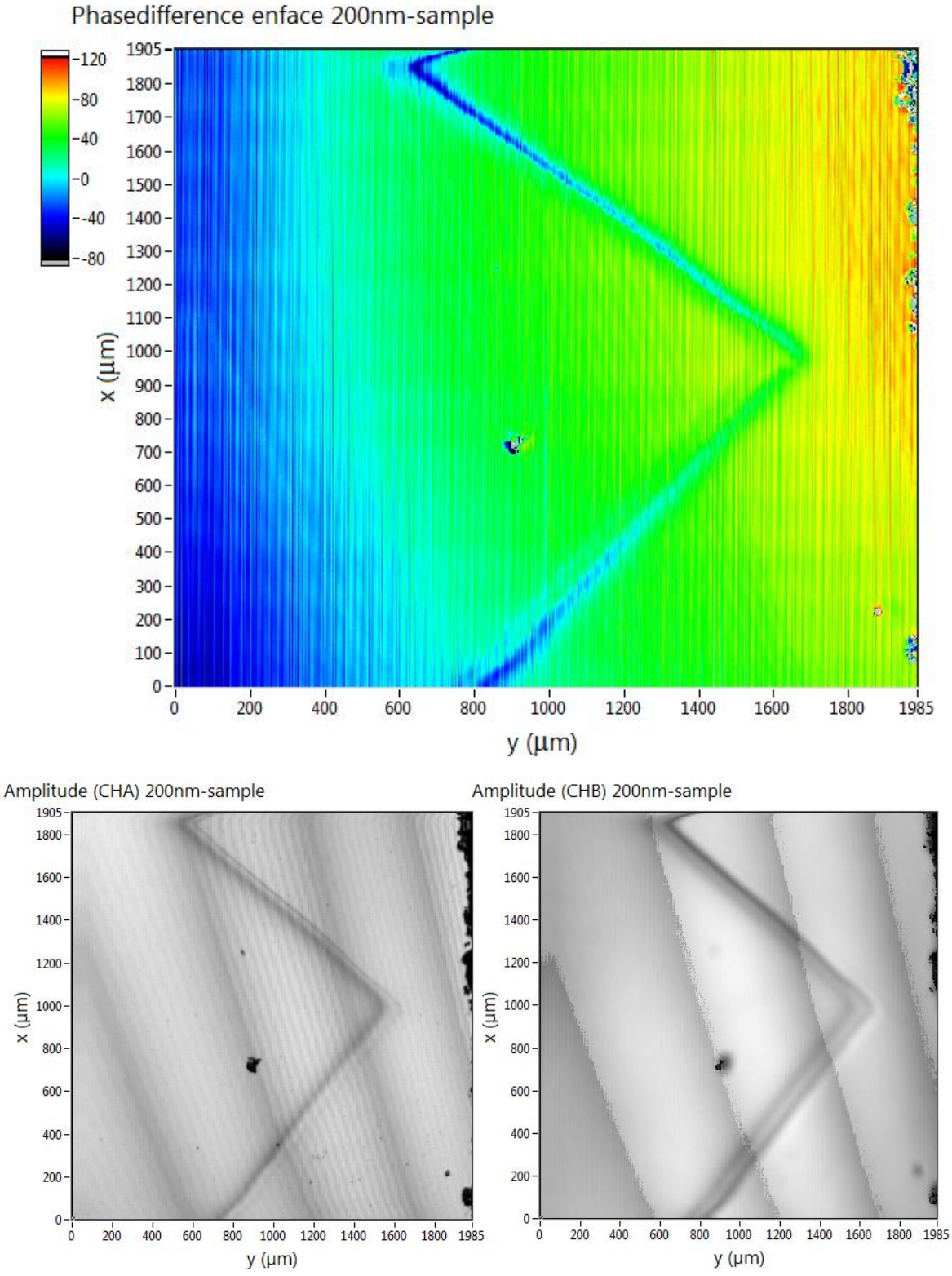

Figure 56: En-face Images of the sample with 200nm step size. On top: The phase difference image with the color bar depicting the phase in degrees. Bottom: Amplitude images of the beam with narrow focal spot diameter to the left and the broader focal spot diameter to the right. The grey-values contain the amplitude of the back reflected light of the sample. The 200nm sample shows a wide edge even in the amplitude image of the beam with high resolution. This depicts a flattening of the edge and explains the strong reduction of the peak in the phase difference images.

3.2.1 Long term stability

The long term reproducibility is examined by comparison of five consecutive measurements, taken within five minutes. The measured values are shown in Table 8.

Table 8: Repetitive measurements of both edges in the sample performed every 5 minutes. The left column represents the lower edge in the en-face image, the right column the upper edge. The difference between the columns of each sample comes from different scanning angles with respect to the edge.

Step size	50nm		100nm		200nm	
Time/ Min.	Upper edge	Bottom edge	Upper edge	Bottom edge	Upper edge	Bottom edge
0	14.57°	39.24°	18.3	58.59°	57.6°	30.2°
5	12.7°	41.24°	22.58	56.28°	61°	30.11°
10	15.32°	40.25°	19.63°	58.96°	64.92°	33.1°
15	15.93°	41.12°	22.77°	63.24°	62.87°	28.87°
20	12.71°	39.33°	19.69°	58.6°	60.14°	29.11°
Mean value	**14.26°**	**40.24°**	**20.6°**	**59.13°**	**61.3°**	**30.27°**
Std. dev.	**1.33°**	**0.85°**	**1.77°**	**2.26°**	**2.48°**	**1.5°**

The reproducibility measurements show that the phase subtraction method principally works. However, instabilities because of residual interferometric jitter and phase fluctuations due to scanner control in the sample arm are responsible for the small variations of the measured value.

As several dust particles on the surface of the sample with a 100nm step were observed, a second attempt was made to quantify the beam displacement over the scanning field by localizing the center of dust particles in both amplitude images (cf. Fig. 57). The x- and y-deviation of the positions in the image correspond to the beam displacements in x- and y-direction at the sample.

A parabolic fit reflected the beam displacement in y-direction as a function of the vertical coordinate y quite well. The displacement in x-direction as function of the horizontal coordinate x was distributed around a mean value of 6µm (cf. Fig. 58).

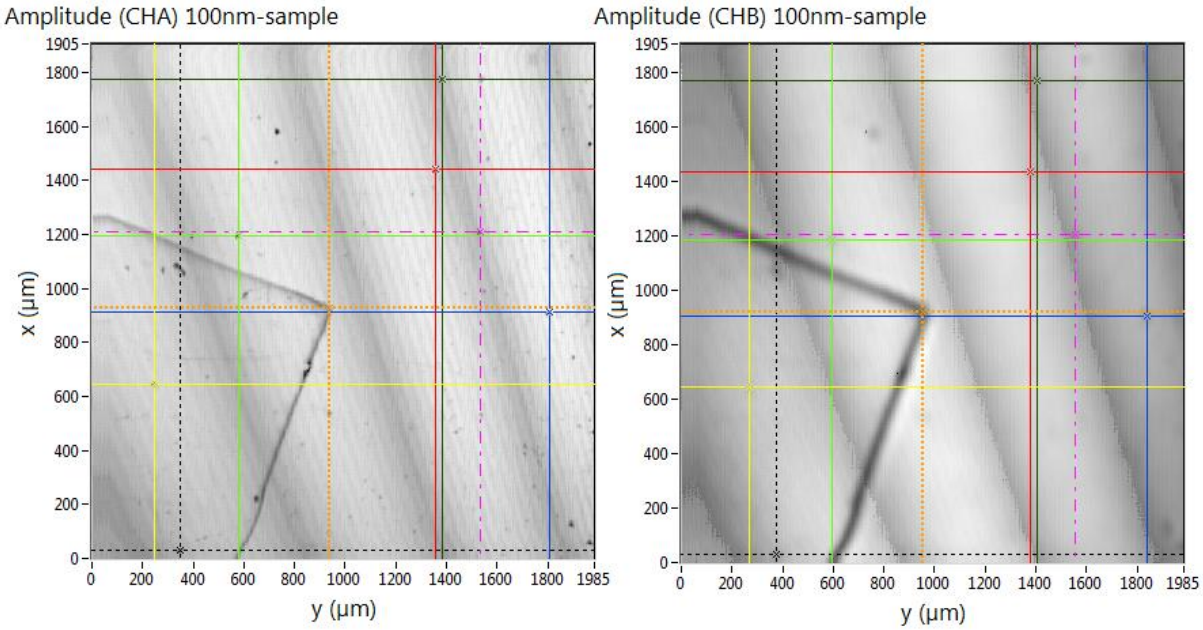

Figure 57: Amplitude images of a sample with a 100nm step size. Various dust particles can be identified in both images. The displacement of the locations of these particles in Channel A and Channel B is used to examine how the beam displacement changes over the scanning field. Some particles cannot be seen in the full field of view of Channel B, but can be identified by zooming into a region where the particle is assumed and increasing the contrast. The location of particles that are used to quantify the displacement between the beams are marked with cursors in different colors.

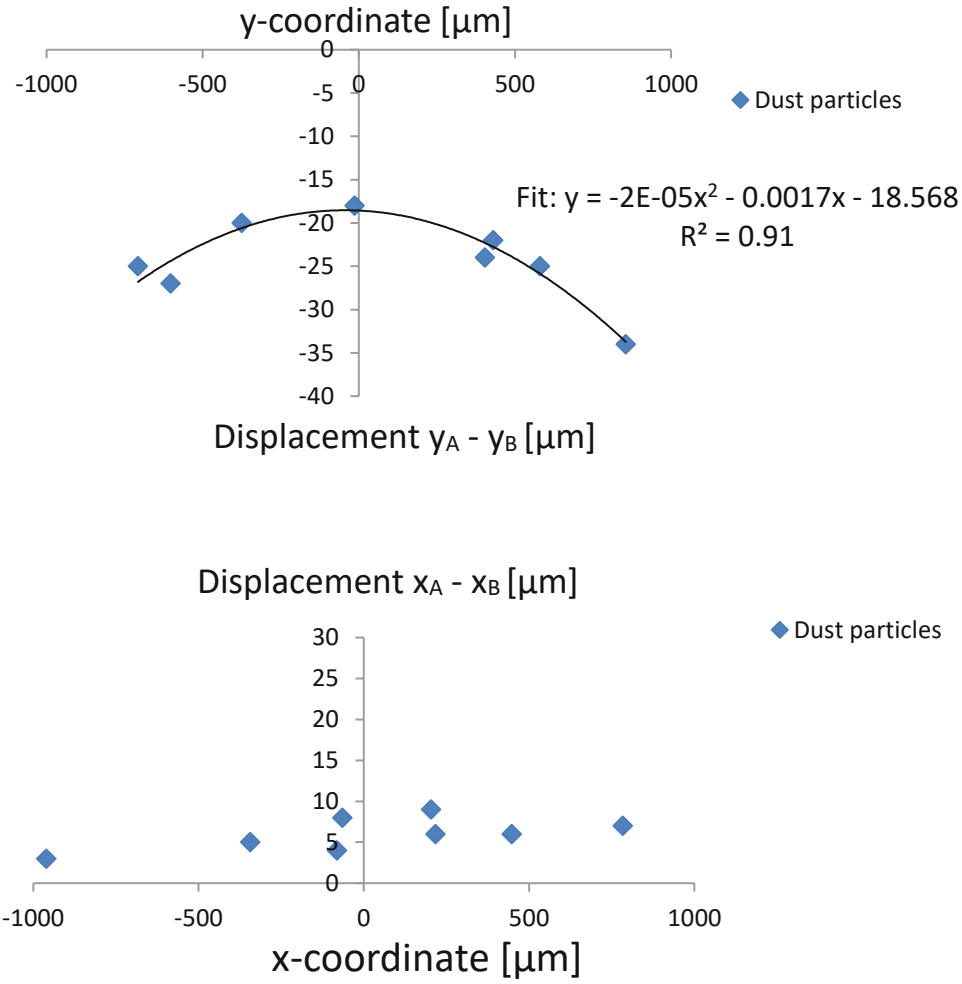

Figure 58: Evaluation of the beam displacement measured by localized dust particles. A parabolic fit described the beam displacement in y-direction of the scanning field quite well, while the beam displacement in x-direction was distributed around a mean value of 6µm. Note that the coordinate system does not represent the coordinate system of Fig. 58, but the point of origin (0,0) now represents the center of the amplitude image.

With the now determined displacement between beams A and B in x- and y-direction, the situations occurring at the transitions of edges of the three samples can be explained.

For the sample with a 100 nm step and the sample with a 200 nm step, the beams are displaced in a way that the edges are not traversed simultaneously by both beams.

For the sample with a 50nm step, the orientation of the edge and the beam displacement compensate for each other and a simultaneous transition (at different edge positions) is the case, which allows recalculation of the step size.

E. Discussion

In this work, a setup was developed that allows to assess the differential phase between two OCT beams of different focal spot diameter (chapter C1). Differential phase values were simulated in order to enable a better interpretation of the recorded signals (chapter B2.2).
Linked with the alignment procedures of the scanner pivot point, software has been developed to check if the beam is impinging on the rotation axis of the scanner (chapters C2, C3).
Furthermore, the required steps in post processing to obtain differential phase images have been explained (C2). The temporal stability of the differential phase values was investigated by using a mirror as sample. The axial and transverse resolution of the system was determined through measurements on a resolution test target. Finally, quantitative phase measurements have been performed on specifically manufactured test samples (chapter D).
Using dust particles on the surface of one test sample, a method for assessing the displacement of the two beams within the scanning field was found (chapter D3).

The measurements of the RTT as well as the mirror (chapters D1, D2) show that calculating the phase difference between the two OCT beams allows to minimize instabilities in the phase measurements introduced by the optical setup and to significantly reduce phase noise on the measurement. Furthermore, depth variations of technical samples can be measured by this technique, as edges introduce a deterministic phase difference signal, that can be used to estimate the height of the (known) original structure (chapter D3).

Even slight misalignments of the pivot point of the scanner in respect to the imaging beam evoke a strong impact of the servo control of the scanners on the absolute phase measurement. This is reflected in a modulation of the absolute phase measurement with a frequency of approximately 2 kHz (chapter D1, cf. Fig. 41).
With the two-beam setup, two perfectly aligned beams would allow to completely get rid of this influence, as the same fluctuations will be present for both beams. Any misalignment of the two beams will cause residual phase fluctuations as can be seen in Fig.44 (chapter D1).
Thus, a perfect alignment of the beams goes hand in hand with an efficient reduction of noise introduced for example by the galvanometer scanner.
It should be noted, that even when excluding influences of the optical setup a fluctuation of 300 Hz that is likely caused by electronic components was still observed on the measured differential phase signal (chapter D1, Fig. 40-43). This noise influences the overall precision

of the proposed method and should be eliminated if a higher precision is needed. However, for the measurements performed in this thesis this influence was negligible.

For the used field of view of 2x2 mm^2 the galvanometer scanner generates in principle a regular scanning field with approximately constant light intensity (cf. Fig.46, Figs. 54-56). For larger scanning fields, intensity losses in the periphery of the field of view are introduced in a reflecting sample because the back-reflected light is not back coupled into the fiber components. This is mainly caused by the combined x-y-scanner unit where both scanners are physically separated and the imaging lens can only be optimized for one scanner.

This problem can be overcome by a setup where a telescope is placed between the scanners so that the pivot point of one scanner is imaged onto the pivot point of the second scanner. Another possibility is the use of a microelectromechanical system (MEMS), where a single mirror can be tilted in x-and y-direction for the scanning procedure.

Another issue of the method is the residual misalignment between the beams over the scanning field. A quantification of that was achieved by analyzing dust particles on the surface of a sample (chapter D3). As the resolution of the beam with larger focal spot diameter is limited, edges of a sample or of structures of the RTT are not directly suited for examining the beam displacement, while small particles can be localized very well with the beams of low and high resolution by localizing the center of the particle in the amplitude images.

The analyzed beam displacements in y-direction can be approximated by a parabolic fit, while the displacements in x-direction did not follow a specific trend but stayed rather constant around a mean value (chapter D3).

The varying lateral displacement between the beams causes different behaviors of the measured phase signal depending on the location within the scanning field. This has to be considered and makes the current version of the system less applicable. For example, when imaging a simple technical test target as the edge with a specific step size, the orientation of the edge in respect to the scanning direction needs to be considered for a correct interpretation of the data. For more complex samples this would not be possible.

The phase difference technique provides images with an improved contrast of phase changing structures such as the edges shown above compared to images that are based on absolute phase measurements. However, the imperfect alignment of the current system makes a quantification of the corresponding signal difficult. As outlined above, the beams must be

perfectly co-linear to remove the strong dependency of the orientation of the measured structure (such as edges) with respect to the scanning direction of the imaging beam on the measured phase difference signal.

Another problem for quantification of these subtle height difference is residual interferometric jitter, resulting from relative motion of the components within the sample arms of the two beams. Although, special care was taken to minimize this jitter, the current realization could not completely eliminate it.

A potential solution would be a setup where the beam separation (into large and small diameter imaging beam) is introduced before the main interferometer. This has the advantage that movements and other influences in the sample arm are then identical for both sample arms and can thus be eliminated by the phase difference calculation. Additionally, the back reflected light would not have to pass the beam separation unit again after being backscattered at the sample, which potentially reduces back coupling losses.

A disadvantage of such a setup is the usage of a large portion of bulk optics and a more sophisticated way to build the reference arm to minimize intensity losses there.

The co-linear alignment of the sample beams requires fine adjustment possibilities, as it has a huge influence on the phase differential measurement. Especially sample mirror SM2 and polarizing beam splitter PBS2 require adjustment possibilities with micrometer or even sub-micrometer precision.

For further noise reduction, a setup up needs to be built, where the beam separation takes place before the entrance of the main interferometer.

Furthermore, the focal condition has to be realized for both scanners, which requires either a physical separation of the scanners and introduction of a telescope between the scanners or the use of a MEMS-scanner.

Finally, a higher sensitivity of the system is necessary, in order to apply the phase differential method on scattering objects. This can be achieved by minimizing the losses at the individual components that leads to an increasing light intensity in the sample arm and higher power returning from the sample.

All these improvements can in principle be implemented and should allow to reach the final goal of the proposed method i.e. to detect phase changes in tissue with nanometer precision.

F. Conclusion

A dual beam setup for differential phase contrast OCT imaging was introduced. The system was used to image simple test targets and height differences on the surface in the nanometer range could be measured. A modelling function for the recalculation of the height difference from the phase difference function was presented.

In order to apply this technique in scattering samples, several improvements have to be implemented. Phase contrast OCT has great potential for visualizing subtle length changes well below the resolution limit of standard OCT.

G. References

1) J. F. de Boer, R. Leitgeb, and M. Wojtkowski", Twenty-five years of optical coherence tomography: the paradigm shift in sensitivity and speed provided by Fourier domain OCT [Invited]", Biomedical Optics Express 8, 3248-3280 (2017). DOI: 10.1364/BOE.8.003248
2) A. F. Fercher, "Optical Coherence Tomography", Journal of Biomedical Optics 1(2), 157-173 (1996). DOI: 10.1117/12.231361
3) K. Koyama, A. Iwasaki, M. Tanimoto, and I. Kudo, "Simple interferometric microscopy for in situ real-time two-dimensional observation of crystal growth", Review of Scientific Instruments 67, 2584-2587 (1996), DOI: 10.1063/1.1147190
4) A. Barty, K. A. Nugent, D. Paganin, and A. Roberts, "Quantitative optical phase microscopy", Optics Letters 23(11), 817-819 (1998). DOI: 10.1364/ol.23.000817
5) C. Yang, A. Wax, I. Georgakoudi, E. B. Hanlon, K. Badizadegan, R. R. Dasari, and M. S. Feld, "Interferometric phase-dispersion microscopy", Optics Letters 25(20), 1526-1528 (2000). DOI: 10.1364/ol.25.001526
6) A. Fercher, "Optical coherence tomography – developments, principles, applications", Zeitschrift Medizinische Physik 20(4), 251-76 (2010). DOI: 10.1016/j.zemedi.2009.11.002
7) F. Lexer, C. K. Hitzenberger, A. F. Fercher, and M. Kulhavy, "Wavelength-tuning interferometry of intraocular distances", Applied Optics 36 (25), 6548-6553 (1997). DOI: 10.1364/AO.36.006548
8) A. F. Fercher, C. K. Hitzenberger, G. Kamp, and S. Y. Elzaiat, "Measurement of Intraocular Distances by Backscattering Spectral Interferometry", Optics Communications 117(1-2), 43-48 (1995). DOI: 10.1016/0030-4018(95)00119-S
9) Z. Yaqoob, J. Wu, C. Yang, "Spectral domain optical coherence tomography: a better OCT imaging strategy", Biotechniques 39 (6), 6-13 (2005). DOI: 10.2144/000112090
10) F. Beer, R. P. Patil, A. Sinha-Roy, B. Baumann, M. Pircher, C. K. Hitzenberger, "Ultrahigh Resolution Polarization Sensitive Optical Coherence Tomography of the Human Cornea with Conical Scanning Pattern and Variable Dispersion Compensation", Applied Sciences 9, 4245, 1-12 (2019). DOI: 10.3390/app9204245
11) M. Sticker, M. Pircher, E. Götzinger, H. Sattmann, A.F. Fercher, C. K. Hitzenberger, "En face imaging of single cell layers by differential phase-contrast optical coherence microscopy", Optics Letters 27 (13), 1126-1128 (2002). DOI: 10.1364/OL.27.001126
12) C. K. Hitzenberger, A.F. Fercher, "Differential phase contrast in optical coherence tomography", Optics Letters 24 (9), 622-624 (1999). DOI: 10.1364/OL.24.000622
13) H. J. Huang, T. Y. Hsieh, L. D. Chou, W. C. Kuo, C. Chou, "Analog differential-phase detection in optical coherence reflectometer", Optics Express 16 (17), 12847-12858 (2008). DOI: 10.1364/OE.16.012847

14) M.Pircher, B.Baumann, E. Götzinger, H. Sattmann, C. K. Hitzenberger, "Phase contrast coherence microscopy based on transverse scanning", Optics Letters 34 (12), 1750-1753 (2009). DOI: 10.1364/OL.34.001750

15) B. Heisse, D. Stifter, "Quantitative phase reconstruction for orthogonal-scanning differential phase-contrast optical coherence tomography", Optics Letters 34 (9), 1306-1308 (2009). DOI: 10.1364/OL.34.001306

16) O. Vogel, A. Bruhn, J. Weickert, and S. Didas, "Direct Shape-from-Shading with Adaptive Higher Order Regularisation", In: Sgallari F., Murli A., Paragios N. (eds) "Scale Space and Variational Methods in Computer Vision. SSVM 2007", Springer, Lecture Notes in Computer Science 4485, 871-882 (2007). DOI: 10.1007/978-3-540-72823-8_75

17) F. Helderman, B. Haslam, J. F. de Boer, M. de Groot, "Three-dimensional intracellular optical coherence phase imaging", Optics Letters 38 (4), 431-433 (2013). DOI:10.1364/OL.38.000431

18) F. Beer, A. Wartak, R. Haindl, M. Gröschl, B. Baumann, M. Pircher, C. K. Hitzenberger, "Conical scan pattern for enhanced visualization of the human cornea using polarization sensitive OCT", Biomedical Optics Express 8 (6), 2906-2923 (2017). DOI: 10.1364/BOE.8.002906

19) S. Aumann, S. Donner, J. Fischer, F. Müller: "Optical Coherence Tomography (OCT): Principle and Technical Realization", In: "Bille J. (eds) High Resolution Imaging in Microscopy and Ophthalmology: New Frontiers in Biomedical Optics", Springer, 59-85 (2019). DOI: 10.1007/978-3-030-16638-0_3

20) M. A. Choma, A. K. Ellerbee, C. H. Yang, T. L. Creazzo, and J. A. Izatt, "Spectral-domain phase microscopy", Optics Letters 30 (10), 1162-1164 (2005). DOI: 10.1364/OL.30.001162

21) M. Sticker, C. K. Hitzenberger, R. Leitgeb, A. F. Fercher, "Quantitative differential phase measurement and imaging in transparent and turbid media by optical coherence tomography", Optics Letters 26 (8), 518-520 (2001). DOI: 10.1364/OL.26.000518

22) Axsun Technologies, Inc. "Axsun OCT source manual Rev 14", 2014

23) S. H. Yun, G. J. Tearney, J. F. de Boer, N. Iftimia, and B. E. Bouma, "High-speed optical frequency-domain imaging", Optics Express 11 (22), 2953-2963 (2003). DOI: 10.1364/OE.11.002953

24) M. A. Choma, M. V. Sarunic, C. Yang, J. A. Izatt, "Sensitivity advantage of swept source and Fourier domain optical coherence tomography", Optics Express 11 (18), 2183-2189 (2003). DOI: 10.1364/OE.11.002183

25) M. Wojtkowski, V. J. Srinivasan, T. H. Ko, J. G. Fujimoto, A. Kowalczyk, J. S. Duker, "Ultrahigh-resolution, high-speed Fourier domain optical coherence tomography and methods for dispersion compensation", Optics Express 12 (11), 2404-2422 (2004). DOI: 10.1364/OPEX.12.002404

H. List of abbreviations

AC	alternating current
AD converter	analogue digital converter
A-scan	axial scan
BD	balanced detector
BM-scan	repeated B-scan at the same vertical position in the scanning field
BS	beam splitter
B-scan	cross sectional image of a plane in direction of the imaging beam
CHA/CHB	polarization channel A/B
DAQ	data acquisition card
DC	direct current (=steady component)
DOF	depth of focus
DPC	differential phase contrast
DPOCR	differential phase optical coherence reflectometry
en-face scan	cross sectional image of a plane orthogonal to the imaging beam
FB	fiber based
FBG	fiber Bragg grating
FDOCT	Fourier domain OCT
FSR	focal spot ratio
FWHM	full width half maximum
GS	galvanometer scanner
K	conversion factor
L	lens
LCI	low coherence interferometry
LP	linear polarizer
M-scan	repeated A-scan at the same position in the scanning field
OCPM	optical coherence phase microscopy
OCT	optical coherence tomography
PBS	polarizing beam splitter
PC	polarization control paddles
PSOCT	polarization sensitive OCT
RM	reference mirror
RTT	resolution test target
SDOCT	spectral domain OCT
SfS	shape from shading
SL	sample lens
SLS	swept laser source
SM	sample mirror
SNR	signal to noise ratio
SSOCT	swept source OCT
Std. dev.	standard deviation
TDOCT	time domain OCT
TTL	transistor-transistor logic
ZOI	zone of interaction